KfK 3174
Juni 1981

Neutrino Physics at the Spallation Neutron Source

II Neutrino Fluxes, Shielding Considerations and Detector Analysis

T. A. Gabriel, R. A. Lillie, B. L. Bishop
J. Wilczynski, B. Zeitnitz
Institut für Kern- und Teilchenphysik

Kernforschungszentrum Karlsruhe

KERNFORSCHUNGSZENTRUM KARLSRUHE

Institut für Kern- und Teilchenphysik

KfK 3174

NEUTRINO PHYSICS AT THE SPALLATION NEUTRON SOURCE

II NEUTRINO FLUXES, SHIELDING CONSIDERATIONS AND DETECTOR ANALYSIS

T.A.Gabriel, R.A.Lillie and B.L.Bishop
Oak Ridge National Laboratory

J.Wilczynski and B.Zeitnitz
Kernforschungszentrum Karlsruhe

Kernforschungszentrum Karlsruhe GmbH, Karlsruhe

Kernforschungszentrum Karlsruhe GmbH
ISSN 0303-4003

NEUTRINO PHYSICS AT AN INTENSE SPALLATION NEUTRON SOURCE

II NEUTRINO FLUXES, SHIELDING CONSIDERATIONS AND DETECTOR ANALYSIS

Abstract

The shielding and detector analysis associated with a contemplated low energy ($\sim$ 10 to 50 MeV) neutrino experiment at a spallation neutron source are presented and discussed. This analysis includes neutrino production and interaction rates, time dependence of the neutrino pulse, shielding considerations for neutrons coming directly from the spallation source and those which are scattered from other experimental areas, shielding considerations for galactic sources especially muons and finally detector responses to neutrino and background radiations. In general for a 1 mA (200 ns/pulse, 100 Hz), 1.1 GeV proton beam incident on a lead target surrounded by a moderator system, approximately 8 m of iron are required to reduce the background so that the event rate in the detector systems is $\lesssim$ 1 event/day. If the detector system is not shadowed by the primary shield, then $\sim$3 m of iron above the detector are required to reduce the background from scattered neutrons from experimental areas and galactic muons to an acceptable level of $\lesssim$ 1 event/day. For a 50 ton mineral oil segmented detector system and a volume distributed source, resolutions of approximately 10% (FWHM) can be obtained for gamma rays and electrons in the 10 to 20 MeV range.

NEUTRINOPHYSIK AN EINER INTENSIVEN SPALLATIONS-NEUTRONEN-QUELLE

II NEUTRINOFLÜSSE, ABSCHIRMRECHNUNGEN UND DETEKTORENTWURF

Zusammenfassung

Für ein Neutrinoexperiment bei niedrigen Energien (~10 bis 50 MeV) an einer Spallations-Neutronen-Quelle wurden die Abschirmung und die Auslegung eines Detektors berechnet. Der erste Teil dieser Rechnungen gibt Aufschluß über die Erzeugungsrate der Neutrinos, die Wechselwirkungsrate der Neutrinos im Detektor und die Zeitabhängigkeit der Neutrinoflüsse. Im zweiten Teil wurde die Dicke der Abschirmung bestimmt, die notwendig ist, um den Detektor gegen Neutronen, die direkt von der Spallationsquelle und mehrfach gestreut von anderen Experimentierbereichen kommen, und gegen galaktische Strahlung, insbesondere Müonen, abzuschirmen. Im dritten Teil wurde das Ansprechvermögen des Detektors für Neutrinos und für Untergrundstrahlung bestimmt.

Es ist eine Eisenabschirmung mit einer Dicke von ca. 8m erforderlich, um den Strahlungsuntergrund, der von einem 1 mA (200 ns/Puls, 100 Hz), 1.1 GeV Protonenstrahl erzeugt wird, der auf ein von einem Moderator umgebenes Bleitarget trifft, so zu reduzieren, daß die Zählrate in den Detektorsystemen kleiner als 1 Ereignis/Tag ist. Falls sich das Detektorsystem nicht unterhalb dieser primären Abschirmung befindet, ist oberhalb des Detektorsystems eine zusätzliche Eisenabschirmung mit einer Dicke von ca. 3m erforderlich, um die Zählrate, die durch den Strahlungsuntergrund gestreuter Neutronen und galaktischer Müonen hervorgerufen wird, auf 1 Ereignis/Tag zu reduzieren.

Für ein segmentiertes Detektorsystem, das 50 Tonnen Mineralöl enthält, und für eine räumlich ausgedehnte Quelle wurde für Gammastrahlung und Elektronen im Energiebereich von 10 bis 20 MeV eine Energieauflösung von ca. 10% (FWHM) berechnet.

CONTENTS Page

I. INTRODUCTION

During the past several years interest has grown substantially in neutrino research[1-8]. The successful introduction and application of gauge theories and quark models has led to new and somewhat surprising new questions concerning the elementary properties of the neutrinos and yet other undetected massive exchange particles. If the neutrinos (ν_e, ν_μ, ν_τ) have mass, then the possibility that neutrinos transform into each other becomes a distinct possibility. This transformation has been put forth as a credible answer to the discrepancy existing between the measured and calculated number of neutrinos from the sun. In addition, if muon number conservation can be violated in the oscillation and the neutrinos of the electron and muon have different masses, this leads to the decay $\nu_\mu \rightarrow \nu_e + \gamma$ (if $m_{\nu_\mu} > m_{\nu_e}$). But, the lifetime estimate of this process ($\tau_{1/2} > 5 \times 10^{11}$ yrs) will not be measurable in the laboratory.

As a result of the gauge theories, interactions between particles can occur by exchange of the socalled $W^\pm$ boson and the electrically neutral particle Z^o. However, because of their great masses direct detection of these particles could not as yet take place in direct experiments. Still, their existence can be inferred and many fundamental questions answered by studing low energy neutrino interactions. A more detailed discussion of the physics motivation for low energy neutrino experiments at intense accelerators is presentend in part I of this paper[19].

The spallation neutron source (SNQ) currently being contemplated for the Federal Republic of Germany and the SNS being constructed at Rutherford Laboratory in England will have the necessary beam currents and time structure for detailed neutrino research and presents the possibility of improving the upper limit on the mass of the neutrino by at least an order of magnitude. In addition to investigating previously considered neutrino interactions: for example, $\nu_\mu + e^- \rightarrow \nu_\mu + e^-$ and $\nu_e + d \rightarrow p + p + e^-$ additional nuclear transition interactions can be considered: for example,

$$\nu_\mu + {}^{12}C \rightarrow \nu_\mu' + {}^{12}C^* \\ \hookrightarrow {}^{12}C + \gamma \ (15.1\ \mathrm{MeV}).$$

Since neutrino reactions at spallation type sources will deal with the detection of low energy particles (~ 10 to 50 MeV), this paper specifically addresses the response of various detector systems to gamma rays and electrons in this energy range and the shielding necessary to reduce machine and background radiation to an acceptable level. Neutrino interaction rates ($\sigma \lesssim 10^{-40}$ cm^2) are notoriously low, even for high beam current (~1 mA) machines. If detailed neutrino research is to be accomplished, the background rate from all sources must be reduced to ~1 "unreal" event/day in the energy range under consideration.

Presented in the following sections are calculated results dealing with neutrino production and interaction rates, time dependence of the neutrino pulse, shielding considerations for neutrons coming from a spallation neutron source and from scattered neutrons from experimental areas, shielding considerations for galactic sources, especially muons, and finally detector responses to neutrino and background radiations. Many of the calculations are very detailed and were obtained by utilizing state of the art radiation transport codes. Some calculated results are only approximate because up to now only a superficial understanding of these processes, for example, wide angle bremsstrahlung for the muons (WAB), was necessary. In all cases, the results for the background should represent upper limits.

A generalized description of the calculational codes and data used are given in Section II and modifications of the codes as well as the calculated results are presented in Section III.

II. GENERALIZED DESCRIPTION OF THE RADIATION TRANSPORT CODES AND DATA

The Code HETC

The three-dimensional, multimedia, nucleon-meson transport code HETC[9)] uses Monte Carlo methods in conjunction with theoretical nuclear-interaction models to determine the energy, angle, and multiplicity of the particles produced in nucleon-nucleus and pion-nucleus (including pion capture) interactions. The Monte Carlo simulation of the particle transport involves selecting the energy, direction, and spatial coordinates of the primary particles from an input source description and computing individually the trajectories of the primary particles and the secondary particles produced by nuclear collisions and by pion and muon decay. The code takes into account charged-particle energy loss due to atomic ionization and excitation, multiple Coulomb scattering by the primary particles, elastic and nonelastic neutron collisions and nonelastic proton and pion collisions with nuclei other than hydrogen, elastic and nonelastic nucleon and pion collisions with hydrogen nuclei, pion and muon decay in flight and at rest, and negative-pion capture at rest. A brief description of the treatment of the various physical processes in HETC is given below. A more detailed discussion can be found in Ref.9).

For nonelastic collisions with nuclei other than hydrogen with atomic numbers $\gtrsim$ 4, the intranuclear-cascade-evaporation model is used for pion collisions at all energies and for nucleon collisions at energies $\gtrsim$ 15 MeV. For each collision, calculations using a subroutine version of Bertini's latest intranuclear-cascade program [10)] and a subroutine version of Guthrie's evaporation program[11)] are performed to determine the identity, multiplicity, energy, and direction of the emitted particles, and the charge, mass, and the excitation energy and recoil energy of the residual nucleus. The underlying assumption of the intranuclear cascade model is that the nuclear interactions by a incident particle can be treated as a series of two body collisions within the nucleus and that the location and resulting particles from this collision are governed by experimental and/or theoretical particle-particle total and differential cross section data. Nuclear potentials and intranuclear particle movement are determined by a zero temperature Fermi distribution. Particles which become "trapped" within the nucleus and holes produced in the Fermi sea constitute the excitation energy used by the evaporation model. The particles produced in the collision may be protons, neutrons, charged pions, or neutral pions from the intranuclear cascade, and protons, neutrons, deuterons, tritons, ^{3}He's, or alpha particles from the evaporation.

Above 15 MeV, neutron elastic collisions with nuclei other than hydrogen are taken into account using experimental data and results from optical-model calculations, and proton and pion elastic collisions with nuclei other than hydrogen are neglected. Elastic and nonelastic nucleon and pion collisions with hydrogen are treated using the same differential particle-particle cross sections as used in the intranuclear-cascade calculations.

Protons with energies $\lesssim$ 15 MeV and deuterons, tritons, ^{3}He's, alpha particles, and recoiling residual nuclei of all energies are assumed to slow down and come to rest without undergoing nuclear interaction. Furthermore, the slowing-down distance is neglected since, for the low energies involved, the range of these particles is usually very small.

Positively charged pions that come to rest are assumed to decay. Negatively charged pions that come to rest are assumed to undergo nuclear capture. An intranuclear-cascade-evaporation calculation is performed to determine the capture products, and the nucleons and charged pions produced are included in the transport calculations. The type of nucleus capturing the pion is determined using the Fermi-Teller Z-law, i.e., the probability of final capture by a nucleus of charge Z (excluding hydrogen) is taken to be proportional to Z times the atom density of Z-type nuclei.

Charged particle elastic scattering with nuclei other than hydrogen is not included in HETC. The energy loss and angular changes in such collisions are small, and therefore, this should not have an important effect on the results since it is expected that the laterial spread of the cascade and the spatial distribution of the energy deposition are predominantly governed by other process which are included in the code, i.e., multiple Coulomb scattering, nucleon and pion nonelastic collisions, neutron elastic collisions with all nuclei, and pion and nucleon elastic collisions with hydrogen.

Each particle in the cascade is followed until it eventually escapes from the target system, undergoes absorption, or comes to rest. A complete description of each "event" (nuclear interaction, stopped charged particle, etc.) that occurs during the computation of each particle history is stored on magnetic tape. These history tapes are then analyzed to obtain the results of interest. Thus, for a given source distribution and geometry material configuration, a single HETC transport calculation provides all of the information needed to compute, for example, absorbed dose, energy deposition, residual nuclei production as well as much useful ancillary information.

The results obtained using the HETC code have been successfully compared with experimental data many times. The application of HETC in this work is to obtain a neutron spectrum from a spallation target to be used in the shielding calculations, and to obtain the number of produced neutrinos.

The Code EGS

EGS along with its cross section processing counterpart PEGS is a three-dimensional multimedia analog Monte Carlo e^-, e^+, and gamma ray transport code[12)]. The source particles for EGS can be defined in the code itself or can be taken from the HETC collision tape in terms of gamma rays from excited nuclei, gamma rays from π^0 decay, and $e^\pm$ from $\mu^\pm$ decay. The code is highly utilized for shielding calculations and detector design calculations. Specific application of the code in this paper will be for detector design calculations and shielding considerations. The code is very detailed and takes into account all important physical processes, for example, pair production, compton, photoabsorption, e^-e^--interactions, e^+e^--interactions, annihilation, bremsstrahlung, etc.. Results obtained from the code have successfully been compared with experimental data.

The code MORSE

Neutron collisions with all nuclei in the energy range from ~15 MeV to thermal are treated by using experimental cross section data and the three-dimensional Monte Carlo neutron and gamma ray multimedia transport code MORSE[13)]. Some general features of the code are

1) uses multigroup cross sections sets which can be generated from ENDFB cross section data

2) anisotropic scattering can be utilized

3) includes time dependence

4) includes a generalized three-dimensional geometry package

5) solution of a given problem may be obtained in either the forward or adjoint mode

6) much of the drudgery associated with flux estimation, biasing, and data handling has been reduced,

7) it is not an analog Monte Carlo program, i.e., weighting and averaging are used to describe many of the physical phenomena.

Multigroup cross sections represent cross sections which have been averaged over a given energy range and all particles within that energy range are required to behave according to that average cross section. A group averaged cross section can be defined as follows

$$\sigma_j = \int_{E_j}^{E_{j+1}} \sigma(E)\phi(E)dE / \int_{E_j}^{E_{j+1}} \phi(E)dE$$

where $\phi(E)$ is an appropriate flux weighting factor. When particles have collisions they scatter from group to group rather than from a specific energy to a specific energy.

A simplistic view of the way MORSE (and HETC and EGS) using Monte Carlo techniques solves the transport equation is as follows:

1) pick a source particle from an HETC tape or define a source particle,

2) obtain cross section and select a travel distance to the collision site,

3) if the travel distance is in the system and no medium change has occured, transport the particle to the new position; obtain new energy, direction, and weight of particle, (store any produced particles, and go to step 2),

4) if the travel distance is out of the system, transport the particle to the boundary and obtain a previously produced particle, if any, and go to step 2) or go to step 1),

5) if the total travel distance places the particle in another cross section media, transport the particle to the boundary separating the media, and go to step 2).

MORSE is a powerful code and can serve in other ways than to transport neutrons and gamma rays. MORSE has been used with minimum modification to do cryogenic pump design calculations and has been used in this paper to do scintillation light transport. However, the major purpose of the code is for reactor and shielding design calculations.

The codes ANISN, TDA and DOT

The radiation transport codes ANISN[14)], TDA[15)] and DOT[16)] employ the discrete ordinates method coupled with a multigroup approximation to the continuous energy variable to obtain deterministic solutions of the Boltzmann transport equation. These codes are widely accepted in the shielding community and have been used extensively for deep penetration shielding problems where Monte Carlo methods are sometimes unacceptable due to statistical difficulties. ANISN and TDA solve the one-dimensional form of the Boltzmann transport equation in slab, cylindrical, or spherical geometries whereas DOT solves the two-dimensional form in slab and R-Z or R-θ cylindrical geometries. Both ANISN and DOT are time-independent codes and as such yield only steady state solutions. TDA, which stands for Time Dependent ANISN, ultilizes a finite difference approximation to the particle density time derivative to obtain time-dependent solutions. For point impulse sources, TDA employs a semi-analytic uncollided or first flight estimations procedure. This procedure conserves the time-distance relationships for the uncollided particles and coupled with the finite difference approximation provides highly reliable impulse responses which may be convoluted with the actual source time structure to obtain excellent one-dimensional transient solutions. These codes will be used for radiation transport through the thick shields considered in this paper.

The multigroup cross section set: Jörg[17)]

Since many mean free path of material are required for the shielding considered in this paper, Monte Carlo methods are not directly applicable to transporting particles through such great distances. Therefore, the discrete ordinate methods just described must be used. This introduces the problem of what cross sections should be used above 15 MeV. Since the upper energy range of interest here for shielding will be in the hundreds of MeV and since it is the neutrons and secondary gamma rays which will penetrate the deepest, neutron noneleastic total and differential cross sections have been calculated for a variety of elements for energies > 15 MeV and $\leq$ 400 MeV by utilizing the intranuclear-cascade-evaporation model described in the HETC section. By combining high energy ($15 \leq E \leq 400$ MeV) elastic data with the nonelastic calculated data and by using ENDFB-4 data for neutrons and gamma rays with energies < 15 MeV, it is possible to construct a multigroup neutron cross section set which includes all energies from thermal to 400 MeV and a coupled gamma ray cross section set from 0.01 MeV to 15 MeV. Only gamma rays produced by neutrons with energies $\leq$ 15 MeV are included. The cross sections are represented by a P_5 Legendre expension. However, for most of the calculations presented here, only a P_4 corrected P_3 cross section set has been used.

III. RESULTS AND CODE MODIFICATIONS

A) Neutrino Production:
Calculation of Neutrino fluxes from the Spallation Source.

The HETC code without modifications gives no information on the neutrinos produced from charged pion or muon decay. However, the code does correctly pick the decay sites of these particles. Since the pion decay to a muon and a neutrino is a two body final state, all necessary information for the kinematic calculation is available if an assumption about the particle emission in the center of momentum system of the decaying pion is made . For these calculations this angular distribution has been assumed to be isotropic. For the decay of the muon to a three body final state a phase space calculation is performed by assuming isotropic center of momentum emission of each emitted fragment during the decay process. For negatively charged pions which slow to rest, no decay is allowed and all of these particles are assumed to be captured by the nuclei of the medium. Since relatively low energy proton beams are being considered here (< 2 GeV), the produced pions (those which do not interact) will very quickly slow to rest ($\sim 10^{-10}$ s). Due to this, very few of the pions will decay in flight and the majority of the neutrinos will come from decay at rest. Since negative pions are captured when they slow to rest, practically only the positive pions and the positive muons play any role for neutrino research at a spallation neutron source.

The results of several HETC calculations which yield the total number of ν_μ from π^+ decay as a function of proton energy and target material are presented in fig.1. A fit to this data yields the following expression and coefficients:

$$y = ax + b.$$

Target Material	Coefficients a	Coefficients b
^{27}Al	3.46×10^{-4}	-0.152
^{56}Fe	2.92×10^{-4}	-0.127
^{101}Ru	2.50×10^{-4}	-0.110
^{159}Tb	2.16×10^{-4}	-0.095
^{208}Pb	2.06×10^{-4}	-0.095
^{238}U	1.95×10^{-4}	-0.090

where y is the number of ν_μ produced per proton and x is the energy of the incident protons in MeV.

The number of $\bar{\nu}_\mu$ and ν_e from μ^+ decay can also be obtained from the above data.

An experiment has been performed by H.Chen et al. to determine the number of stopped π^+ when 720 MeV protons are incident on a Cu beam dump[18]. The number obtained was 0.0571 ± 0.0035 stopped π^+/720 MeV proton incident. Even though the details of the experiment are not reproduced here, the results obtained above can be used to approximately calculate the same number. The calculated result is 0.085 which is approximately 50% higher than the experimental value. It is possible due to rejection procedures employed in the experiment that the experimental number is low. For design considerations, the calculated values will be used.

The energy dependent ν_μ flux from π^+ decay and the $\bar{\nu}_\mu + \nu_e$ flux from μ^+ decay at 6 m from the spallation source for 1.1 GeV protons incident on a Pb target are given in fig.2. The π^+ point above ~30 MeV represents the muon neutrino from π^+ decay at rest.

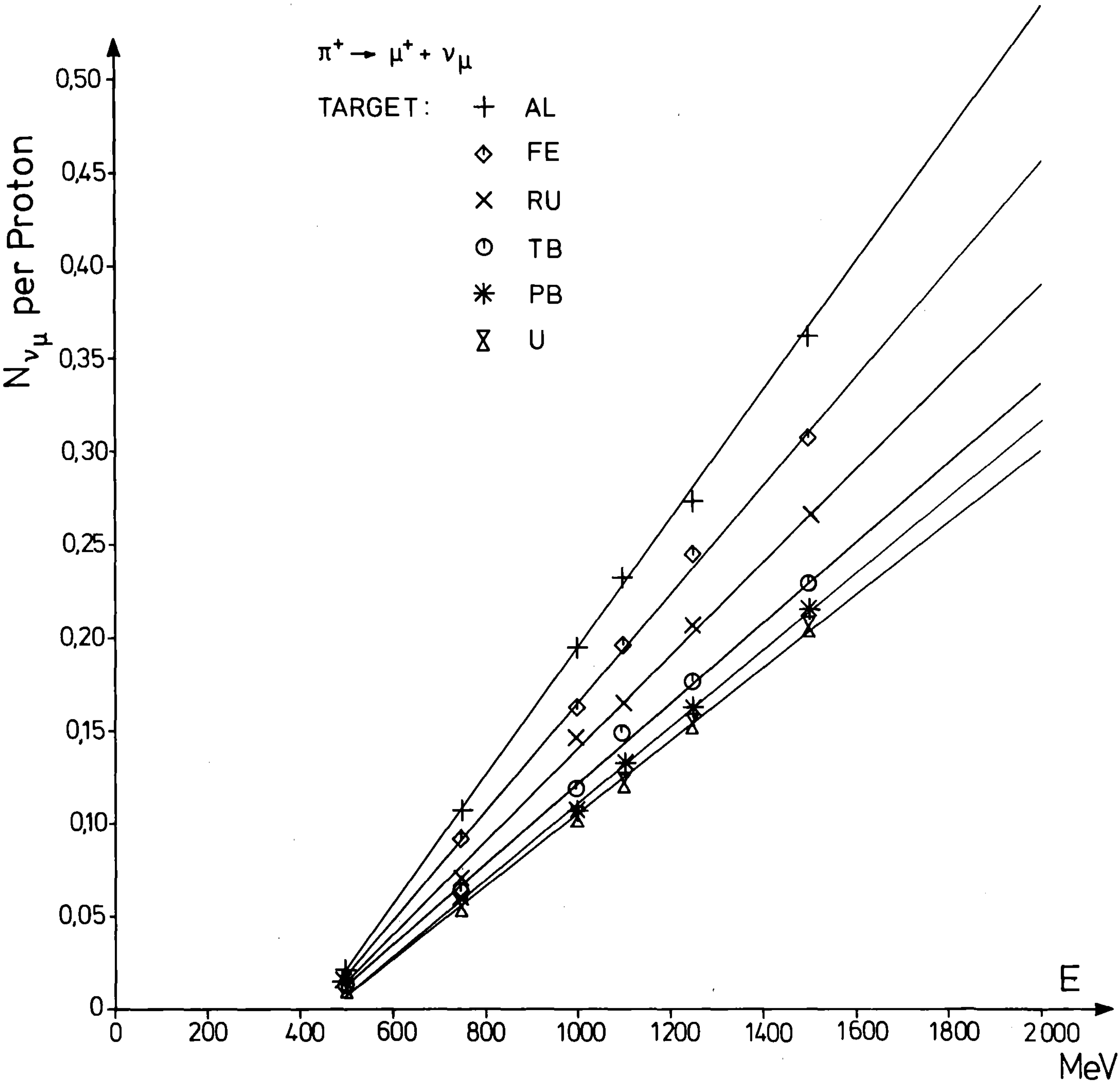

Fig.1: The number of ν_μ produced per proton as a function of proton energy and target material

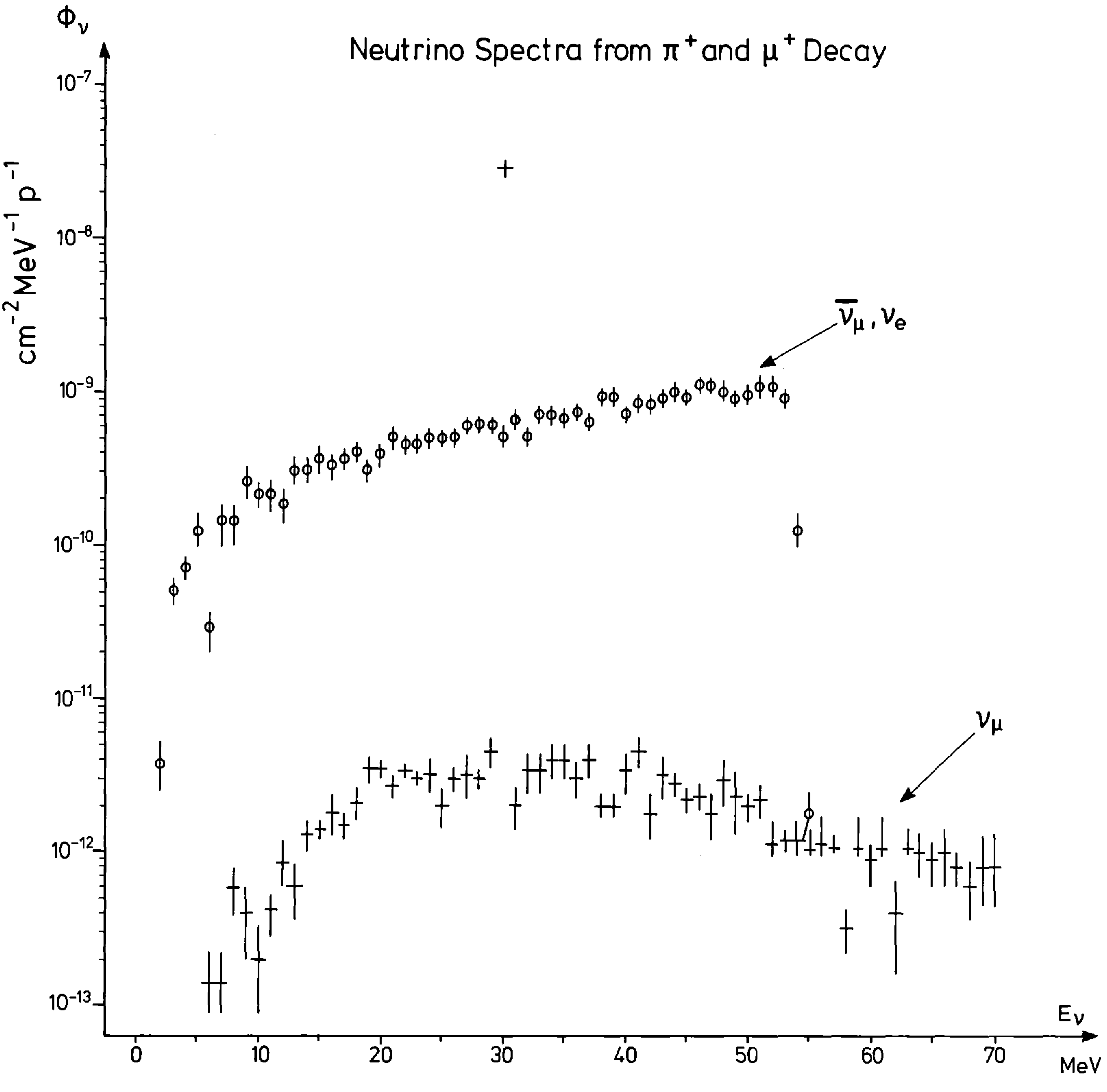

Fig.2: Energy dependent neutrino flux at 6 m for 1.1 GeV protons incident on a Pb target

A closer inspection of the $\bar{\nu}_\mu + \nu_e$ spectrum from μ^+ decay is given in fig.3. Since a phase space type calculation was used to describe the energy dependence of these neutrinos, this energy flux spectrum is only in rough agreement with the spectra calculated from detailed theory (see fig.4).

The time dependence of the neutrinos from π^+ and μ^+ decay are presentend in fig.5 assuming a 200 nsec proton pulse width with a frequency of 100 Hz and an average proton current of 1 mA. The ν_μ neutrinos will come with the proton pulse but the ν_e and $\bar{\nu}_\mu$ neutrinos will come much slower due to the longer lifetime of the muon.

To represent the time dependence of the neutrinos reaching the detector at a distance of 12 m, the time scale in fig.5 must be shifted by ~40 nsec.

The equations used to calculate the time dependence of the neutrino are given below

$$\phi_{\nu_\mu} = Q_o(1-e^{-\lambda_\pi t}) \qquad t < t_p$$

$$\phi_{\nu_\mu} = Q_o(e^{\lambda_\pi t_p}-1)e^{-\lambda_\pi t} \qquad t > t_p$$

for the π^+ decays and

$$\phi_{\nu_e,\bar{\nu}_\mu} = Q_o[(1-e^{-\lambda_\mu t})+\frac{\lambda_\mu}{\lambda_\pi-\lambda_\mu}(e^{-\lambda_\pi t} \quad e^{-\lambda_\mu t})] \qquad t < t_p$$

$$\phi_{\nu_e,\bar{\nu}_\mu} = Q_o \frac{\lambda_\mu}{\lambda_\mu-\lambda_\pi}(e^{\lambda_\pi t_p}-1)[e^{-\lambda_\pi t}-e^{(\lambda_\mu-\lambda_\pi)t_2-\lambda_\mu t}]$$
$$+ Q_o(e^{\lambda_\mu t_p}-1)e^{-\lambda_\mu t}$$
$$- Q_o(\frac{\lambda_\mu}{\lambda_\mu-\lambda_\pi})(e^{(\lambda_\mu-\lambda_\pi)t_2}-1)e^{-\lambda_\mu t} \qquad t > t_p$$

for the μ^+ decays

where:

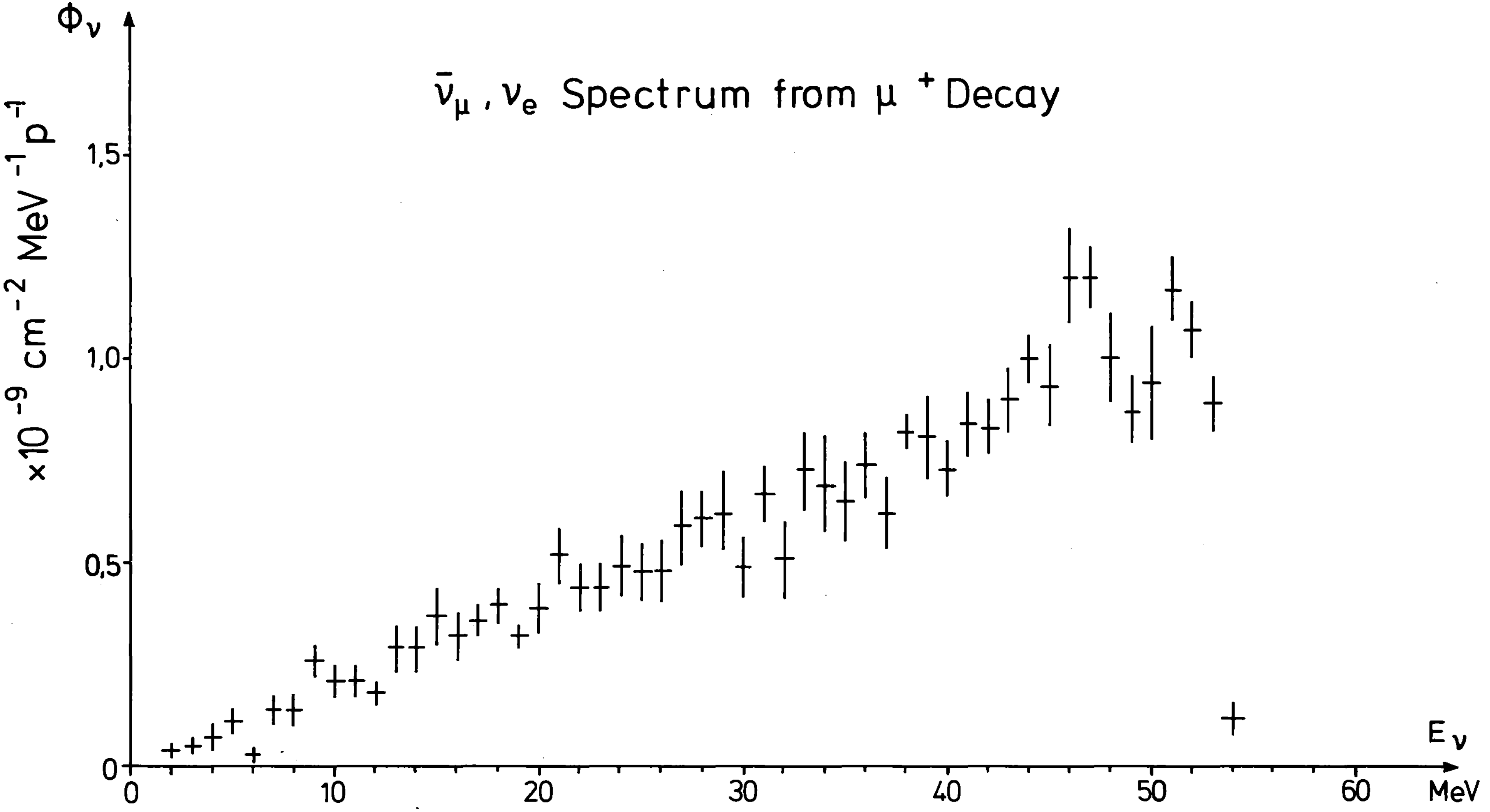

Fig.3: Energy dependent $\bar{\nu}_\mu + \nu_e$ flux at 6 m from 1.1 GeV protons incident on a Pb target

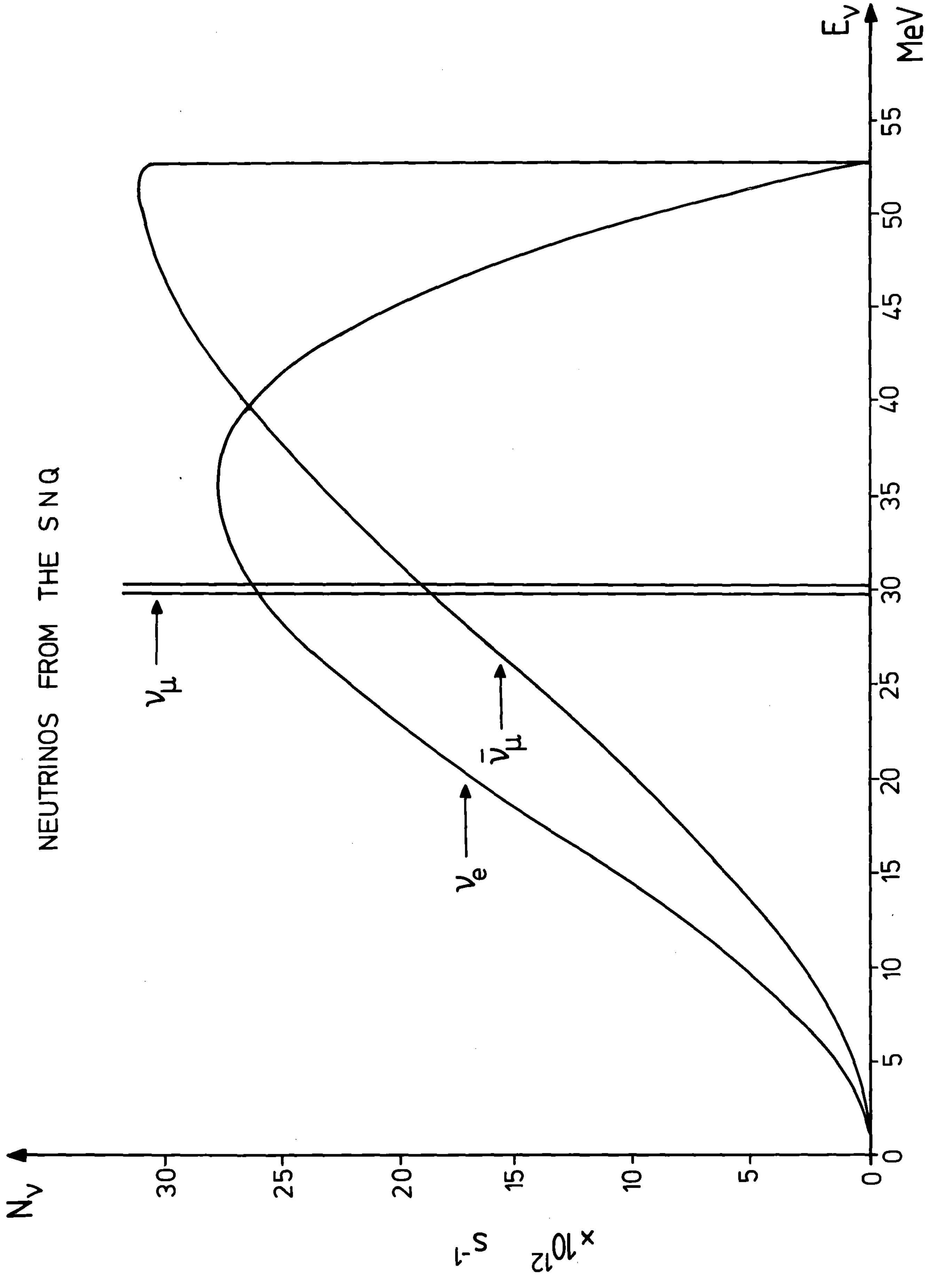

Fig.4: Energy distributions of the neutrinos generated at the spallation neutron source (beamstop). The total numbers of all three kinds of neutrino are equal. The indicated source strengths apply to a 1 mA averaged proton current for E_p = 1100 MeV.

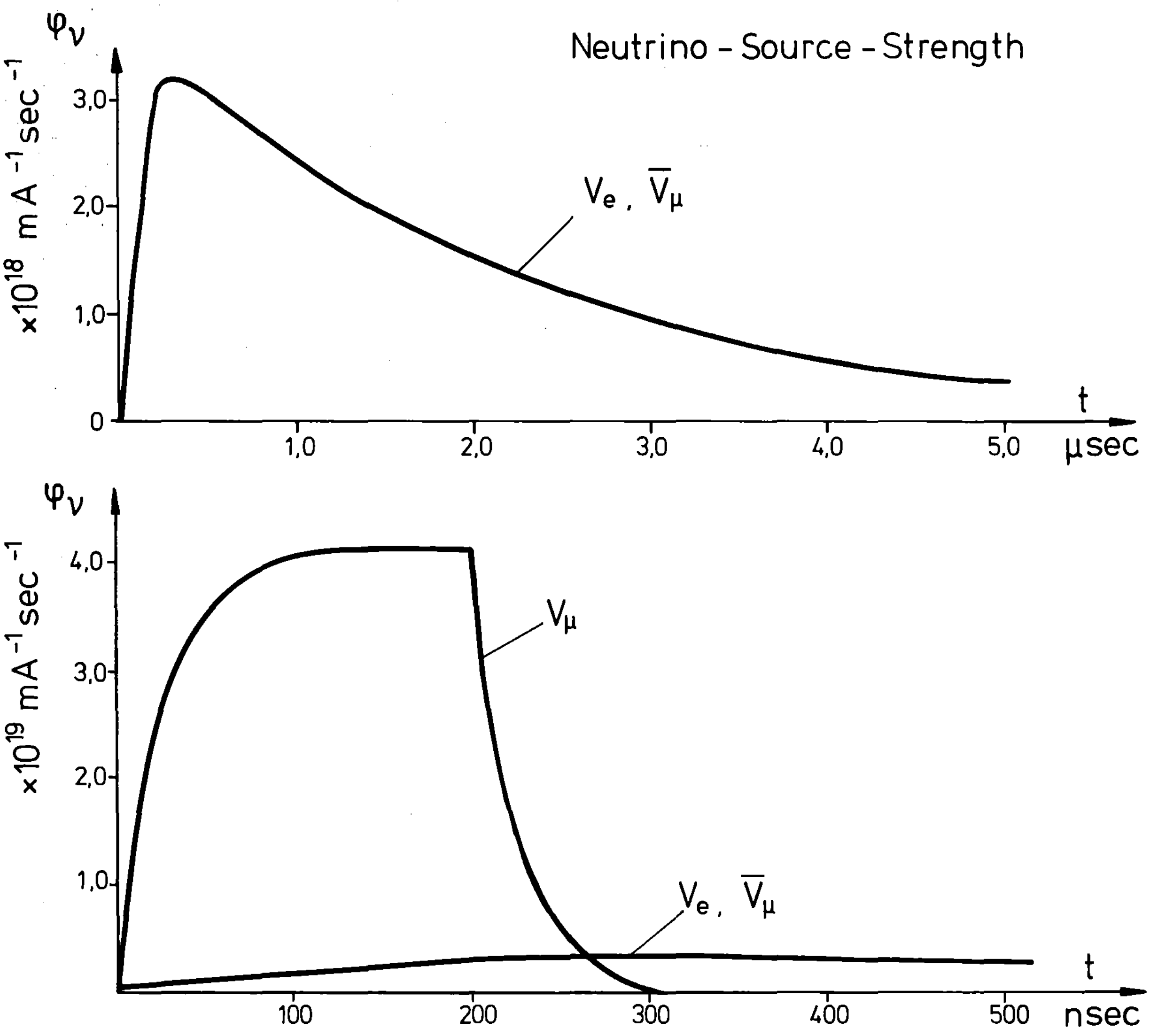

Fig.5: Time dependence of the neutrino source at the spallation neutron source (t_p = 200 ns, $\bar{I}_p$ = 1 mA, f = 100 Hz).

t_p = the pulse lenght, $\lambda_\mu = \frac{1}{\tau^{\mu}_{1/2}}$, $\lambda_\pi = \frac{1}{\tau^{\pi}_{1/2}}$ and
$\tau_{1/2}$ = 1/2 lifetime of the π and μ and:

$$Q_o = 0.133\ \frac{\nu}{p} \cdot \frac{6.25\mathrm{x}10^{15}\ \mathrm{p}/(\mathrm{mA \cdot sec})}{100\ \frac{\mathrm{pulses}}{\mathrm{sec}} \cdot 200\mathrm{x}10^{-9}\ \mathrm{sec/pulse}} = 4.16\mathrm{x}10^{19}\ \frac{\nu}{\mathrm{mA \cdot sec}}$$

Using the energy averaged cross sections of various neutrino interactions of interest presented in Ref.19 and the production levels of neutrinos for 1.1 GeV protons incident on a Pb target, the counting rate in the detector located an average distance of 12 m away can be calculated. These results are present in Table 1. At distances $\gtrsim$ 6 m from the target, the neutrino source appears as a point isotropic source since most of these particles are from pions and muons decaying at rest and, therefore, the data presented in the previous figures can be scaled relative to R^{-2}.

The numbers in Table 1 will be useful for comparison when the data concerning background event rates are presented in later sections. Due to the very small event rates, the background for various sources must be reduced to as low a level as possible so that true neutrino interaction events can be detected and analyzed.

Table 1: Cross Sections and Counting Rates Typical for Neutrinos at the Spallation Neutron Source

Reaction	Mean Energy MeV	σ_{tot} (cm^2)	Counting Rate* (day.mA.ton)$^{-1}$	Remarks
$\nu_e + d \rightarrow p + p + e^-$	37	$5 \cdot 10^{-41}$	29	
$\nu_e + {}^{12}C \rightarrow e^- + {}^{12}N$ (11 ms)	37	$1.5 \cdot 10^{-41}$	2.9	WSGIM theory
$\nu_e + e^- \rightarrow \nu_e + e^-$	37	$6 \cdot 10^{-43}$	0.74	V-A-theory
$\nu_\mu + e^- \rightarrow \nu_\mu + e^-$	30	$5 \cdot 10^{-44}$	0.062	
$\nu_\mu + {}^{12}C \rightarrow \nu_\mu' + {}^{12}C^*$(15.1 MeV)	30	$2.5 \cdot 10^{-42}$	0.48	WSGIM theory
$\nu_\mu + {}^{6}Li \rightarrow \nu_\mu' + {}^{6}Li^*$(3.56 MeV)	30	$1.5 \cdot 10^{-41}$	5.7	

*Counting rates at 12 m distance from the neutron source.
Target electrons per ton of organic scintillator.

B) Shielding:

1. Direct and Scattered Source Shielding

One potential background which must be reduced to a very low level so that the neutrino interaction events can be detected are the neutrons produced by the spallation source. Experiments at other accelerator facilities (LASL, for example) have shown that these neutrons can yield a substantial background and that many meters of iron are necessary to shield against them[4,8]. There are two ways neutrons can enter the neutrino detector area (see fig.6):

Those that come directly through the spallation source shield, and those that enter the experimental areas and then scatter into the neutrino detector area. This section considers these two potential backgrounds.

Direct Source Shielding

The HETC code, modified to take into account hadron-deuteron collisions, was used to calculate the neutron emission flux spectrum from the target moderator system shown in fig.7. This calculated flux spectrum will be used to determine the necessary shielding. HETC does not explicity include any mechanism to account for hadron-deuteron nonelastic collisions and the code was modified to include these interactions. Experimental total hadron-deuteron cross sections were used for the transport calculations, and phase space determined for nonelastic collisions the energy spectra of the secondary particles assuming isotropic center of momentum emission of each fragment breakup. Since the energy range of the transported particles is reasonably low, no pion production by hadron-deuteron collisions was considered. Elastic neutron-deuteron collisions were also included for energies up to 100 MeV. The 1.1 GeV proton beam was taken to be normally incident

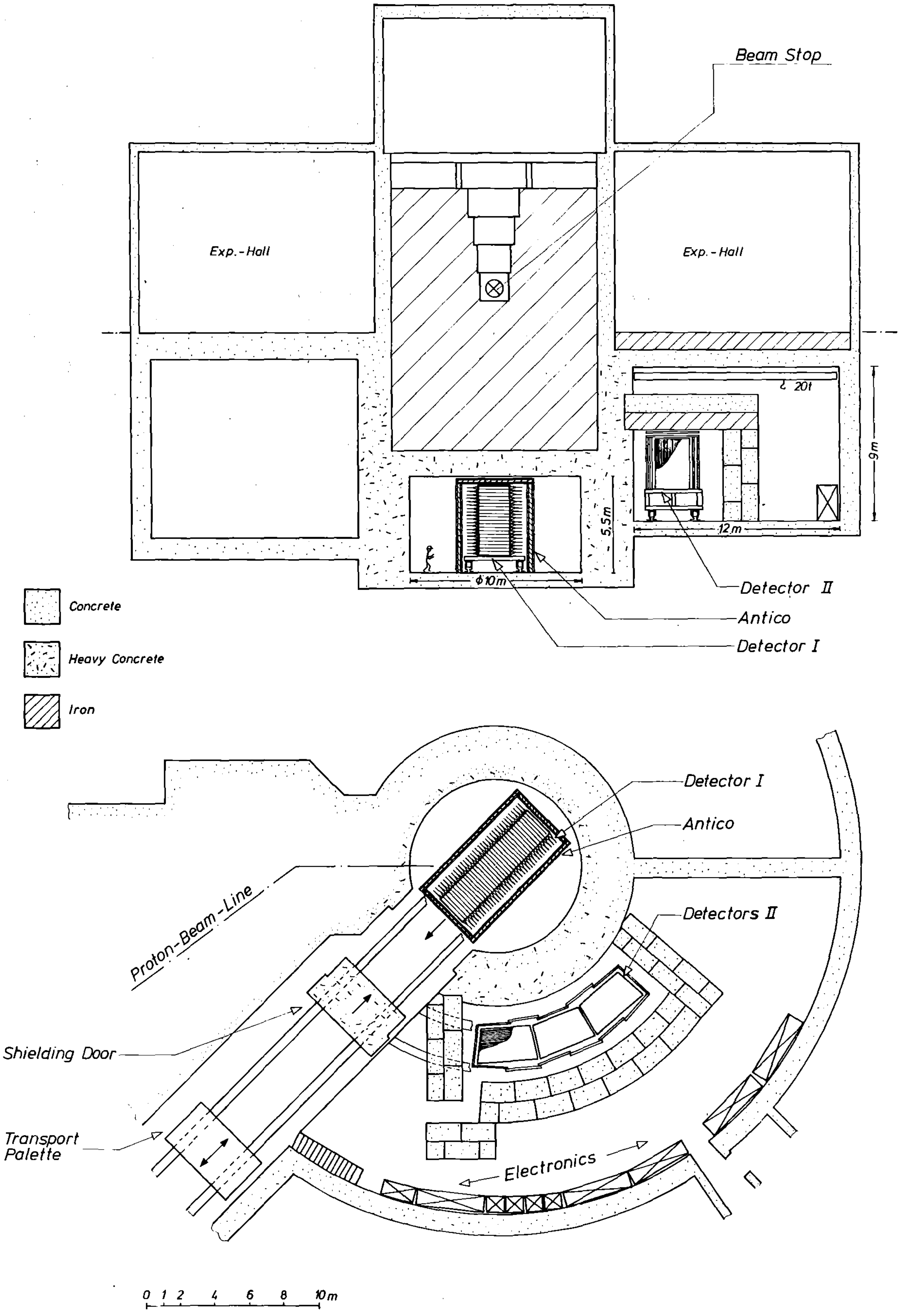

Fig.6: The neutrino facility at the spallation source

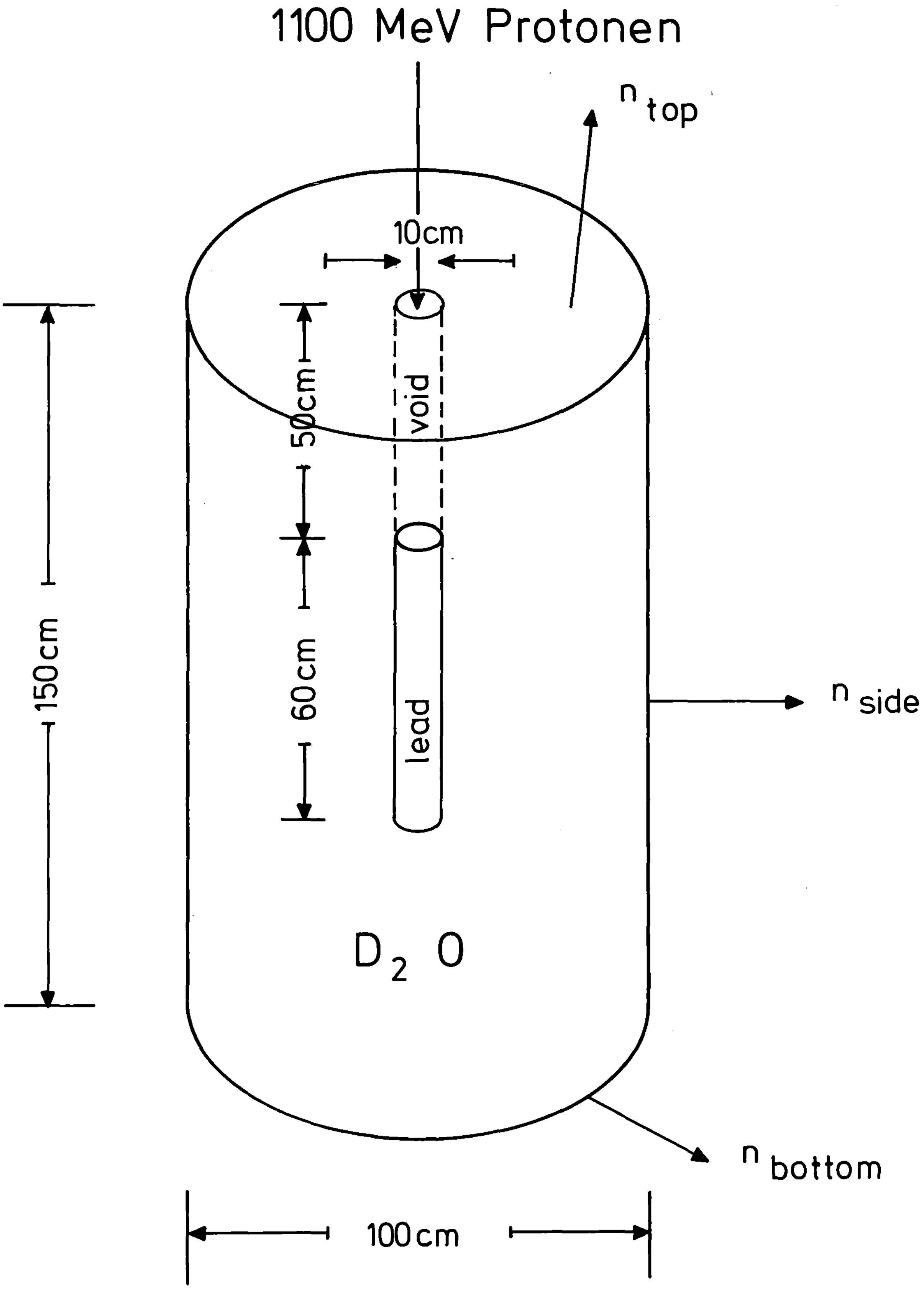

Fig.7: Geometry of the target-moderator system used in obtaining the neutron leakage flux for the detector shielding calculations.

on the center of the Pb target. The leakage flux spectra from the top, bottom, and side (Table 2) was combined to define the neutron source flux for the shielding calculations. Only neutrons with energies above 15 MeV need to be considered for the source since only high energy particles will contribute to the neutron flux at large distances into the shielding material. The calculated neutron leakage flux spectrum is given in fig.8 and Table 2. The partial neutron group structure used for these calculations as well as the total neutron and gamma ray group structure for later calculations is given in Table 3.

The shape and magnitude of the flux is almost totally determined by the leakage from the side of the moderator. The peak between 375 and 400 MeV is not physical but represents particles produced above 400 MeV as well as those produced between the above mentioned energies. Since cross sections for the discrete ordinates codes are only available to 400 MeV an attempt was made to incorporate particles produced above 400 MeV by conserving energy. The conserved energy particles which were produced above 400 MeV were given increased weight according to the following expression

$$Wt_{modified} = Wt_{actual} \cdot \frac{E_{actual}}{387.5}$$

Their energy was then reassigned to 387.5 MeV or the average energy associated with the last energy box shown in fig.8.

The integral of the flux over energy yields a value of 2.016×10^{-5} n/cm^2/p or for a proton beam current of 1 mA (6.25×10^{15} p/sec) 1.26×10^{11} n/(cm^2·sec·mA).

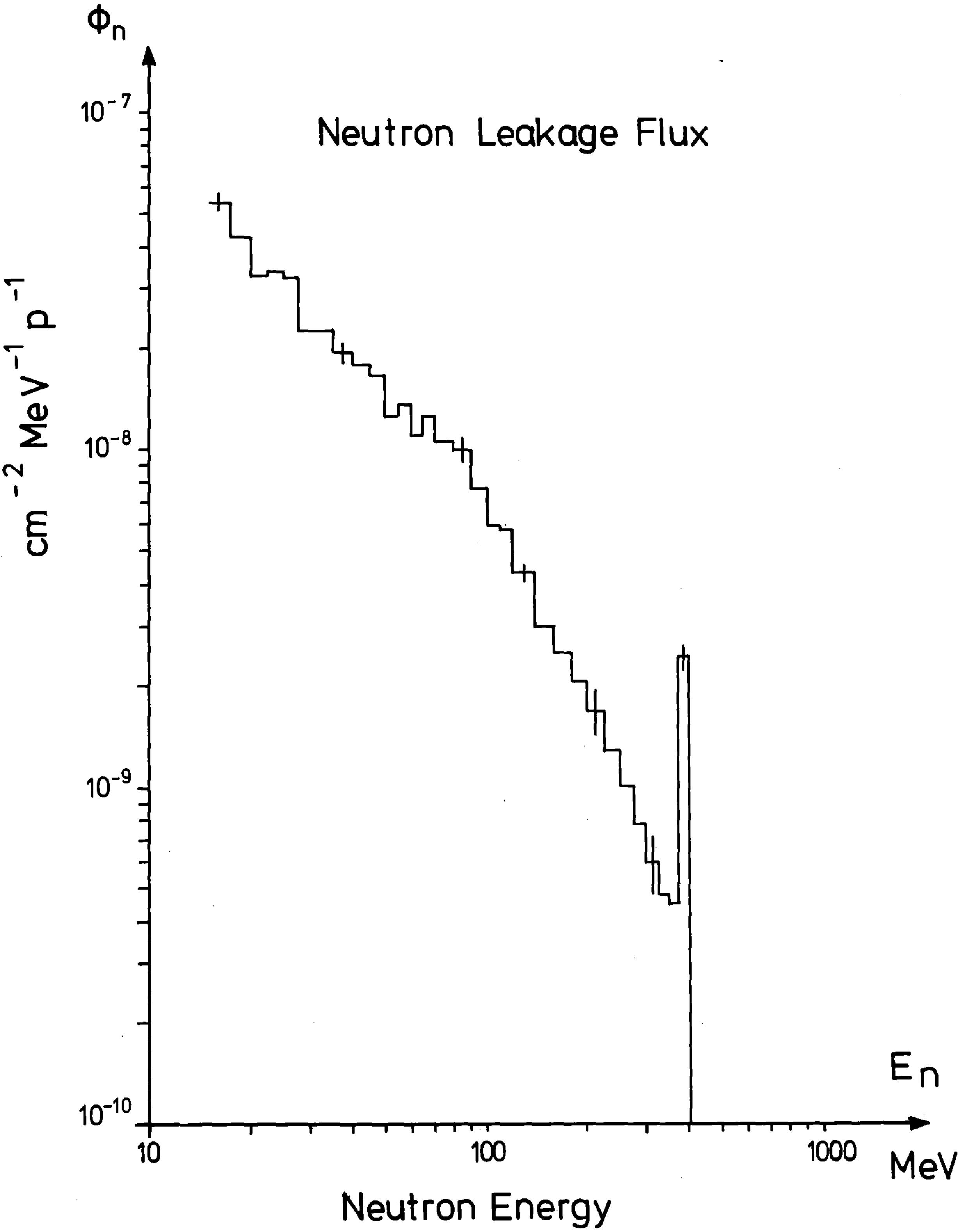

Fig.8: Neutron leakage flux spectrum produced by 1.1 GeV protons incident on a Pb target surrounded by a heavy water moderator (see fig.7).

Table 2: Spallation Source Neutrons for 1.1 GeV Protons Incident

Energy Range (MeV) and Group number		Neutron Flux (n/cm^2/proton) Side	Botton	Top	Total
400-375	1	4.42x10^{-7}	2.23x10^{-6}		6.11x10^{-7}
-350	2	1.08x10^{-7}	2.52x10^{-7}		1.12x10^{-7}
-325	3	1.05x10^{-7}	3.31x10^{-7}		1.20x10^{-7}
-300	4	1.61x10^{-7}	2.20x10^{-7}		1.48x10^{-7}
-275	5	1.98x10^{-7}	3.60x10^{-7}		1.93x10^{-7}
-250	6	2.61x10^{-7}	4.19x10^{-7}		2.49x10^{-7}
-225	7	3.48x10^{-7}	4.94x10^{-7}		3.23x10^{-7}
-200	8	4.71x10^{-7}	5.23x10^{-7}		4.19x10^{-7}
-180	9	4.71x10^{-7}	4.16x10^{-7}		4.05x10^{-7}
-160	10	5.63x10^{-7}	5.82x10^{-7}		4.95x10^{-7}
-140	11	6.55x10^{-7}	7.88x10^{-7}		5.89x10^{-7}
-120	12	9.23x10^{-7}	1.25x10^{-6}	7.27x10^{-8}	8.57x10^{-7}
-110	13	6.81x10^{-7}	4.93x10^{-7}	3.00x10^{-8}	5.76x10^{-7}
-100	14	6.67x10^{-7}	6.76x10^{-7}	8.23x10^{-8}	5.95x10^{-7}
- 90	15	8.72x10^{-7}	7.46x10^{-7}	1.19x10^{-7}	7.62x10^{-7}
- 80	16	1.19x10^{-6}	5.74x10^{-7}	2.30x10^{-7}	9.91x10^{-7}
- 70	17	1.17x10^{-6}	1.00x10^{-6}	2.21x10^{-7}	1.03x10^{-6}
- 65	18	7.19x10^{-7}	4.74x10^{-7}	1.39x10^{-7}	6.16x10^{-7}
- 60	19	6.25x10^{-7}	4.41x10^{-7}	2.02x10^{-7}	5.49x10^{-7}
- 55	20	7.93x10^{-7}	4.66x10^{-7}	8.45x10^{-8}	6.64x10^{-7}
- 50	21	7.43x10^{-7}	2.70x10^{-7}	1.67x10^{-7}	6.12x10^{-7}
- 45	22	9.67x10^{-7}	5.91x10^{-7}	2.54x10^{-7}	8.30x10^{-7}
- 40	23	1.08x10^{-6}	4.58x10^{-7}	2.12x10^{-7}	8.90x10^{-7}
- 35	24	1.10x10^{-6}	8.73x10^{-7}	2.48x10^{-7}	9.62x10^{-7}
- 30	25	1.32x10^{-6}	7.38x10^{-7}	3.85x10^{-7}	1.13x10^{-6}
- 27.5	26	6.90x10^{-7}	1.83x10^{-7}	1.41x10^{-7}	5.58x10^{-7}
- 25.0	27	9.55x10^{-7}	3.31x10^{-7}	3.61x10^{-7}	8.03x10^{-7}
- 22.5	28	9.77x10^{-7}	6.31x10^{-7}	2.52x10^{-7}	8.43x10^{-7}
- 20.0	29	9.51x10^{-7}	4.21x10^{-7}	3.41x10^{-7}	8.08x10^{-7}
- 17.5	30	1.25x10^{-6}	4.93x10^{-7}	5.83x10^{-7}	1.07x10^{-6}
17.5- 14.9	31	1.58x10^{-6}	5.34x10^{-7}	8.09x10^{-7}	1.35x10^{-6}

Table 3: Neutron and Gamma-Ray Group Structure

Group	Neutron Energy Interval (MeV)		
1	$4.00x10^{2}$	to	$3.75x10^{2}$
2	$3.75x10^{2}$	to	$3.50x10^{2}$
3	$3.50x10^{2}$	to	$3.25x10^{2}$
4	$3.25x10^{2}$	to	$3.00x10^{2}$
5	$3.00x10^{2}$	to	$2.75x10^{2}$
6	$2.75x10^{2}$	to	$2.50x10^{2}$
7	$2.50x10^{2}$	to	$2.25x10^{2}$
8	$2.25x10^{2}$	to	$2.00x10^{2}$
9	$2.00x10^{2}$	to	$1.80x10^{2}$
10	$1.80x10^{2}$	to	$1.60x10^{2}$
11	$1.60x10^{2}$	to	$1.40x10^{2}$
12	$1.40x10^{2}$	to	$1.20x10^{2}$
13	$1.20x10^{2}$	to	$1.10x10^{2}$
14	$1.10x10^{2}$	to	$1.00x10^{2}$
15	$1.00x10^{2}$	to	$9.00x10^{1}$
16	$9.00x10^{1}$	to	$8.00x10^{1}$
17	$8.00x10^{1}$	to	$7.00x10^{1}$
18	$7.00x10^{1}$	to	$6.50x10^{1}$
19	$6.50x10^{1}$	to	$6.00x10^{1}$
20	$6.00x10^{1}$	to	$5.50x10^{1}$
21	$5.50x10^{1}$	to	$5.00x10^{1}$
22	$5.00x10^{1}$	to	$4.50x10^{1}$
23	$4.50x10^{1}$	to	$4.00x10^{1}$
24	$4.00x10^{1}$	to	$3.50x10^{1}$
25	$3.50x10^{1}$	to	$3.00x10^{1}$
26	$3.00x10^{1}$	to	$2.75x10^{1}$
27	$2.75x10^{1}$	to	$2.50x10^{1}$
28	$2.50x10^{1}$	to	$2.25x10^{1}$
29	$2.25x10^{1}$	to	$2.00x10^{1}$
30	$2.00x10^{1}$	to	$1.75x10^{1}$
31	$1.75x10^{1}$	to	$1.49x10^{1}$
32	$1.49x10^{1}$	to	$1.35x10^{1}$
33	$1.35x10^{1}$	to	$1.22x10^{1}$
34	$1.22x10^{1}$	to	$1.00x10^{1}$
35	$1.00x10^{1}$	to	8.18
36	8.18	to	6.70
37	6.70	to	5.49
38	5.49	to	4.50
39	4.50	to	3.68
40	3.68	to	3.01
41	3.01	to	2.47
42	2.47	to	2.01
43	2.01	to	1.66
44	1.66	to	1.35
45	1.35	to	1.10
46	1.10	to	9.07-01
47	9.07-01	to	7.42-01
48	7.42-01	to	4.98-01
49	4.98-01	to	3.34-01
50	3.34-01	to	2.24-01
51	2.24-01	to	1.50-01
52	1.50-01	to	8.66-02
53	8.66-02	to	3.19-02
54	3.19-02	to	1.50-02
55	1.50-02	to	7.10-03
56	7.10-03	to	3.35-03
57	3.35-03	to	1.59-03
58	1.59-03	to	4.54-04
59	4.54-04	to	1.01-04
60	1.01-04	to	2.26-05
61	2.26-05	to	1.06-05
62	1.06-05	to	5.04-06
63	5.04-06	to	2.38-06
64	2.38-06	to	1.13-06
65	1.13-06	to	4.14-07
66	4.14-07	to	0

Group	Gamma Energy Interval (MeV)		
67	14.0	to	12.0
68	12.0	to	10.0
69	10.0	to	8.0
70	8.0	to	7.5
71	7.5	to	7.0
72	7.0	to	6.5
73	6.5	to	6.0
74	6.0	to	5.5
75	5.5	to	5.0
76	5.0	to	4.5
77	4.5	to	4.0
78	4.0	to	3.5
79	3.5	to	3.0
80	3.0	to	2.5
81	2.5	to	2.0
82	2.0	to	1.5
83	1.5	to	1.0
84	1.0	to	0.4
85	0.4	to	0.2
86	0.2	to	0.1
87	0.1	to	0.01

This large flux of fast neutrons (E > 15 MeV) must be reduced to an acceptable value so that the neutron and gamma rays event rates in the detector system is below that expected for the neutrinos. Since in this calculation the neutron leakage flux and current are approximately the same, an integration over the surface area yields (1.267 n/p) 7.92×10^{15} n/sec leaking from the target system per mA of 1.1 GeV proton beam current.

The neutron leakage flux spectrum shown in fig. 8 was used as an isotropic "shell source" in an ANISN calculation to determine the rate at which the neutron gamma ray flux and particle currents incident on the detector were reduced by varying the thickness of the iron shielding. The discrete ordinate approach was used for this calculation instead of Monte Carlo methods since many mean free paths of iron will be required for the shielding. A Monte Carlo approach would have required many biasing techniques and many hours of computation time to obtain any results at all. The geometry of the one-dimensional spherical system is shown in fig.9 and in Table 4 are the compositions of the various materials. The radius of the shell source was chosen such that the surface area of the sphere was equal to the cylindrical surface area of the target moderator system shown in fig.7. All of the calculated results are for an S_8 quadrature set and a P_3 expansion of the cross section set. Several calculations were carried out using a higher order quadrature set (S_{16}) and cross section expansion (P_5), but the results were comparable (less then a factor of 2 lower) to those obtained with S_8P_3.

The results of the flux attenuation calculations are shown in fig.10 for up to 8 meters of iron. Plotted in the figure as function of the radial thickness of the iron is the integral of the neutron and secondary gamma ray flux. Notice that the integral is

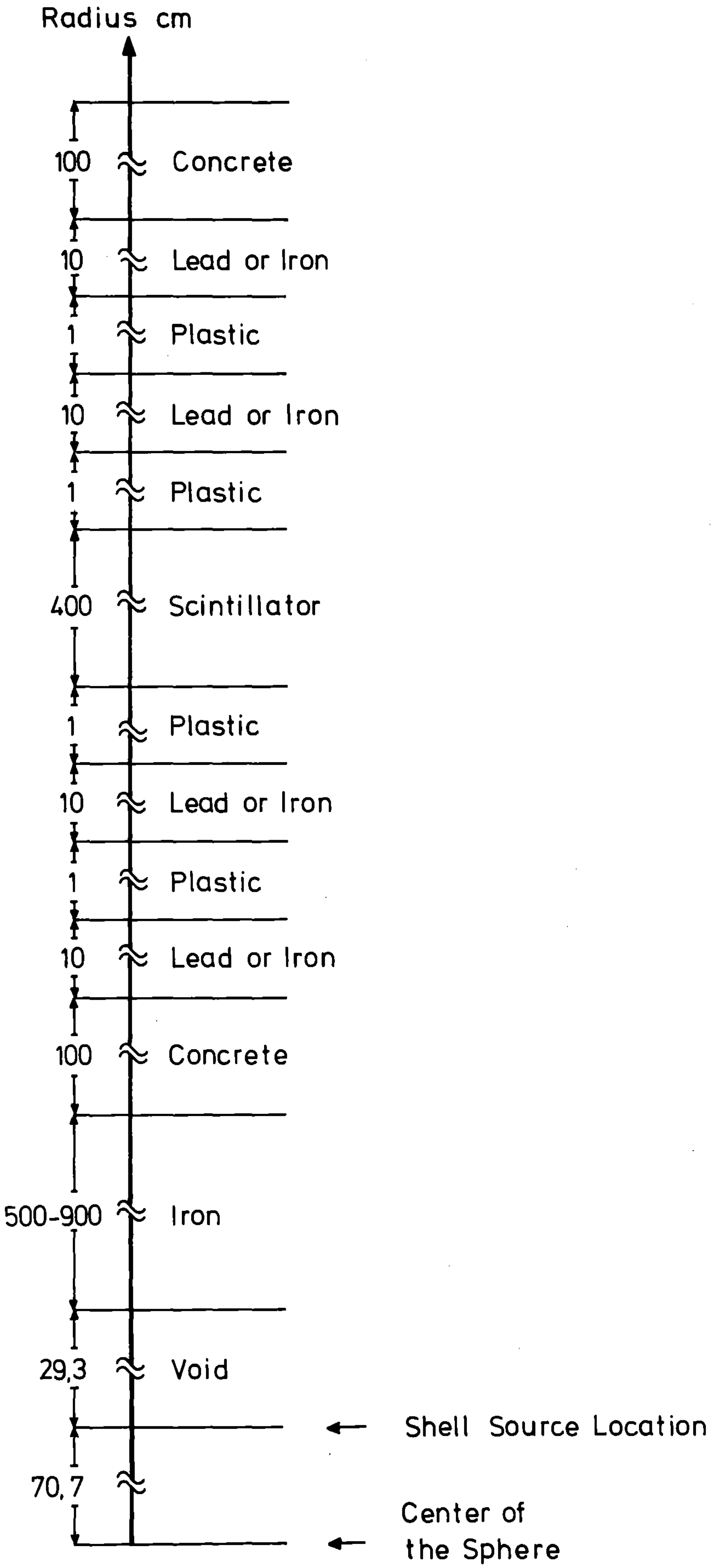

Fig.9: One dimensional spherical geometry for the direct source shielding calculation

(Dimension in cm.)

Table 4: Density and Composition of the Materials used in the Shielding Calculations

Material	Density (g/cm^3)	Nuclei density (atoms/b·cm)
Fe	7.86	8.49×10^{-2}
Concrete	3.50	
Si		5.31×10^{-4}
Al		1.59×10^{-4}
Fe		2.37×10^{-2}
Ca		1.72×10^{-3}
Mg		9.22×10^{-5}
S		4.63×10^{-5}
C		3.66×10^{-5}
B^{10}		2.24×10^{-3}
B^{11}		6.34×10^{-3}
H		1.04×10^{-2}
O		4.24×10^{-2}
Pb	11.35	3.30×10^{-2}
Scintillator	0.89	
C		4.01×10^{-2}
H		4.87×10^{-2}

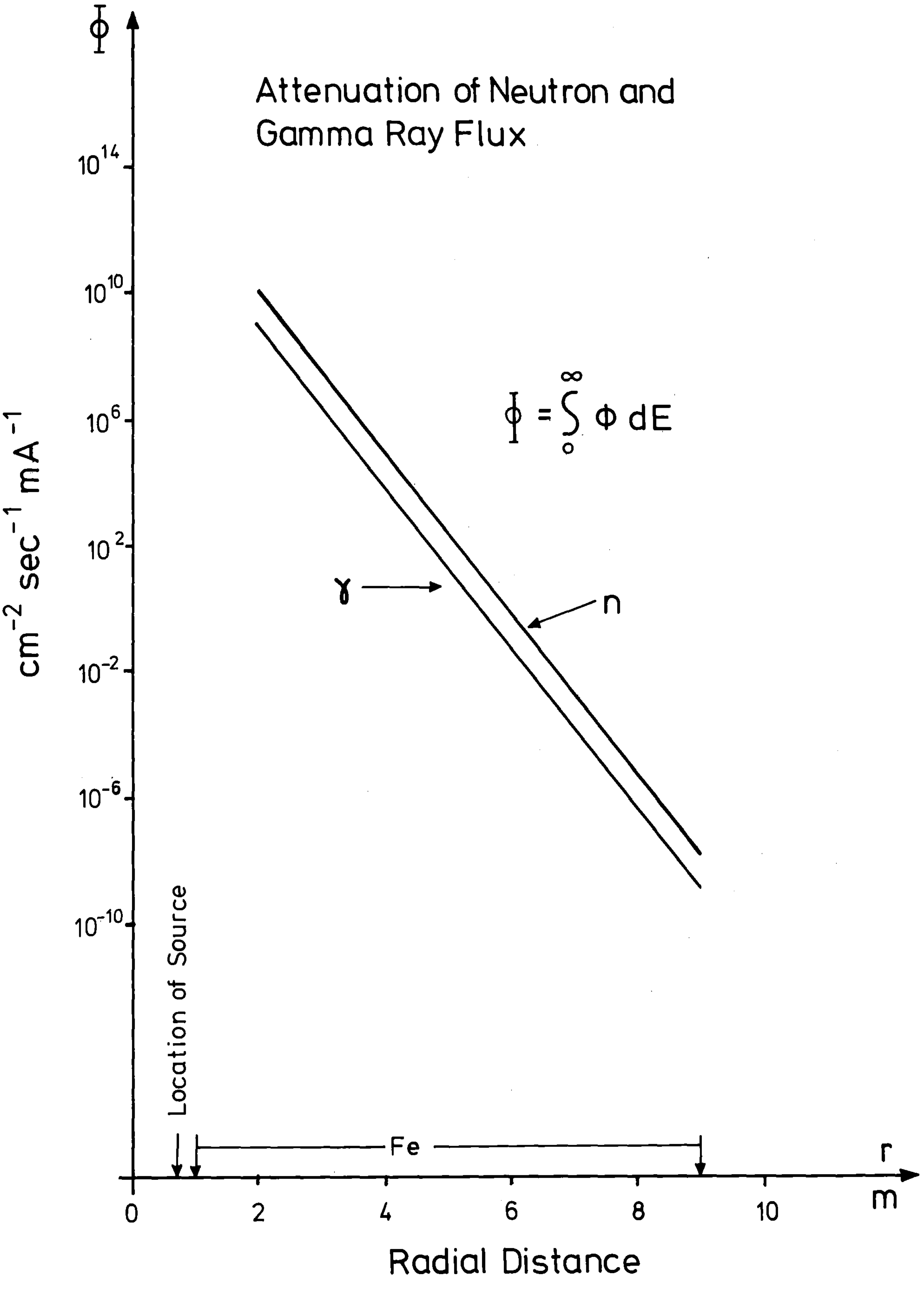

Fig.10: Attenuation of the neutron and gamma ray flux as a function of iron shield thickness.

over all energies. Since neutrons below 15 MeV and all gamma rays from the target were emitted from the source, no data is given until an iron thickness of 1 m. By this thickness of iron, the effect on the plotted results of the low energy neutrons and gamma rays from the source would be neglible.

The energy dependence of the neutron and gamma ray currents entering the detector system for various thickness of iron shielding are given in Table 5. The results are normalized to a 1 mA, 1.1 GeV proton beam and the surface area taken for the detector system is 150x833 cm^2. For 8 m of iron shielding, the neutron and gamma event rates will be < 1/day. Also given in Table 5 for the 8 m iron case, are the results when directly around the detector is placed 20 cm of lead instead of iron. The reduction in the gamma current is obvious. The high energy particles (group 1 - 35 for the neutrons and group 67 - 74 for the gamma rays) can produce pulses in the detector which are within the energy range and within the time gate of the neutrino induced interactions. In addition, these high energy particles will produce many low energy particles which in combination with the low energy particles entering the system may lead to a pile up effect of low pulse height signals. As a measure of this, the reaction rates/day for a 50 ton detector are given in Table 6 as a function of energy for an 8 m iron shield. Since these interactions are dominated by low energy neutrons, the time dependence of these interactions can possibly be used to differentiate between real and unreal neutrino interactions.

The TDA code has been used to calculate the time dependence of the neutron and gamma flux at the front edge of the detector. The same geometry as used for the ANISN calculations has been employed here except the source has been moved to the center of the concentric spheres. This was done so that in the calculation, the

Grps	$\mathrm{Neutrons}\cdot d^{-1}\cdot mA^{-1}$						Ratio [a]
	Shield Thickness						8m
	5m	6m	7m	8m	8m+	9m	J^{+}/ϕ
1- 5	$5.50x10^{3}$	$1.19x10^{1}$	$2.54x10^{-2}$	$5.34x10^{-3}$	$6.02x10^{-5}$	$1.13x10^{-7}$	0.918
6-10	$7.22x10^{4}$	$1.97x10^{2}$	$5.29x10^{-1}$	$1.38x10^{-3}$	$1.49x10^{-3}$	$3.55x10^{-6}$	0.893
11-15	$1.67x10^{5}$	$4.86x10^{2}$	$1.38x10^{0}$	$3.82x10^{-3}$	$3.99x10^{-3}$	$1.03x10^{-5}$	0.828
16-20	$1,17x10^{5}$	$3.41x10^{2}$	$9.66x10^{-1}$	$3.70x10^{-3}$	$2.88x10^{-3}$	$7.21x10^{-6}$	0.720
21-25	$8.93x10^{5}$	$2.58x10^{2}$	$7.28x10^{-1}$	$2.01x10^{-3}$	$2.43x10^{-3}$	$5.41x10^{-6}$	0.609
26-30	$5.64x10^{4}$	$1.63x10^{2}$	$4.58x10^{-1}$	$1.26x10^{-3}$	$1.58x10^{-3}$	$3.39x10^{-6}$	0.557
31-35	$5.44x10^{4}$	$1.57x10^{2}$	$4.40x10^{-1}$	$1.21x10^{-3}$	$1.72x10^{-3}$	$3.24x10^{-6}$	0.486
36-40	$1.02x10^{5}$	$2.93x10^{2}$	$8.21x10^{-1}$	$2.26x10^{-3}$	$3.98x10^{-3}$	$6.04x10^{-6}$	0.459
41-45	$2.44x10^{5}$	$7.01x10^{2}$	$1.96x10^{0}$	$5.40x10^{-3}$	$2.03x10^{-2}$	$1.45x10^{-5}$	0.491
46-50	$6.54x10^{5}$	$1.88x10^{3}$	$5.29x10^{0}$	$1.45x10^{-2}$	$3.58x10^{-2}$	$3.90x10^{-5}$	0.501
51-55	$4.80x10^{5}$	$1.38x10^{3}$	$3.89x10^{0}$	$1.05x10^{-2}$	$2.37x10^{-2}$	$2.87x10^{-5}$	0.382
56-60	$4.46x10^{5}$	$1.28x10^{3}$	$3.62x10^{0}$	$9.68x10^{-3}$	$2.45x10^{-2}$	$2.67x10^{-5}$	0.298
61-65	$2.34x10^{5}$	$6.73x10^{2}$	$1.90x10^{0}$	$5.09x10^{-3}$	$1.50x10^{-2}$	$1.40x10^{-5}$	0.262
66	$9.84x10^{5}$	$2.84x10^{3}$	$7.97x10^{0}$	$2.38x10^{-2}$	$1.25x10^{-1}$	$5.88x10^{-5}$	0.214
	$\mathrm{Gammas}\cdot d^{-1}\cdot mA^{-1}$						
67-70	$1.07x10^{5}$	$3.08x10^{2}$	$8.65x10^{-1}$	$2.52x10^{-3}$	$1.58x10^{-7}$	$6.38x10^{-6}$	0.447
71-74	$6.21x10^{4}$	$1.54x10^{2}$	$4.34x10^{-1}$	$1.26x10^{-3}$	$9.91x10^{-4}$	$3.20x10^{-6}$	0.447
75-78	$5.67x10^{4}$	$1.63x10^{2}$	$4.59x10^{-1}$	$1.32x10^{-3}$	$1.78x10^{-4}$	$3.38x10^{-6}$	0.369
79-82	$1.51x10^{5}$	$4.83x10^{2}$	$1.36x10^{0}$	$3.90x10^{-3}$	$4.13x10^{-3}$	$9.98x10^{-6}$	0.138
83-87	$8.03x10^{5}$	$2.31x10^{2}$	$6.51x10^{0}$	$1.82x10^{-2}$	$7.54x10^{-3}$	$4.80x10^{-5}$	0.254

+Pb around detector; a: Detector size $150x833x400\ cm^{3}$

Table 5: Particles Entering the Detector System from the Spallation Source as a Function of Energy and Iron Shield Thickness [a]

Table 6: Reaction Rates per Day in a 50 Ton Scintillation Detector System shielded by eight Meters of Iron

	Reactions·d^{-1}·mA^{-1}				
Grps	n-C	γ-C	n-H	γ-H	Average Flux in Detector [a] (n/(cm^2·day/mA))
1- 5	4.05x10^{-5}		6.54x10^{-6}		7.77x10^{-11}
-10	1.09x10^{-3}		2.04x10^{-4}		2.05x10^{-9}
-15	3.67x10^{-3}		9.29x10^{-4}		5.74x10^{-9}
-20	4.05x10^{-3}		1.13x10^{-3}		4.26x10^{-9}
-25	4.89x10^{-3}		1.58x10^{-3}		3.41x10^{-9}
-30	3.78x10^{-3}		1.88x10^{-3}		1.86x10^{-9}
-35	4.54x10^{-3}		3.87x10^{-3}		1.92x10^{-9}
-40	7.91x10^{-3}		1.05x10^{-2}		2.47x10^{-9}
-45	1.03x10^{-2}		1.85x10^{-2}		2.36x10^{-9}
-50	2.05x10^{-2}		4.13x10^{-2}		2.86x10^{-9}
-55	2.74x10^{-2}		9.71x10^{-2}		2.77x10^{-9}
-60	3.92x10^{-2}		1.75x10^{-1}		3.68x10^{-9}
61-65	2.75x10^{-2}		1.23x10^{-1}		2.59x10^{-9}
66	4.58x10^{-1}		4.75x10^{0}		4.31x10^{-8}
67-70		1.52x10^{-3}		2.56x10^{-4}	1.77x10^{-9}
-74		1.07x10^{-3}		1.96x10^{-4}	1.03x10^{-9}
-78		2.79x10^{-3}		5.35x10^{-4}	2.24x10^{-9}
-82		3.10x10^{-2}		6.19x10^{-3}	1.84x10^{-8}
83-87		3.30x10^{-1}		5.68x10^{-2}	6.06x10^{-8}

a: Detector size = 150x833x400 cm^3

uncollided source would be properly tracked in space and time. In addition, Pb has been used directly around the detector system.

The time dependence of the neutron flux at the front of the detector is given in fig.11 for a delta function source of neutrons for several neutron energies and an 8 m Fe shield. These data can be convoluted with the pulse structure of the proton beam to obtain the time structure of the neutron and gamma ray flux at the entrance of the detector. The data in fig.11 can be approximately converted to current by multipling the highest energy neutron flux by 1,and the lower energy fluxes by ~0.25 (see Table 5, last column).

The fast flux is directed more radially into the detector system while the lower energy fluxes are more isotropic.

Convoluting the neutron flux in the 160 - 180 MeV range with a rectangular proton pulse of 100/sec and 200 nsec in width gives raise to the data presented in fig.12. Since the neutron flux structure for this energy range of neutrons given in the previous figure raises and falls within a 200 nsec interval, the convoluted neutron flux will saturate to a steady state value during the time the proton pulse is on. However, if the neutron flux time structure is much wider than 200 nsec, the convoluted flux will not saturate and in the case of the lower energy neutrons will form an almost continuous background of radiation. This type of background can be greatly reduced depending on the time gate the detector is allowed to have.

The pulse structure of the gamma rays will be determined by the neutrons which are producing them. Gamma rays which result from fast neutron inelastic collisions will follow the pulse structure of the fast neutrons. Gamma rays which result from low energy neutrons namely capture will be more of a constant background as is the case for the lower energy neutrons and can be time gated to reduce their effect.

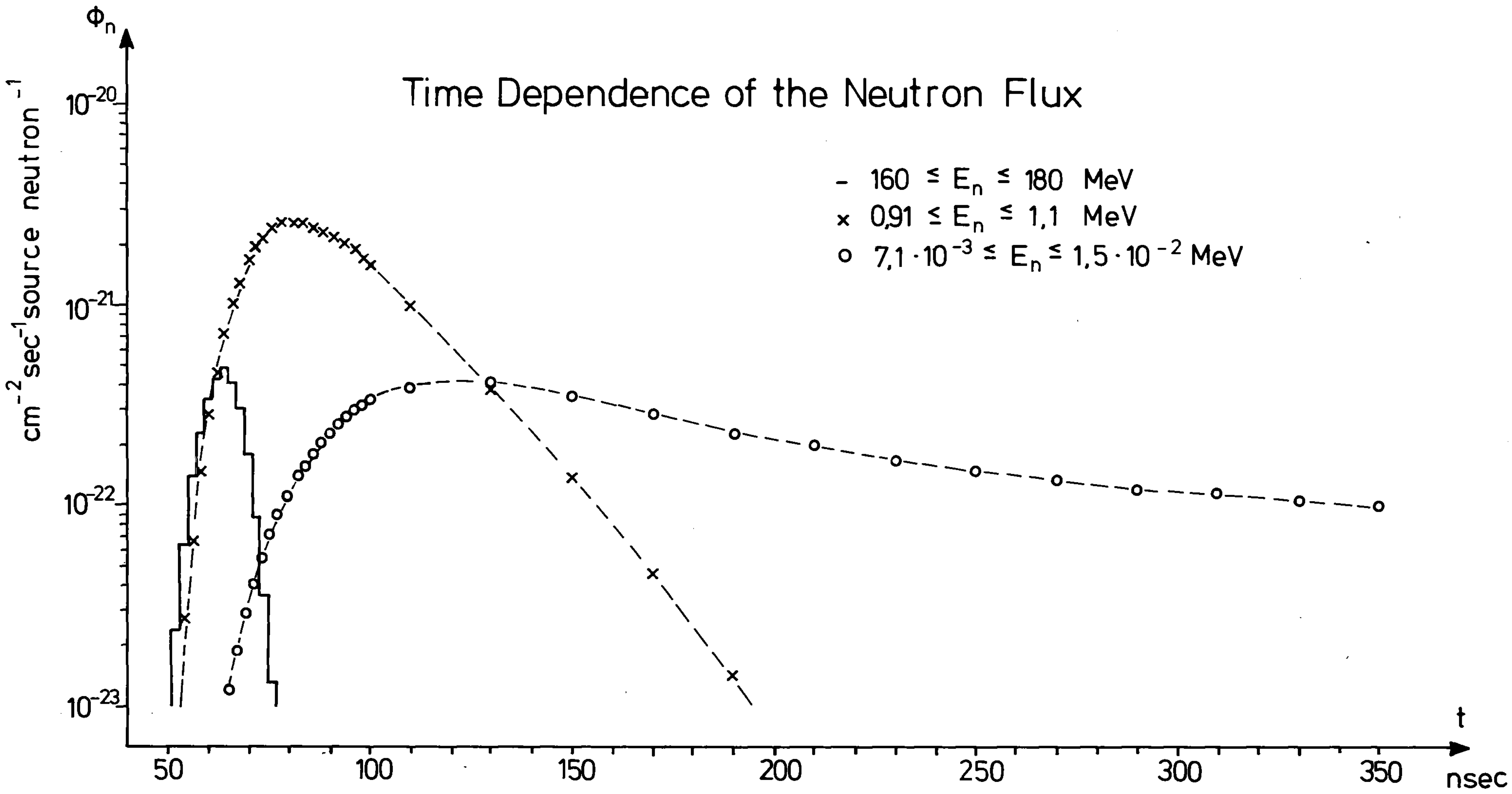

Fig.11: Time dependence of the neutron flux at the front of the detector from a delta function neutron source.

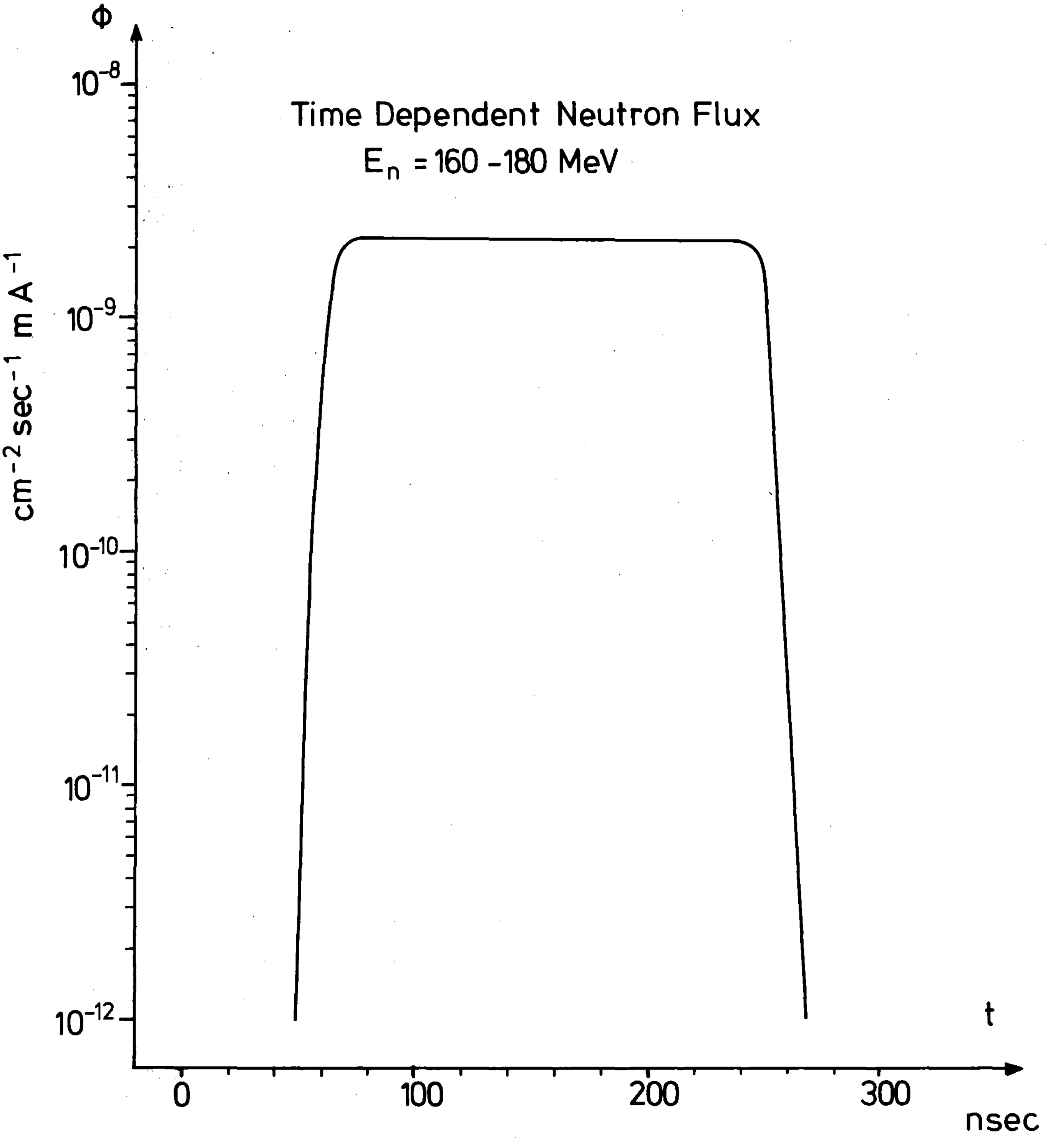

Fig.12: Time dependence of the neutron flux in the 160-180 MeV energy range at the front edge of the detector. Proton beam structure: 100 pulses/sec; 100 nsec pulse width; 1 mA average current

Given in fig.13 is the convoluted fast neutron flux ($E > 1$ MeV), the slow neutron flux (excluding the thermal flux), the thermal neutron flux and the gamma flux for the time structure of the proton beam defined before.

In an attempt to reduce the thermal neutron flux, boron was added to the heavy concrete. However, due to the large number of fast neutrons in the system, a factor of only two reduction in the thermal flux was obtained.

As a check of our one-dimensional analysis, a two dimensional DOT calculation was performed to obtain the neutron flux at the detector system. The results were consistent within factors of 2. Final shielding calculations will be carried out at a later date using two dimensional analysis. For these scoping studies, the one dimensional analysis appears very satisfactory.

Scattered Source Shield

Large numbers of fast and slow neutrons will enter the experimental area above the neutrino cave due to the diagnostic holes through the primary shield (see fig.6). These neutrons can then scatter through the concrete floors and enter the neutrino cave area. To estimate the shielding requirements for these neutrons, two ANISN calculations were performed. Since the neutrons streaming through the diagnostic holes must scatter before they reach the experimental area, an ANISN calculation was performed using the neutron source spectrum defined in fig.8. These neutrons were assumed to be normally incident on a slab of thick concrete. The neutrons which are emitted (albedo) from the surface will constitute the source neutron spectrum for the second ANISN calculation. The second ANISN calculations is a spherical calculation using the above neutron spectrum as an isotropic source. The calculational sequence and the geometry and materials are summarized in fig.14. The density of the materials is the same as given in Table 4.

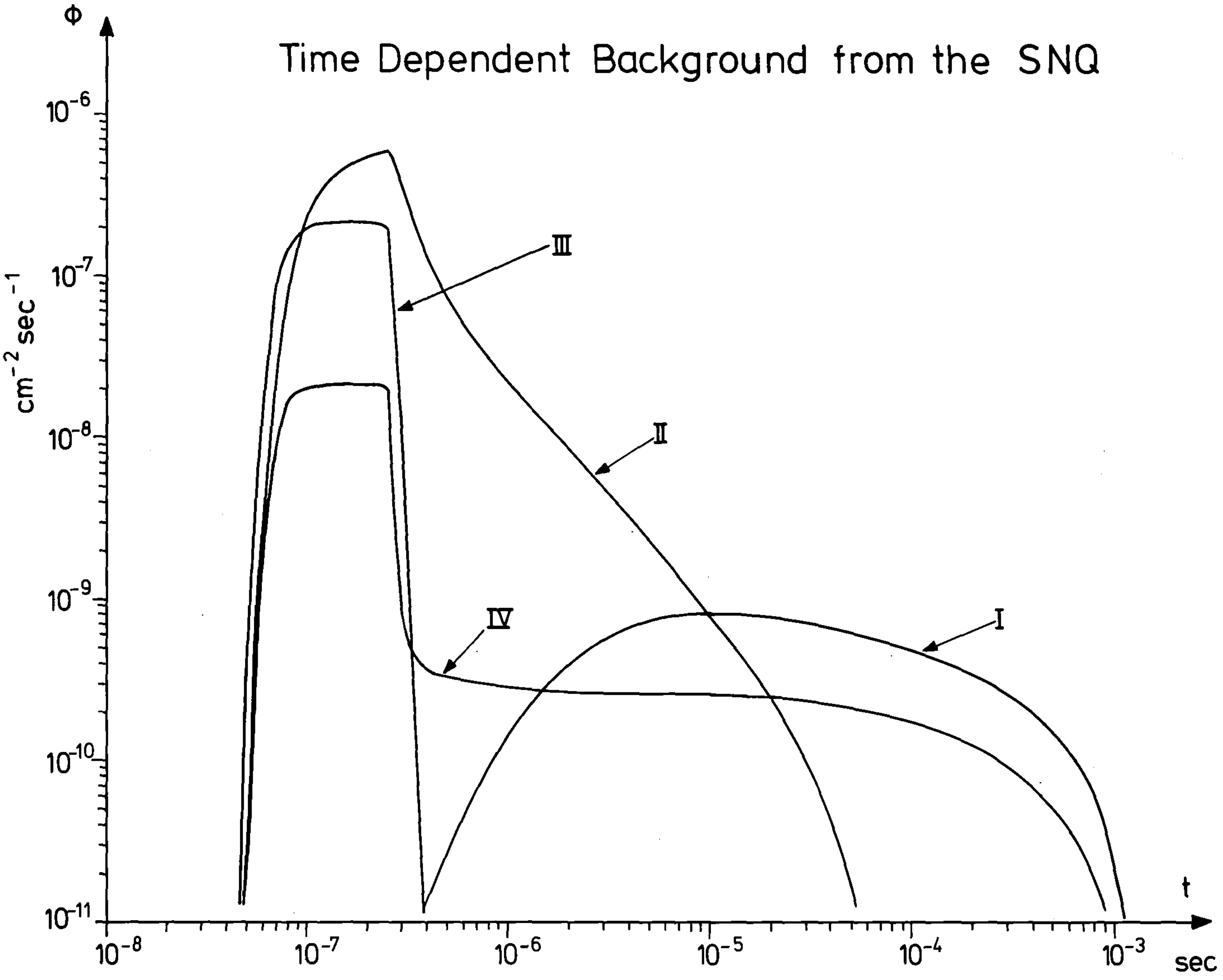

Fig. 13: Time dependence of the neutron and gamma ray flux at the front edge of the detector.

I : thermal neutrons

II : low energy neutrons; 0.4 eV < E_n < 1 MeV

III: fast neutrons; E_n > 1 MeV

IV : gamma rays

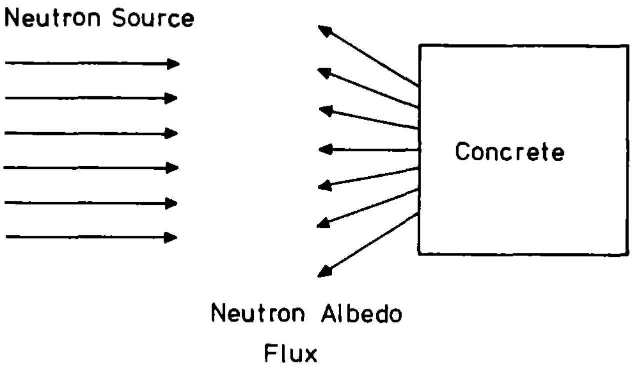

ANISN calculation number 1 to determine the albedo neutron source spectrum for the second ANISN calculation, slab geometry

---

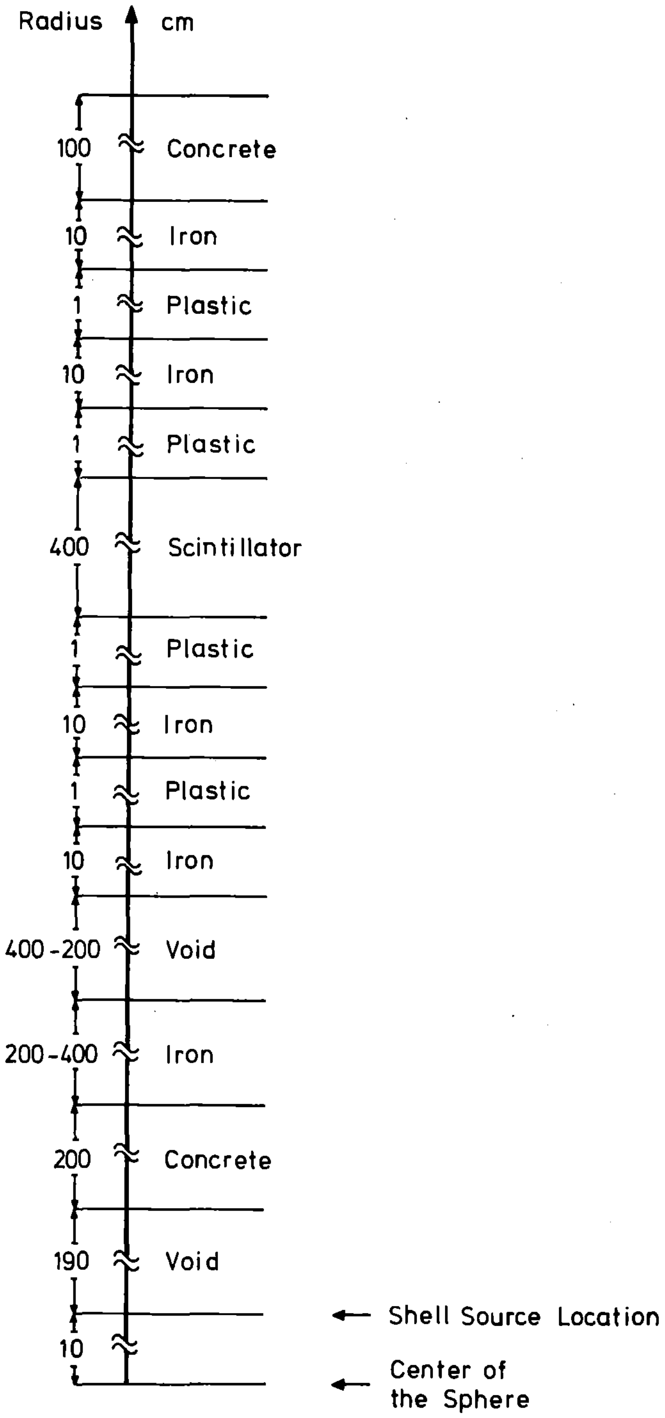

ANISN calculation number 2 to determine shielding requirements for scattered neutrons, spherical geometry

Fig.14: Geometry of the two ANISN calculations used for the scatterd source shielding calculations.

The neutron albedo spectrum calculated from the first ANISN calculation is given in fig.15 for neutrons with energies > 15 MeV. As before, only the higher energy neutrons will contribute to the background in the detector area. For every neutron with energy > 15 MeV incident on the slab of concrete, 1.58×10^{-2} neutrons with energy > 15 MeV are reflected or scattered backward. Using the albedo spectrum for the source in the second ANISN calculation and the following normalization, the particle currents incident on the detector are given in Table 7.

The normalization used for the scattered source is as follows:

$$\left|6.25\times10^{15}\ \frac{p/sec}{mA}\right| \times \left|1.267\ \frac{n}{p}\right| \times \left|\frac{\pi(5)^2\times10}{2\pi(50)^2+2\pi(50)(150)}\right|$$

number of diagnostic holes
times the ratio of the opening
to the ratio of the spallation
source

$$\times\left|1.58\times10^{-2}\right.$$ number of reflected neutrons/neutron incident|

$$\times\left|\frac{cm^{-2}}{4\pi(800)^2}\right.$$ approximate reduction of source due to R^2 attenvation|

$$\times\left|\pi(5)^2\times10\right.$$ total surface area of particles emerging|

$$= 1.53\times10^{8}\ n/sec/mA\ (E > 15\ MeV)$$

Until a better description of the exact experimental area can be defined, the above approximations will be sufficient.An attempt has been made to estimate this background conservatively high for the present. As before the surface area of the detector has been taken to be 150x833 cm^2.

For 3 m of iron shielding the prompt neutron and gamma ray event rates will be ~3/day.

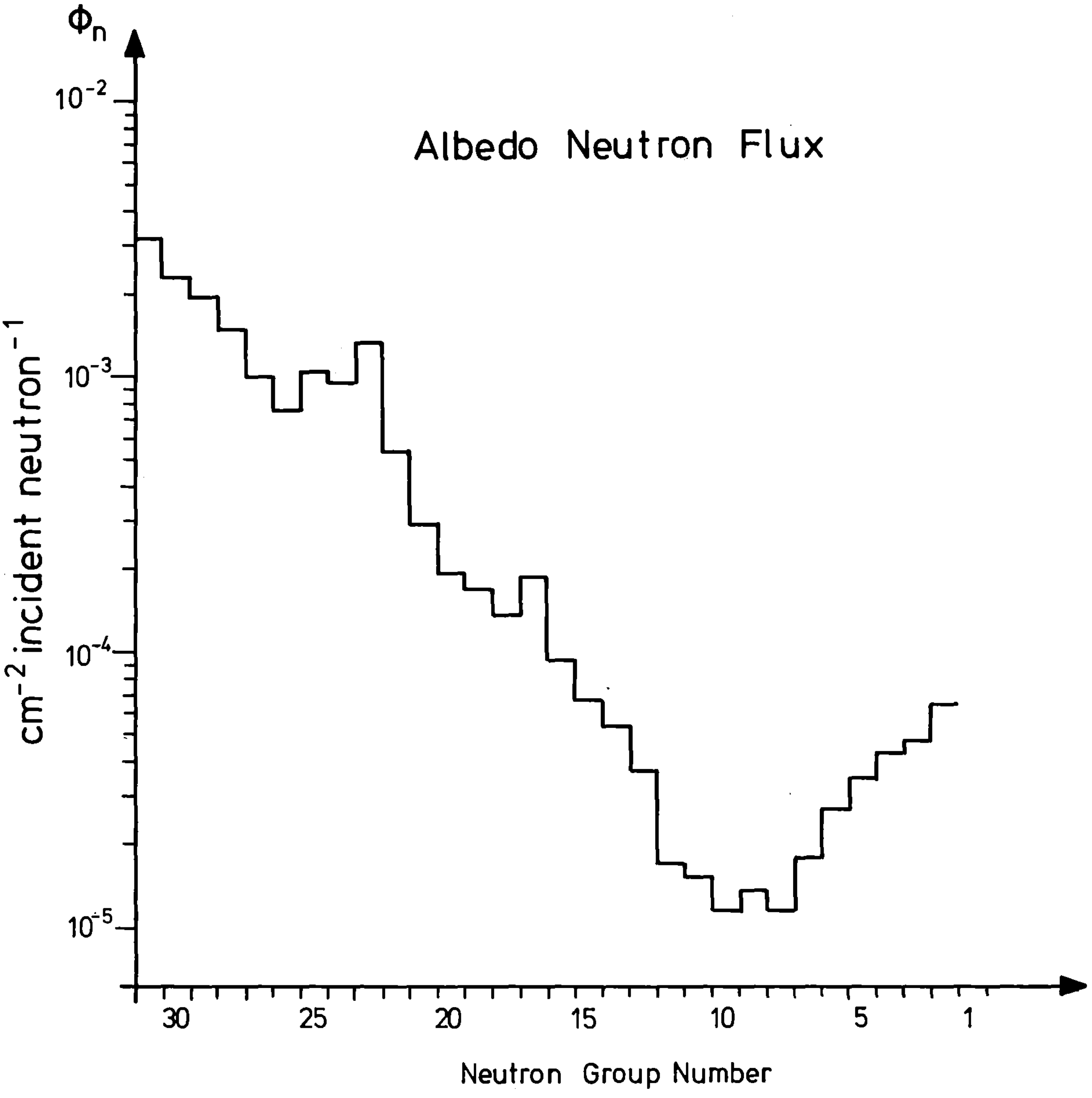

Fig.15: The calculated albedo source for the scattered neutron shielding problem

Table 7: Particles Entering the Detector System from Sacttered Sources as a Function of Energy and Iron Shield Thickness

Neutrons$\cdot$d$^{-1}\cdot$mA^{-1}

Grps	Shield Thickness		
	2m	3m	4m
1- 5	9.86×10^{0}	3.13×10^{-2}	7.02×10^{-5}
6-10	9.63×10^{1}	3.55×10^{-1}	1.11×10^{-3}
11-15	1.80×10^{2}	7.45×10^{-1}	2.56×10^{-3}
16-20	1.36×10^{2}	5.58×10^{-1}	1.91×10^{-3}
21-25	1.09×10^{2}	4.43×10^{-1}	1.50×10^{-3}
26-30	7.08×10^{1}	2.88×10^{-1}	9.71×10^{-4}
31-35	6.66×10^{1}	2.69×10^{-1}	9.07×10^{-4}
36-40	1.19×10^{2}	4.79×10^{-1}	1.62×10^{-3}
41-45	3.09×10^{2}	1.24×10^{0}	4.20×10^{-3}
46-50	2.06×10^{3}	8.37×10^{0}	2.81×10^{-2}
51-55	2.08×10^{3}	8.47×10^{0}	2.84×10^{-2}
56-60	2.40×10^{3}	9.88×10^{0}	3.36×10^{-2}
61-65	1.33×10^{3}	5.47×10^{0}	1.89×10^{-2}
66	4.72×10^{3}	1.93×10^{1}	6.59×10^{-2}

Gammas$\cdot$d$^{-1}\cdot$mA^{-1}

67-70	6.11×10^{2}	2.51×10^{0}	8.67×10^{-3}
71-74	3.09×10^{2}	1.27×10^{0}	4.39×10^{-3}
75-78	3.02×10^{2}	1.24×10^{0}	4.31×10^{-3}
79-82	8.05×10^{2}	3.30×10^{0}	1.14×10^{-2}
83-87	3.18×10^{3}	1.30×10^{1}	4.48×10^{-2}

2. Galactic Shielding

Shielding from Galactic Neutrons and Protons

From previous neutrino experiments, the event rate background from galactic neutrons and protons have been controlled by a reasonable amount of shielding (~1 to 2 m of Fe) and by a favourable time structure of the incident beam. To reconfirm that shielding of these particles is possible very approximate calculations have been carried out. The neutron flux spectrum calculated at sea level by Armstrong et al.[20)] has been used as a source for a 1-D slab ANISN calculation. As before neutrons above 400 MeV in energy have been included by conserving total energy and placing these particles in the 375 - 400 MeV energy group. The source is assumed to be isotropically incident on a thick slab (2 m) of heavy concrete followed by varying thickness of Fe shielding. The detector system follows the shielding. To approximately account for the protons the results of the neutron calculations have been multiplied by 2. The results of the calculation are presented in Table 8. As can be seen 1 to 2 m of Fe reduces the current of incident particles substantially.The background from these particles can be time gated easily.

Shielding from Galactic Muons

Of all of the background radiations, the muons are the most difficult to shield against. Instead of the shielding increasing approximately logmetrically as was the case for the direct and scattered neutrons from the spallation source and for galactic neutrons and protons, the shielding requirement for the muons will vary almost linearly; that is, to reduce the muon background by 2 requires almost twice the shielding. There are several ways muons can contribute to the background. These include 1) muons which pass through or stop in the detector, 2) bremsstrahlung from the electron from muon decay in the Fe (or Pb) around

Table 8: Particles Entering the Detector System from Galactic Neutron and Proton Sources as a Function of Energy and Iron Shield Thickness

Neutrons·d^{-1}

Grps	Shield Thickness 1m	2m	3m
1 - 5	6.50x10^{1}	1.90x10^{-1}	5.13x10^{-4}
6 -10	2.29x10^{2}	9.72x10^{-1}	3.62x10^{-3}
11-15	3.57x10^{2}	1.68x10^{0}	6.86x10^{-3}
16-20	2.58x10^{2}	1.22x10^{0}	4.93x10^{-3}
21-25	2.11x10^{2}	9.83x10^{-1}	3.93x10^{-3}
26-30	1.40x10^{2}	6.46x10^{-1}	2.58x10^{-3}
31-35	1.39x10^{2}	6.32x10^{-1}	2.49x10^{-3}
36-40	2.63x10^{2}	1.18x10^{0}	4.64x10^{-3}
41-45	6.68x10^{2}	3.01x10^{0}	1.18x10^{-2}
46-50	3.63x10^{3}	1.75x10^{1}	6.98x10^{-2}
51-55	3.51x10^{3}	1.72x10^{1}	7.02x10^{-2}
56-60	3.95x10^{3}	1.96x10^{1}	8.08x10^{-2}
61-65	2.16x10^{3}	1.08x10^{1}	4.48x10^{-2}
66	7.82x10^{3}	3.88x10^{1}	1.59x10^{-1}

Gammas·d^{-1}

67-70	9.89x10^{2}	4.94x10^{0}	2.04x10^{-2}
71-74	4.97x10^{2}	2.50x10^{0}	1.03x10^{-2}
75-78	4.89x10^{2}	2.46x10^{0}	1.61x10^{-2}
79-82	1.31x10^{3}	6.54x10^{0}	2.69x10^{-2}
83-87	5.38x10^{3}	2.66x10^{1}	1.09x10^{-1}

the detector, 3) bremsstrahlung (WAB) from muons in the Fe (or Pb) around the detector and 4) bremsstrahlung from muons (WAB) and produced electrons from muon decay in the iron shield above the detector system. The bremsstrahlung (WAB, so called wide angle bremsstrahlung) associated with the muons is not the same flavour as that associated with electron bremsstrahlung. This type of bremsstrahlung for the muons is strongly depressed due to the mass dependence ($\sim m_e^2/m_\mu^2$).

In obtaining the results presented in this section, the muon spectrum defined in ref.21) has been used. This data (integrated over momentum and over 1 steradian) is presented in fig.16 indicating the number of muons with momentum greater than a given momentum. Since the spectral shape of the muon spectrum remains approximately constant when passing through shielding material, the shape of the curve in fig.16 will remain constant and only the magnitude will change. To insure that these results will yield an upper estimate the muons are assumed to be normally incident on the shielding material which is taken to be 2 m of heavy concrete followed by 3 m of iron and finally 20 cm of iron directly around the active part of the detector system. In addition, the minimum ionization energy for iron and concrete has been used to obtain the number of muons reaching the detector. A safety factor of 3 is then applied to all obtained counting rates.

Several EGS calculations were performed to obtain the pulse height distributions for the bremsstrahlung from electrons in the Fe around the detector and the WAB of the μ in the Fe around the detector and from the roof. Approximate WAB cross sections were obtained from ref.22).

The results of these calculations are given in fig.17. For the energy range of interest, namely 10 - 20 MeV, approximately 3×10^6 events/day can be expected. With an anti-coincidence suppression of 10^5 and the proposed duty factor

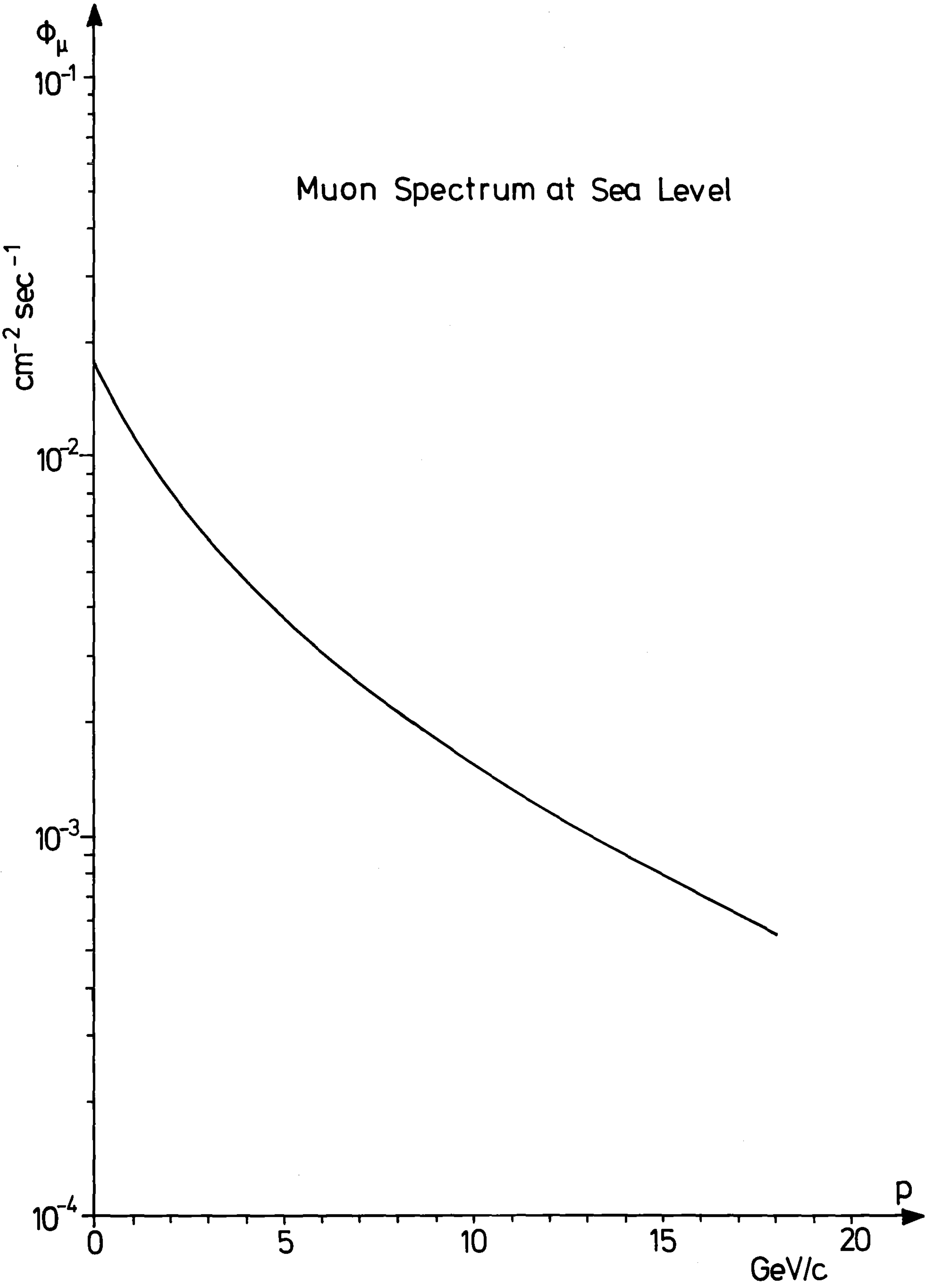

Fig.16: Number of muons at sealevel greater than a given momentum

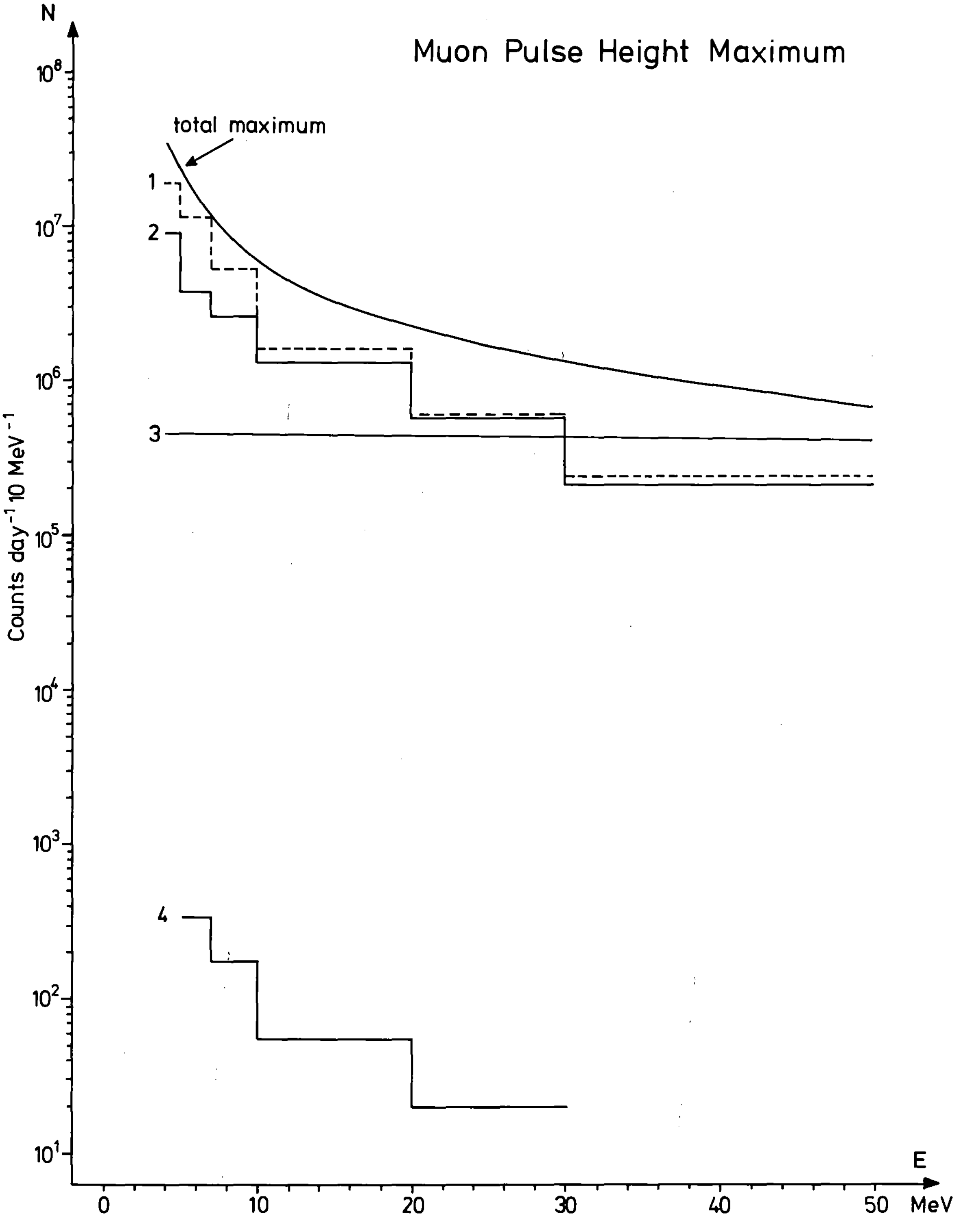

Fig.17: Pulse height maximum in detector for 3 m Fe, 2 m concrete and 20 cm Fe shield around detector (no anti-rejection), for 9 m Fe, 1 m concrete and 20 cm Fe shield, multiply values by 0.35

1. Bremsstrahlung from μ in Fe around detector; 2. Bremsstrahlung from e from μ decay in Fe around detector; 3. Muons which stop in detector; 4.Bremsstrahlung from μ and e in roof

of 5×10^{-2}, the event rate/day can be reduced to ~ 1. Since an attempt has been made to obtain a maximum event rate, the true event rate should be on the order of 0.2/day with three meter of iron shielding.

Muons which decay in the detector after slowing to rest are not included in fig.17. Depending on the time gate, a muon decay in the detector can yield a bogus event. However, a dead time gate of ~ 30 - 35 μsec after an anti fire can reduce this background to $\lesssim$ 1/day.

The effectiveness of the anti-counters with respect to the electrons produced in the Fe surrounding the detector is given in fig.18. As can be seen, the anti counter reduces this background by only a factor of 2. However, in neutrino physics every factor of 2 is graciously accepted.

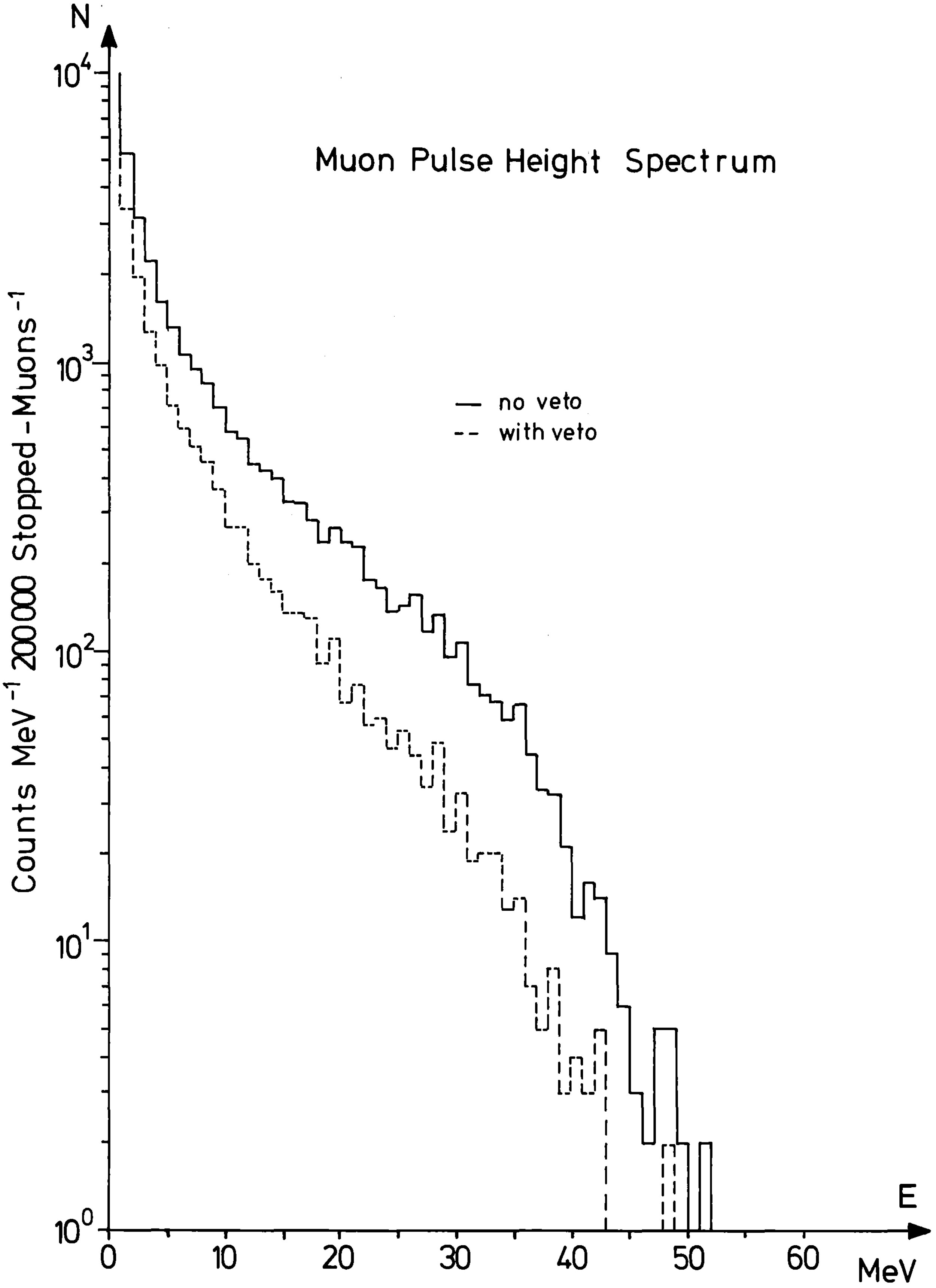

Fig.18: Pulse height distribution in detector system from μ decay in Fe surrounding detector with and without veto system.

3. Natural Radioactivity and Neutrinos from Decay of produced radioactive Nuclides

Previous neutrino experiments have detected background signals in their detectors from natural radioactivity. The Los Alamos detector of Willis indicated that this background could be as high as several events/day but that most of the produced signals were very low ($\lesssim$ 10 MeV) in energy. It is imperative that the shielding closest to the detector system, and the support material for the detector be as clean of natural radioactivity as possible. Iron which has been used around accelerator facilities should not be considered for use.

The decay of produced radioactive nuclides around the spallation source yield large numbers of low energy neutrinos. If one assumes that every star produced by an incident 1.1 GeV proton will produce a neutrino, then ~50 neutrinos will be emitted per proton. This is quite a large number of neutrino from radioactive nuclides when compared to 0.133 from π^+ decay. However, even if all of these decay nuclide neutrinos could produce an event in the energy range of interest they will represent a continuous background due to there finite lifetimes and can be time gated. Any reasonable time gate will reduce this background to an acceptable level.

C) Detector Analysis

The expected energy resolution and efficiency of a detector system, i.e., its ability to yield the energy of a gamma ray, electron or any other particle, is determined by many factors including sampling fluctuations, energy loss due to leakage, scintillation light or charge collection efficiency, saturation effects, electronic noise, etc.. All of these factors will effect the performance of the two types of detector systems considered in this work: a modular scintillation system and a liquid argon ionization chamber. This is especially true since the energy range of the particles (γ,$e^{\pm}$) produced by neutrino interactions of interest are from 5 to ~30 MeV.

Sampling fluctuations are present whenever the energy deposition through ionization is not measured throughout the detector volume but only in specific areas. For modular or segmented systems, the energy deposited in the material seperating the "active" sections is not measured and will induce sampling fluctuations.For the scintillation detector systems considered here, the sampling fluctuations contribute only slightly to the resolution. However, for the liquid argon system the sampling fluctuations will be one of the major contributors to the overall resolution since the target material for the incident neutrons, carbon (which is part of the scintillator system), must be introduced between the ionization sections. Since the electron gamma shower code, EGS, is a multimedia, three-dimensional program, the sampling flucuations are included explicity, i.e., energy deposited in non-active areas is not converted to scintillation light or electrical charge.

Neglecting a slight $1/R^2$ effect, the incident neutrinos will interact uniformily throughout the volume of the detector system with a large percentage of the interactions being located close to the edge of the detector. Since scintillator and liquid argon (and carbon) have rather large radiation lengths,a substantial amount of particle leakage from this system is expected and thereby a worsing of the resolution and efficiency. However, it will be shown that the largest effect is with the efficiency and not with the resolution. As with the sampling fluctuations,the EGS code includes the effect of energy leaking from the system.

The collection efficiency of scintillation light following the deposition of energy by a charged particle will be determined by the geometry of the modular section, the reflectivity of the surface, the absorption length of scintillation light in the scintillation material, and the photo-electron conversion efficiency. The MORSE Monte Carlo code was modified to determine the light collection and conversion to photo-electron efficiency of the scintillation detector systems considered here. These results were combined with the energy depositions calculated by EGS code to yield realistic responses. Neglecting leakage energy, the collection and conversion of the scintillation light will have the largest effect on the performance of the scintillation detector system.

Charge collection in the liquid argon ionization chamber will also effect the performance of this system. However, because of the sampling fluctuations and leakage, the fluctuation in charge collection will be a second order effect and, therefore, will not be considered.

For electron-gamma showers, saturation types effects, i.e., the scintillation light observable or charge collected is not a linear relationship with respect to energy deposition, are expected to be small and need not to be considered.

Electronic noise and other effects which can have an impact on the performance of our detector systems will not be treated. These problems are usually second order effects and can be made almost neglible by utilizing state-of-the-art electronic and by providing adequate shielding.

Scintillation Detector System

As mentioned above the MORSE Monte Carlo code with spectular reflection at specified boundaries and operated in an analog mode was modified to transport scintillation light throughout a module of the detector system.

Several module sizes were considered: a 10x10x100 cm^3 module with 5.08 cm diameter phototubes, one attached to each end, and a 20x20x150 cm^3 module with 10.16 cm diameter phototubes, one attached to each end.

The wavelength distribution of the scintillation light and the phototube detection efficiency are shown in fig.19 a and b. The wavelength distribution was used by employing standard sampling techniques to define the source for the transport calculation. As implied by the histogram in fig.19a, the calculation was carried out using 15 scintillation light wavelength groups, each group being 10 nm wide.

The absorption length for all wavelengths of light considered was assumed to be constant at 150 cm for the 10x10x100 cm^3 module and 250 cm for the 20x20x150 cm^3 module. Scintillation light which reached the sampled flight path before reaching the phototube was assumed to be absorbed (or killed) and, therefore, did not contribute to the signal. The reflectivity of the walls of the module was taken to 97% (or on the average 3 photons in a 100 were absorbed (or killed) on the walls). Spectular reflection at the walls of the module was used to define the reflected photon direction. Photons which reach the phototube produced a photo-electron with the probability given in fig.19b. No statistical weighting was used in any of these calculations. A source particle which started with statistical weight of one had a statistical weight of one when or if it made it to the phototube.

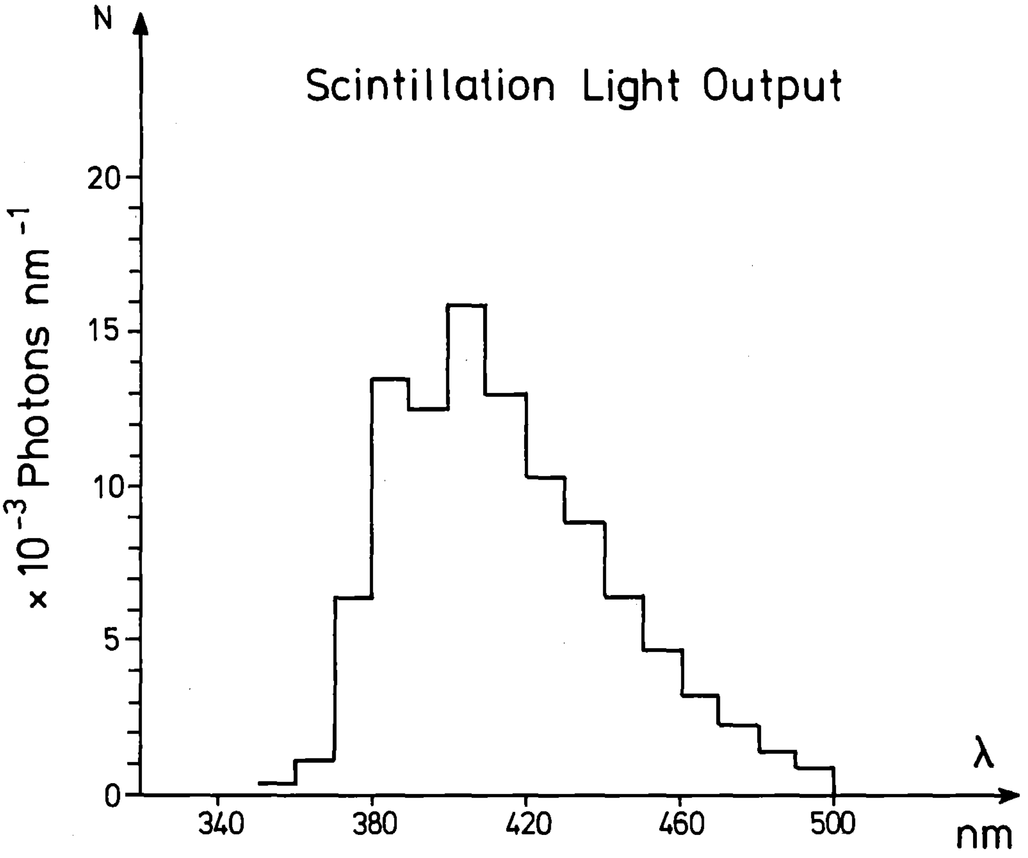

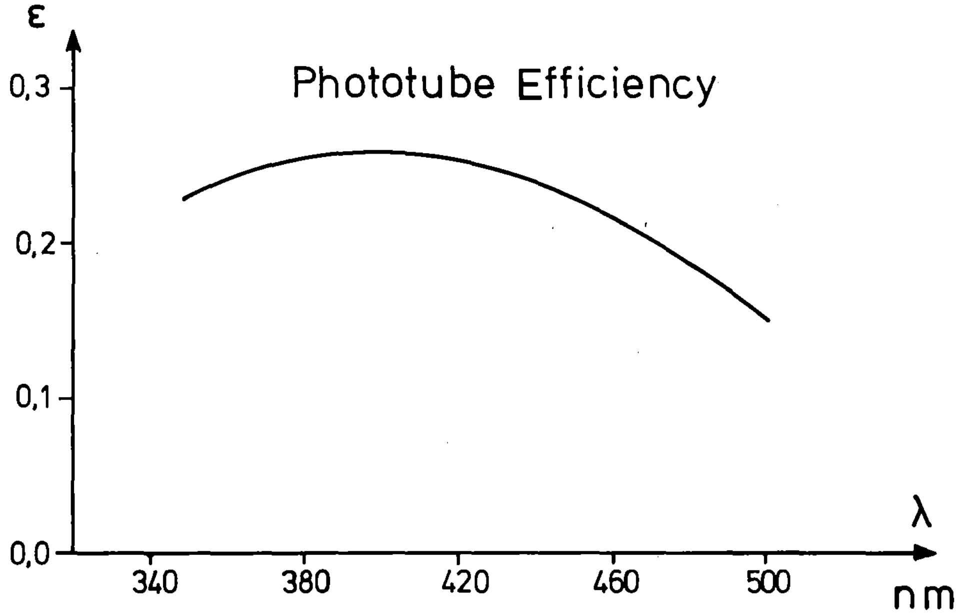

Fig.19: Scintillation light output and phototube efficiency versus wave lenght

Results for the 10x10x100 cm^3 Module Detector

The number of photo-electrons produced in both phototubes as a function of the number of scintillation photons is given in fig.20. These results are for an isotropic source of scintillation photons located in the center of the 10x10x100 cm^3 module. For 750 photons each phototube sees on the average 8.25 photo-electrons or 16.5 total. A fit to this data yields $y = 0.02203\ x$ where x is the number of scintillation photons and y is the total number of photo-electrons produced. The fluctuation in the total number of photo-electrons detected by both tubes is given in fig.21 as a function of the number of scintillation photons. These results are for the same type of source as defined.
For 750 photons the fluctuation(σ) in the average number of photo-electrons is $\pm$ 3.9. As one would expect from statistical theory the curves in fig.21 is proportional to the square root of the number of photons. A best fit to the data yields the following expression: $\sigma = 0.14258\ x$ where x is the number of scintillation photons and σ is the standard deviation of the average number of photo-electrons produced.

The pulse height data from which the fluctuations in fig.21 were obtained are very gaussian for reasonably large number of photo-electrons (> 10). A comparison between a gaussian curve and the data is given in fig.22.

So far the data presented has been for an isotropic source located in the center of the module. The variation of the average number of photo-electrons detected when 500 scintillations photons are emitted as a function of distance from the closest photo-tube is given in fig.23. The curve is reasonable flat until about 5 cm from the edge. This strong dependence on the last 5 cm will probably eliminate this area from consideration since a small pulse here will lead to overly large signal. A least squares fit to the data in fig.23 gives the following expression:

$$Y = 3.29 \coth (0.10\ x) - 0.05\ x + 10.00$$

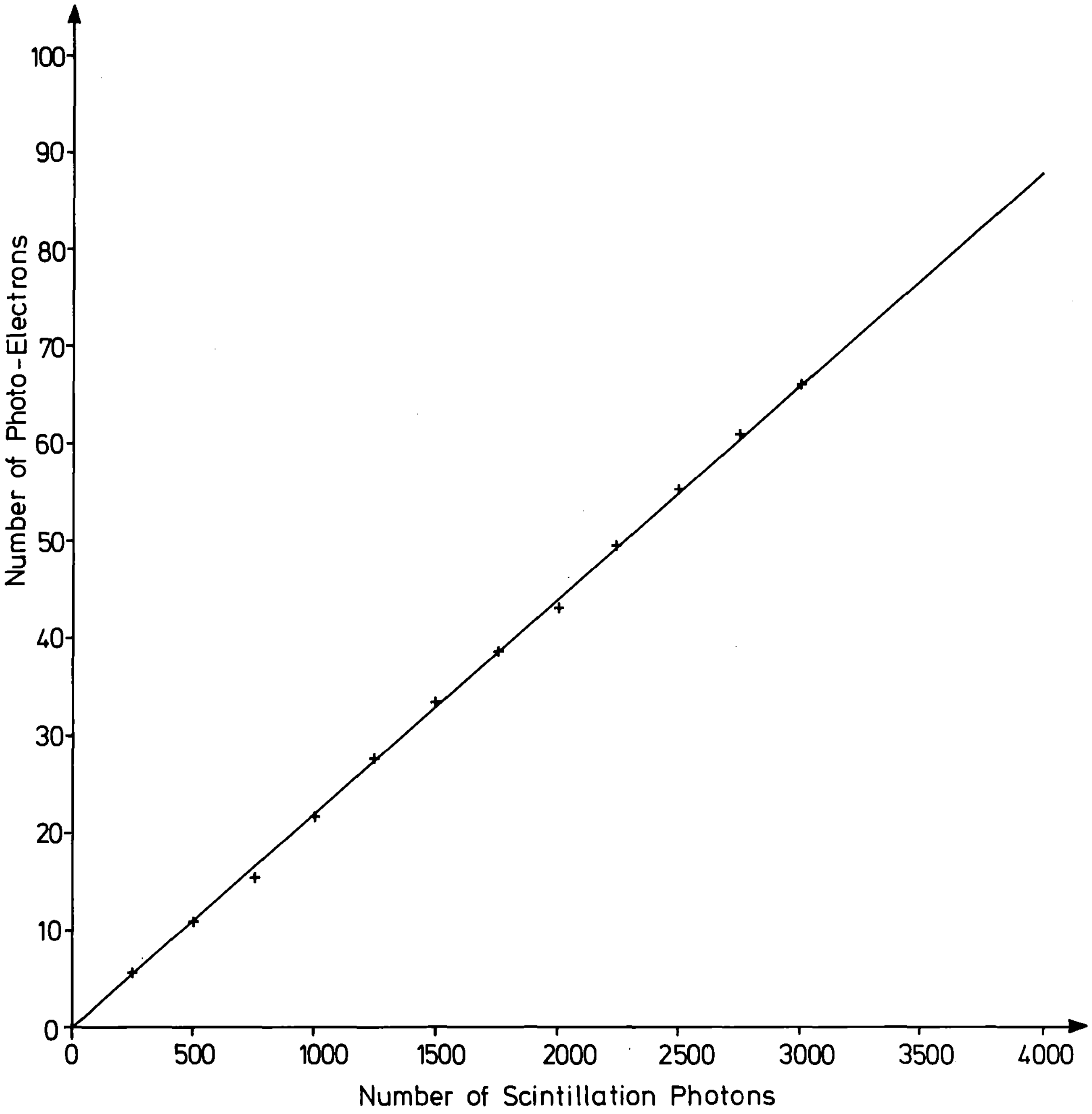

Fig.20: The number of photo-electrons produced versus the number of scintillation photons for the 10x10x100 cm^3 module. Source photon location is in the center of the module. The number of electrons represents the sum from both photomultiplier tubes.

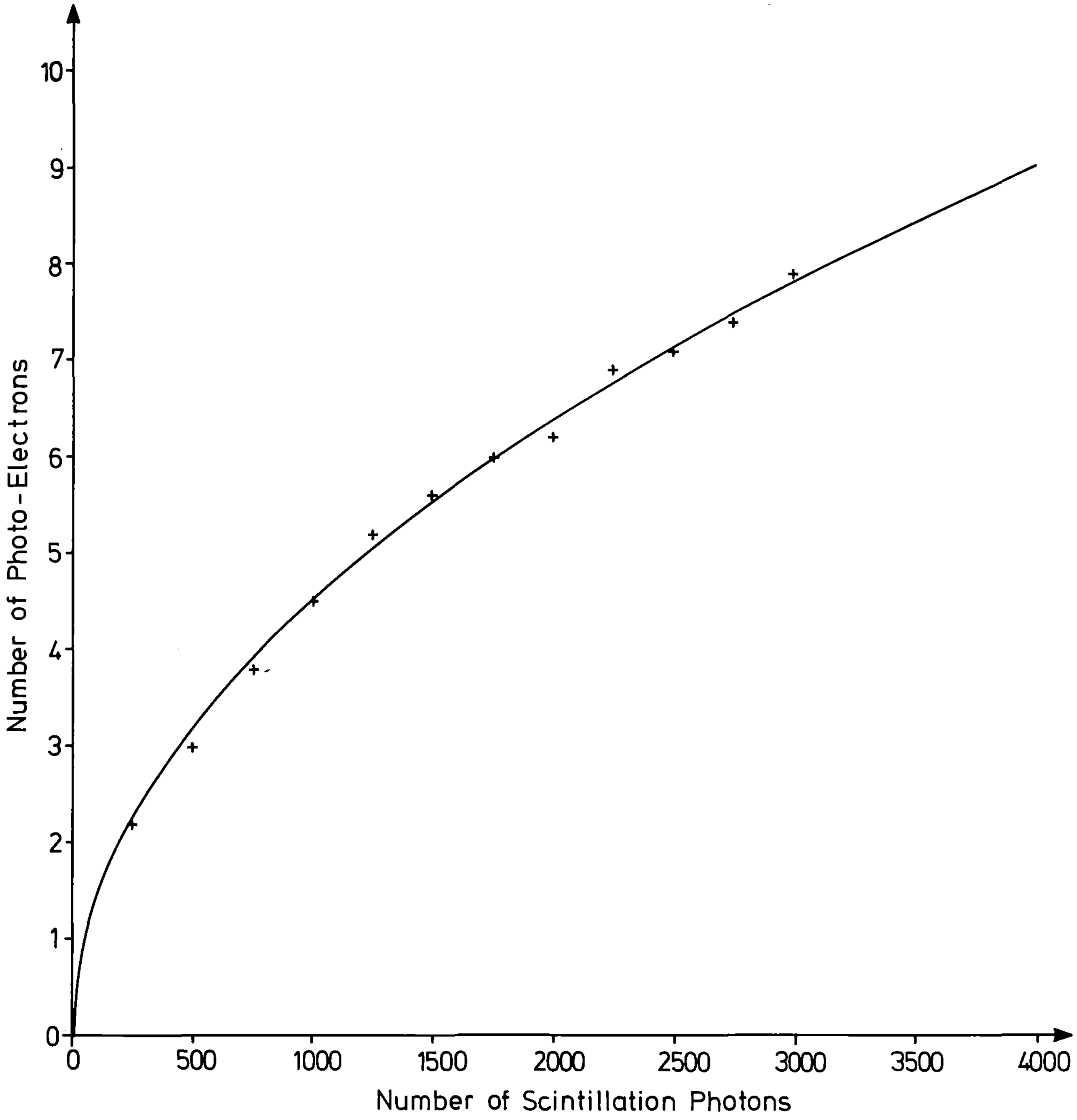

Fig.21: Standard deviation in the number of photo-electrons produced versus the number of scintillation photons for the 10x10x100 cm^3 module. Source photon location is in the center of the module. The number of electrons represents the sum from both photomultiplier tubes.

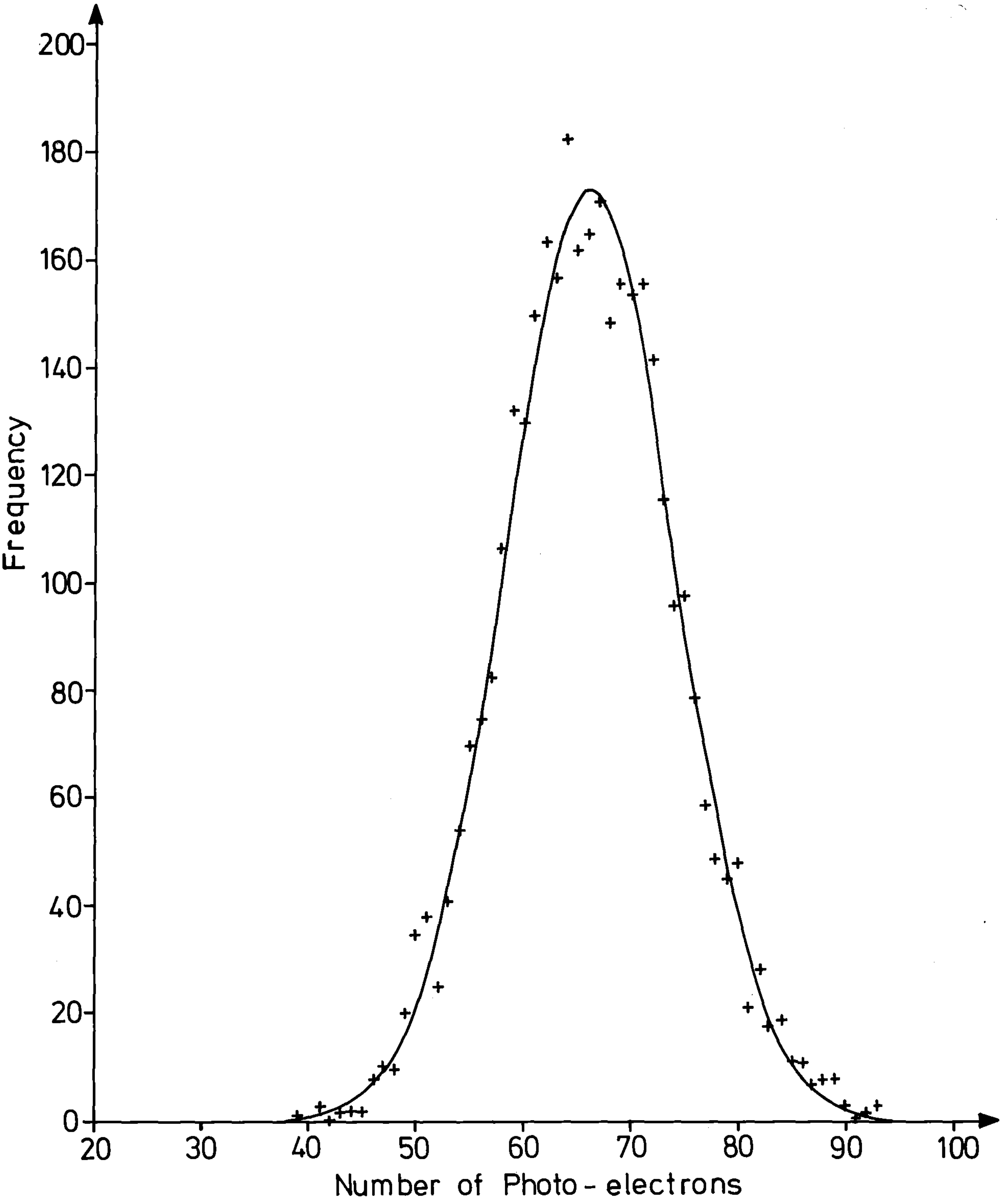

Fig.22: Comparison between calculated data (+) and gaussian fit to that data.

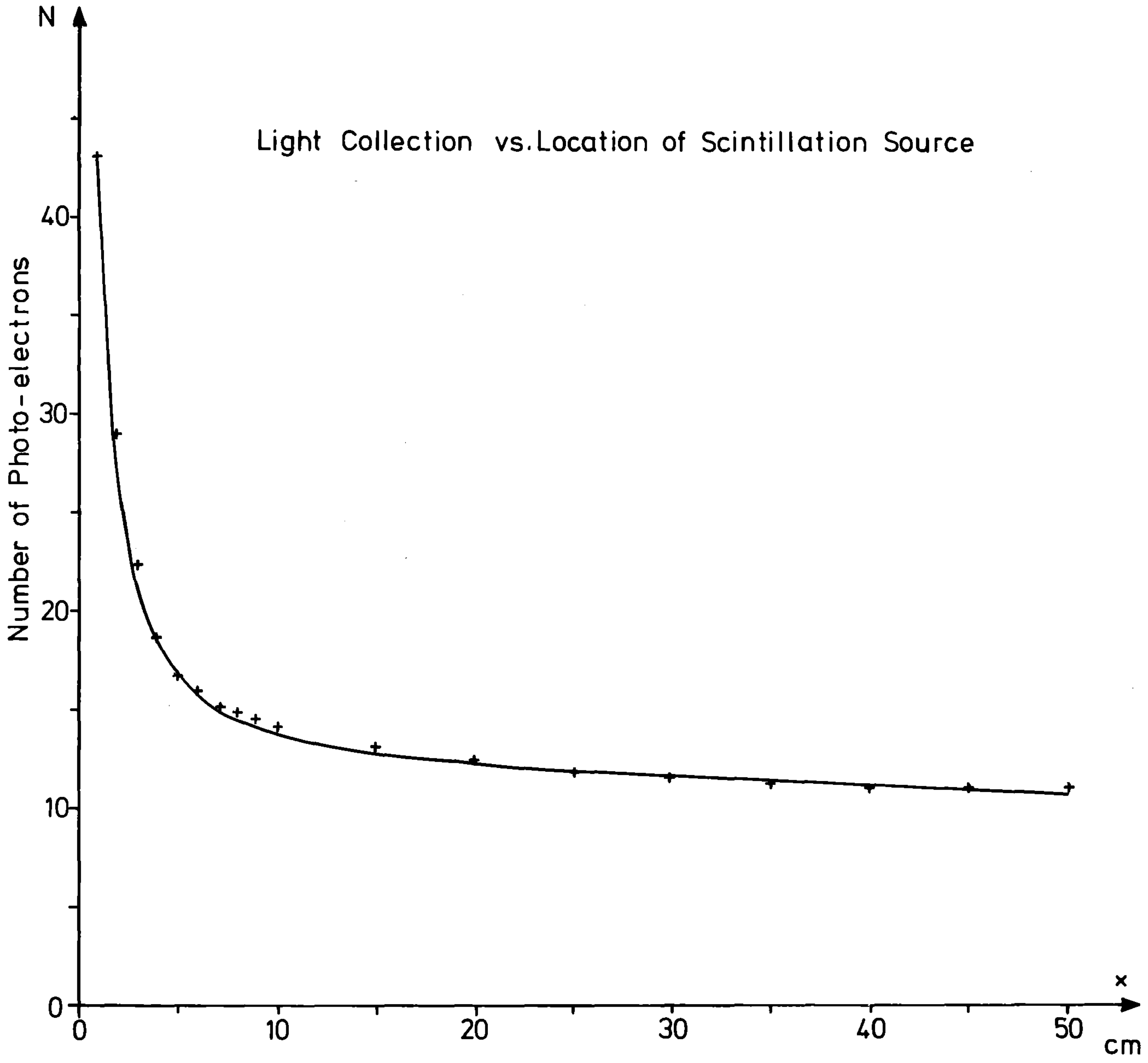

Fig.23: Spatial variation in the number of photo-electrons as a function of distance from the closest photomultiplier tube for a source of 500 scintillation photons. The number of electrons represents the sum from both photomultiplier tubes (10x10x100 cm^3 module)

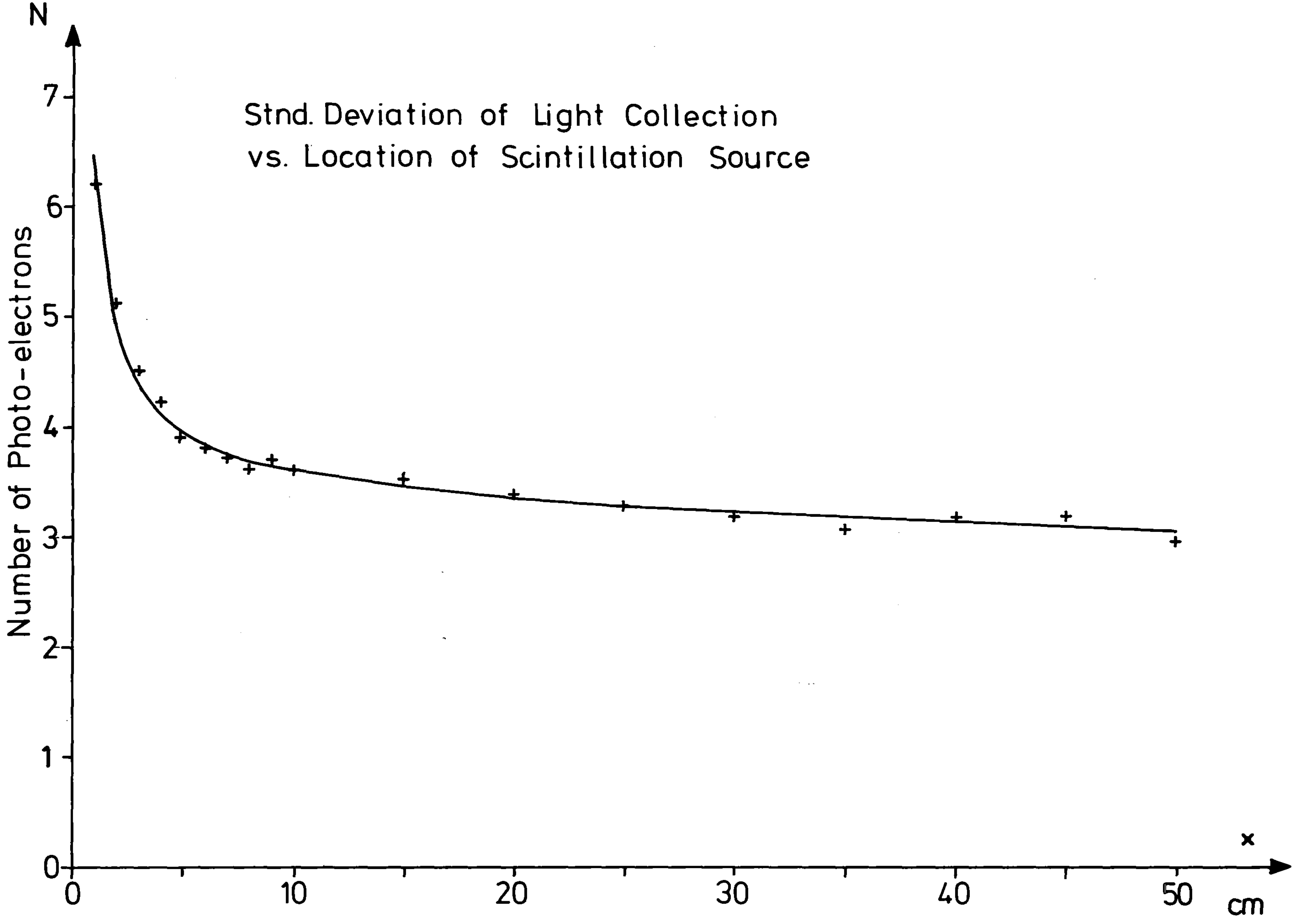

Fig.24: Spatial variation in the standard deviation in the number of photo-electrons produced versus the distance from the closest photomultiplier tube for a source of 500 scintillation photons. The number of electrons represents the sum from both photomultiplier tubes (10x10x100 cm^3 module)

where x is distance from the closest photomultiplier tube and Y is the number of photo-electrons.

There are other methods for producing a flatter response across the module and these methods will be discussed later.

The variation of the number of photo-electrons as a function of distance from the closest photomultiplier tube for 500 scintillation gammas is given in fig.24. A fit to this data yields the following expression

$$\sigma = 0.35 \coth(0.11\ x) - 0.01\ x + 3.28$$

where x ist the distance from the closest photomultiplier tube and σ is the standard deviation in units of number of photo-electrons.

Since the expected dependence on the number of photo-electrons is linear with respect to the number of scintillation gammas (see fig.20) and the fluctuations are proportional to the square root of the number of scintillation gammas (see fig.21), the data in fig.23 and fig.24 completely define the scintillation light collection efficiency of the 10x10x100 cm^3 module.

In all of the calculations presented so far, the source location for the scintillation gamma rays has been assumed to be on a line located in the center of the module. Variations in the average number of photo-electrons or their fluctuations due to source locations off this line are small except for source locations near the ends of the modules. These effects have not be included in the calculated results.

To convert from energy deposition to scintillation photons it has been assumed that 1 photon will be emitted per 100 eV of energy deposition. The EGS code provides the energy deposition and location and the curves in figures 23 and 24 along with a linear and square root dependence provide the detection efficiency (and fluctuations) of the observed light.

Two methods exist for obtaining the final detector response for one incident particle. The straight forward method stipulates that at each energy deposition site:

1. Convert energy deposition to scintillation gamma rays
2. find average number of photo-electrons, χ_i
3. sample from gaussian with proper σ_i to obtain fluctuation $\chi_i^{11} = \chi_i \pm \chi_i^1$ (if $\chi_i^{11} < 0$ set $\chi_i^{11} = 0$)
4. repeat above procedure for all energy deposition sites and sum the χ_i^{11}'s $\bar{\chi} = \Sigma\chi_i^{11}$

For each incident particle one number will be obtained which can be stored to form the pulse height distribution.

The other method will yield simular results but a much smoother pulse height distribution. The method is as follows:

1. Convert energy deposition to scintillation gamma rays
2. find average number of photo-electrons, χ_i and corresponding σ_i
3. sum the χ_i's to find $\bar{\chi} = \Sigma\chi_i$
4. sum the squares of the σ_i's to find $\bar{\sigma}^2 = \Sigma\sigma_i^2$
5. store $\bar{\chi}$ and $\bar{\sigma}$ so that the total pulse height for many incident particles can be convoluted from the $\bar{\chi}$'s and $\bar{\sigma}$'s

Method two will be used for most of these calculations.

The pulse height distribution for 15 MeV gammas which originate isotropically and uniformily (excluding the metal containers for the scintillator) throughout a 4.6 ton detector composed of 400 10x10x100 cm^3 modules (20 high by 20 deep by 1 wide) is given in fig.25. The thickness of the walls which optically separate the modules is 0.01 cm. Only the data in fig.20 has been used (with no fluctuations) to convert from energy deposition to photo-electrons. The

Fig. 25

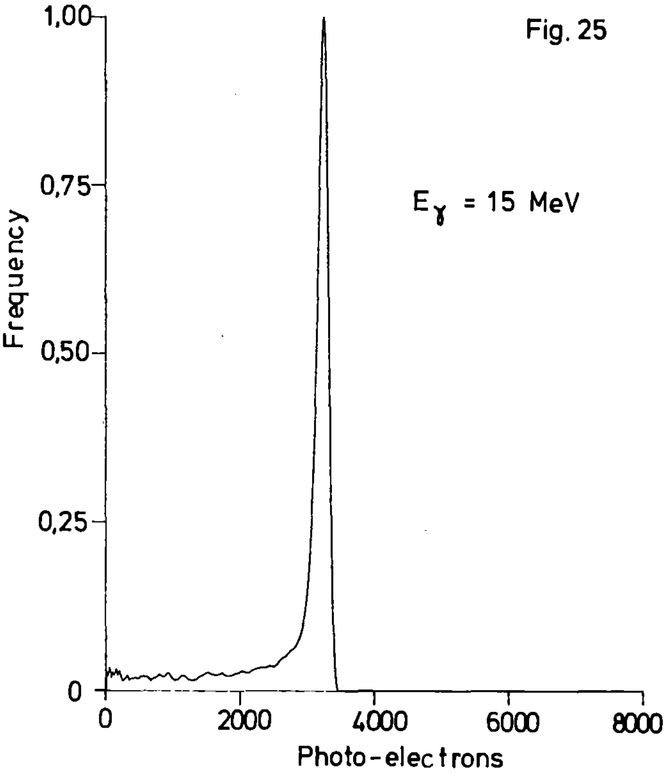

Fig.25: Pulse height distribution for 15 MeV gamma rays in the 10x10x100 cm^3 modular detector system neglecting spatial and fluctuational variations in the number of photo-electrons produced.

Fig. 26a

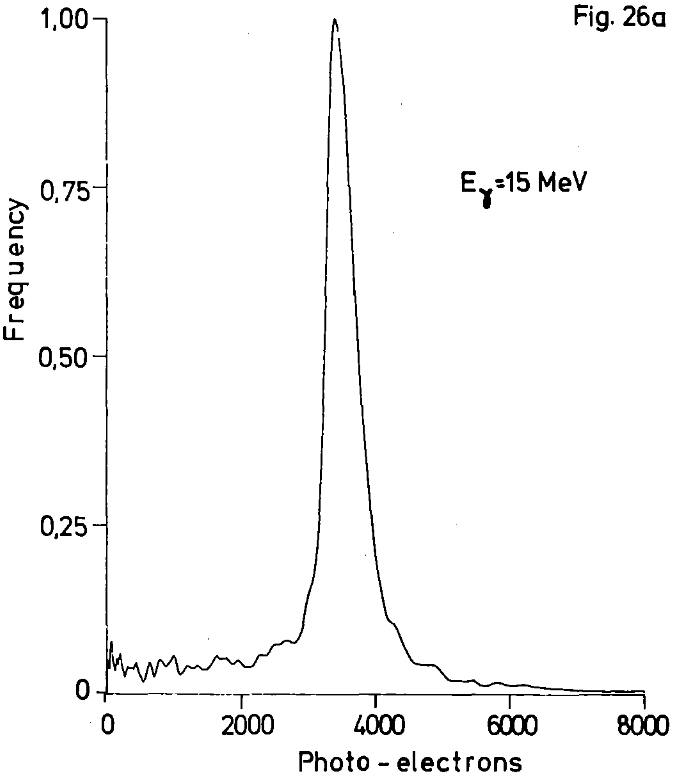

Fig. 26b

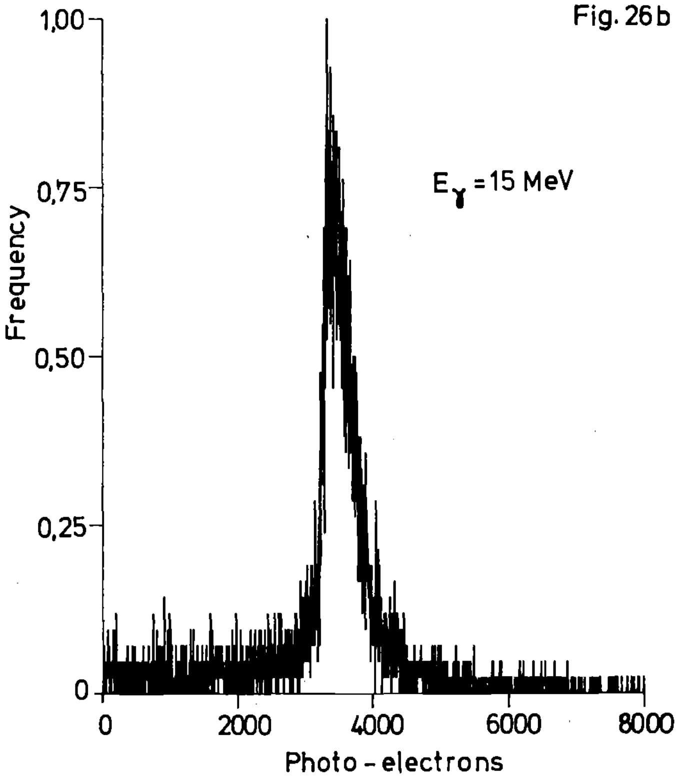

Fig.26a) Pulse height distribution for 15 MeV gamma rays in the 10x10x100 cm^3 modular detector system including all photo-electron production statistics and using method II.

b) Same as a) except method I is used to produce the pulse height distribution observed resolution, though physically unreal is excellent and is due entirely to energy leakage and sampling flucuations. The pulse height distribution obtained when the spatial dependence of the light collection and fluctuations are taken into account is given in fig.26a. The resolution worsens substantially and the pulse height distribution, in addition to having low energy pulse signals as before also has signals at much higher pulse heights due to the spatial dependence of the scintillation photons (see fig.23). The most probable peak has also moved to a higher value for the same reason. The pulse height distribution for 15 MeV gamma rays obtained using method 1 is given in fig.26b. As can be seen the results are similar. The expected pulse height distributions for other gamma energies and for various electron energies are given in figs. 27-29. Overall the resolution for this detector system is ~15% (FWHM) of which, sampling fluctuations and leakage energy contributes ~6%.

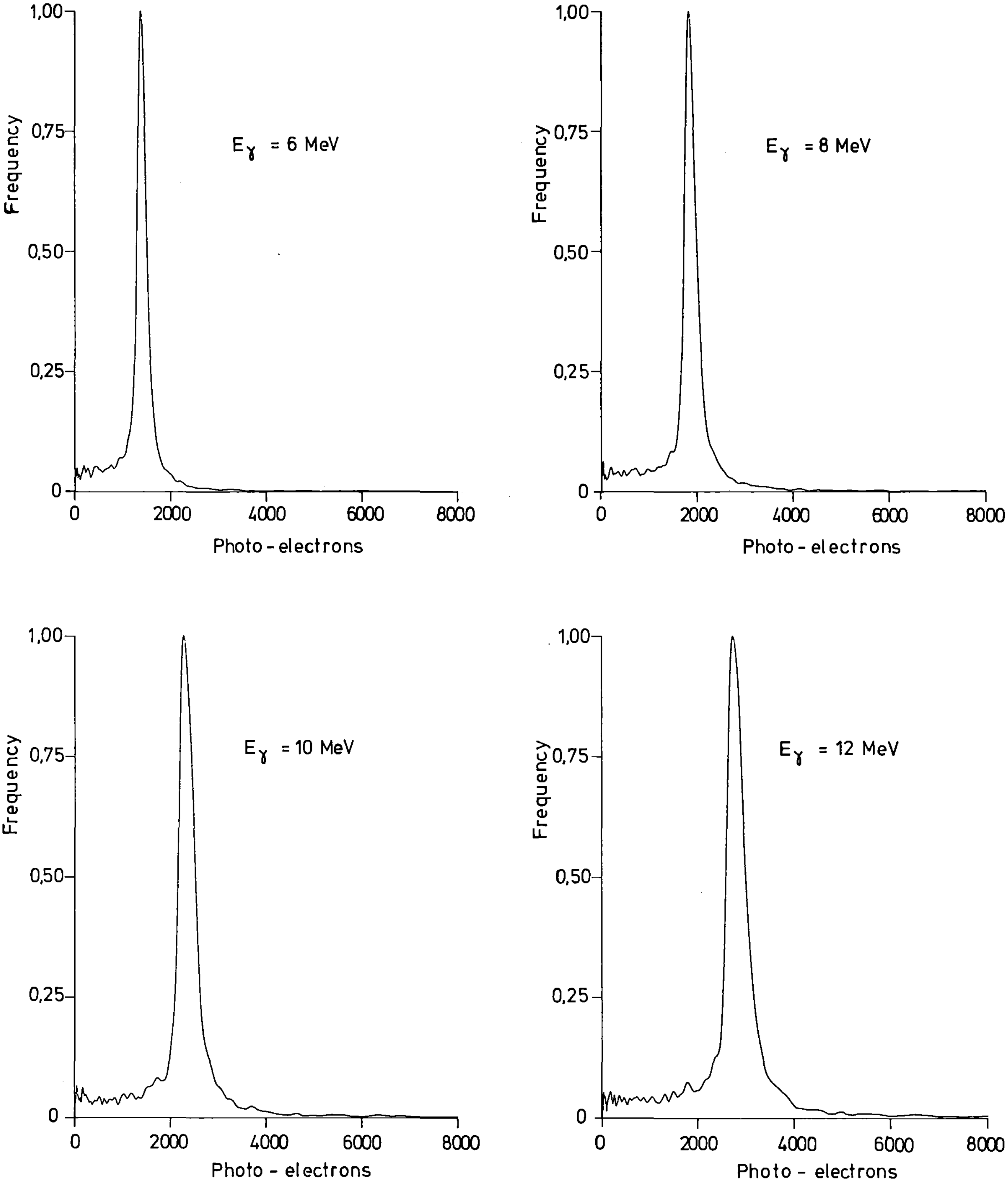

Fig.27: Pulse height distributions for various gamma ray energies (6, 8, 10 and 12 MeV) for the 10x10x100 cm^3 modular detector system.

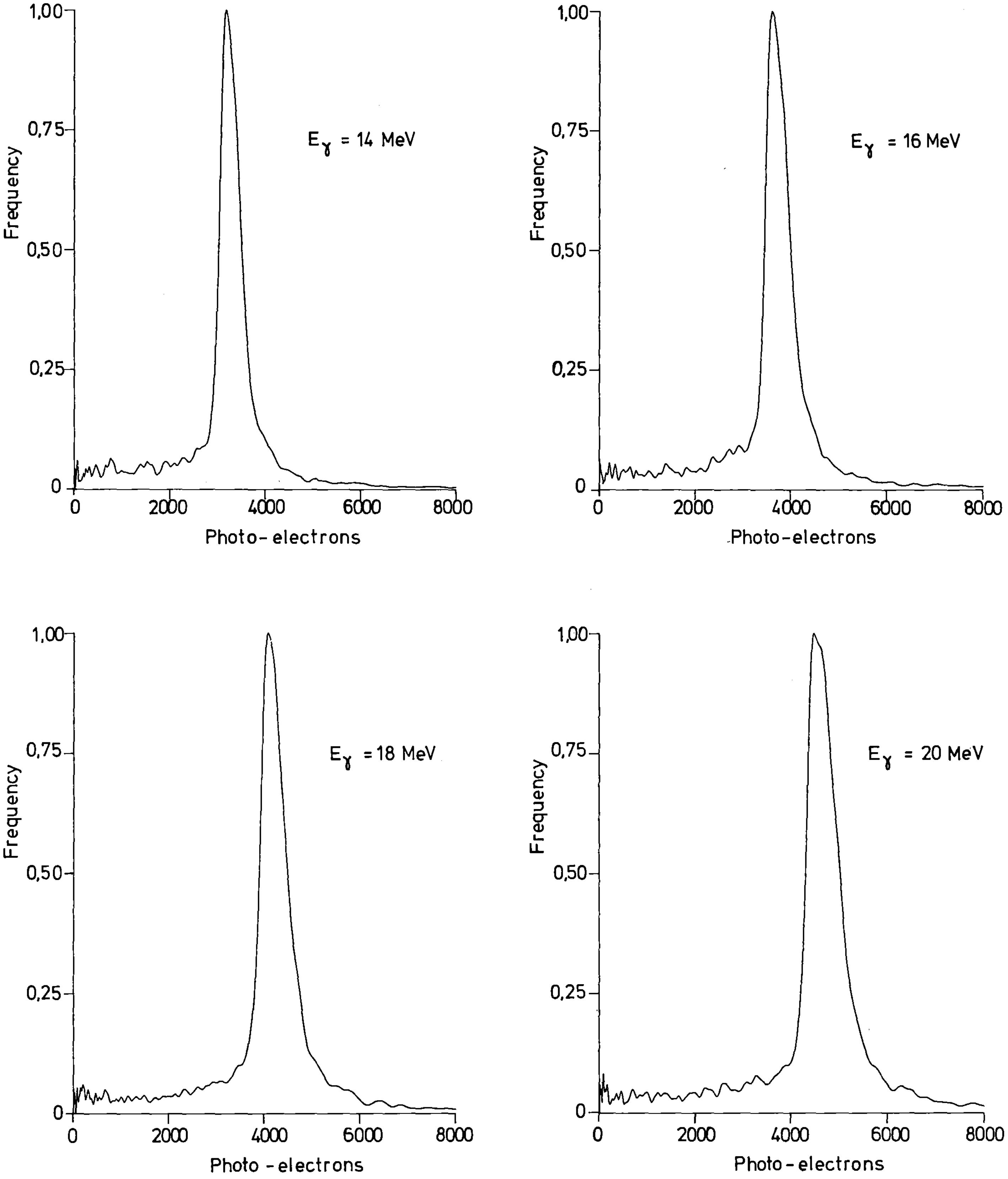

Fig.28: Pulse height distributions for various gamma ray energies (14, 16, 18 and 20 MeV) for the 10x10x100 cm^3 modular detector system.

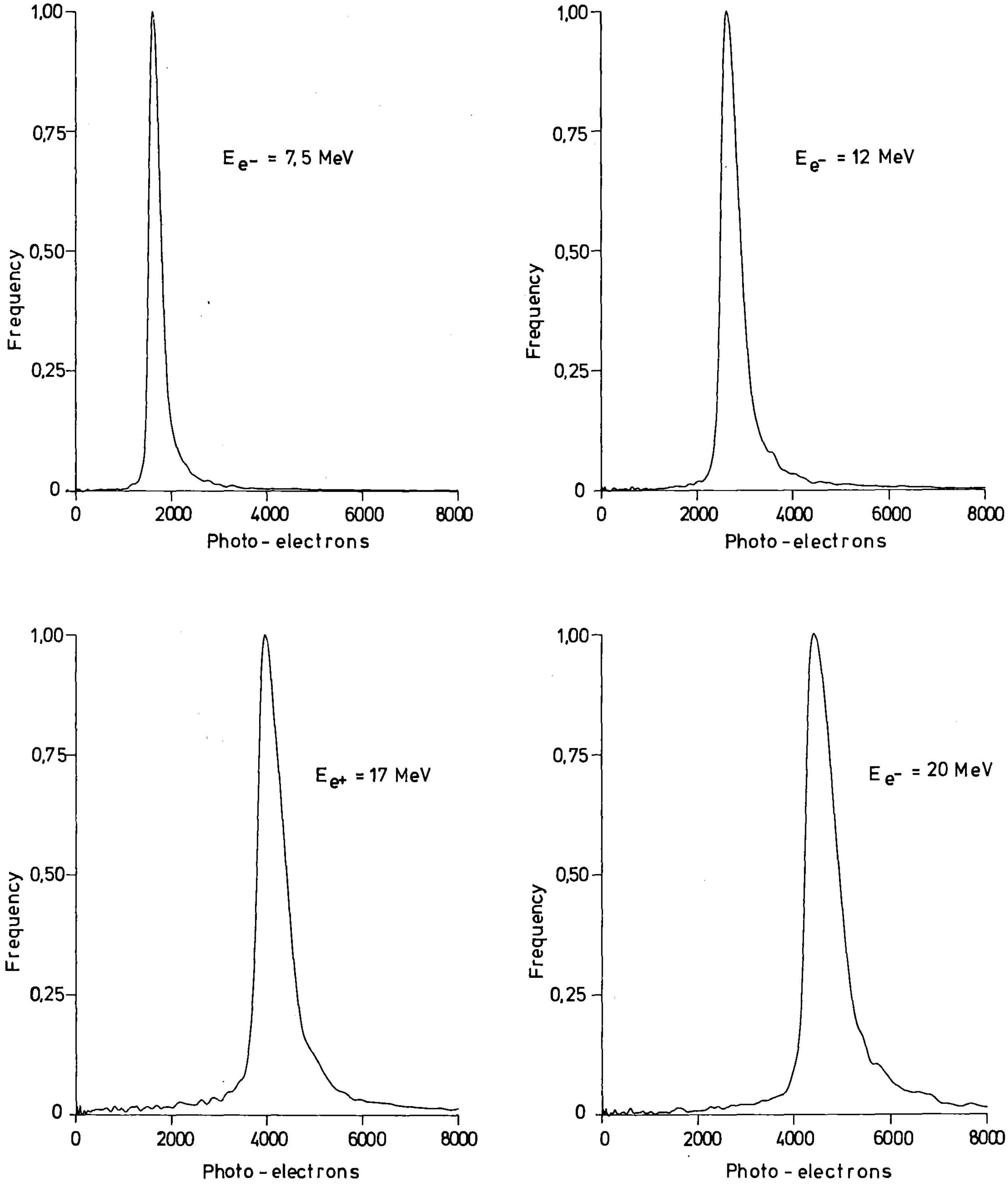

Fig.29: Pulse height distributions for various electron and positron energies for the 10x10x100 cm^3 modular detector system.

As mentioned earlier, there is another method which can be used to remove some of the spatial dependence on the number of photo-electrons detected (see fig.23). For the data presented so far, the number of photo-electrons produced in each of the two photomultiplier tubes have been summed to obtain the final total number. If the response is obtained by taking the square root of the product of the signal from each tube, instead of summing the signals, a much flatter spatial dependence can be obtained. The results of such a calculation are given in fig.30. The spatial dependence has been reduced substantially from that given in figs.23 and 24. The pulse height distributions for a 15 MeV gamma source as given before are presented in fig.33. Two things are quite apparent. The pulse height peak has moved to a lower position and the tail of the distribution has been drastically decreased. The resolution has also improved rather drastically leaving the sampling fluctuations and energy leakage as the dominate contributions to the energy resolution.

Results for the 20x20x150 cm^3 Modular Detector

The total size of this detector system is much larger than the previous one and has been taken to be the reference design detector for the neutrino experiment. The number of modules in this detector is 840 arranged 20 high by 42 deep by 1 wide. This represents the 50 ton detector. Photo-electron data for each module comparable to the data given in figs.23, 24 and 30 are presented in figs. 31 and 32.

The resulting pulse height distributions for 15 MeV gammas are given in fig.34a and b for the two methods used in obtaining the signals at the phototubes, i.e., the sum method and the product square root method. In case of the product square root method the resolution for the larger detector is only slightly better than for the previously considered system. But as expected in case of the sum method the energy resolution for the larger detector is much better than for the smaller one.

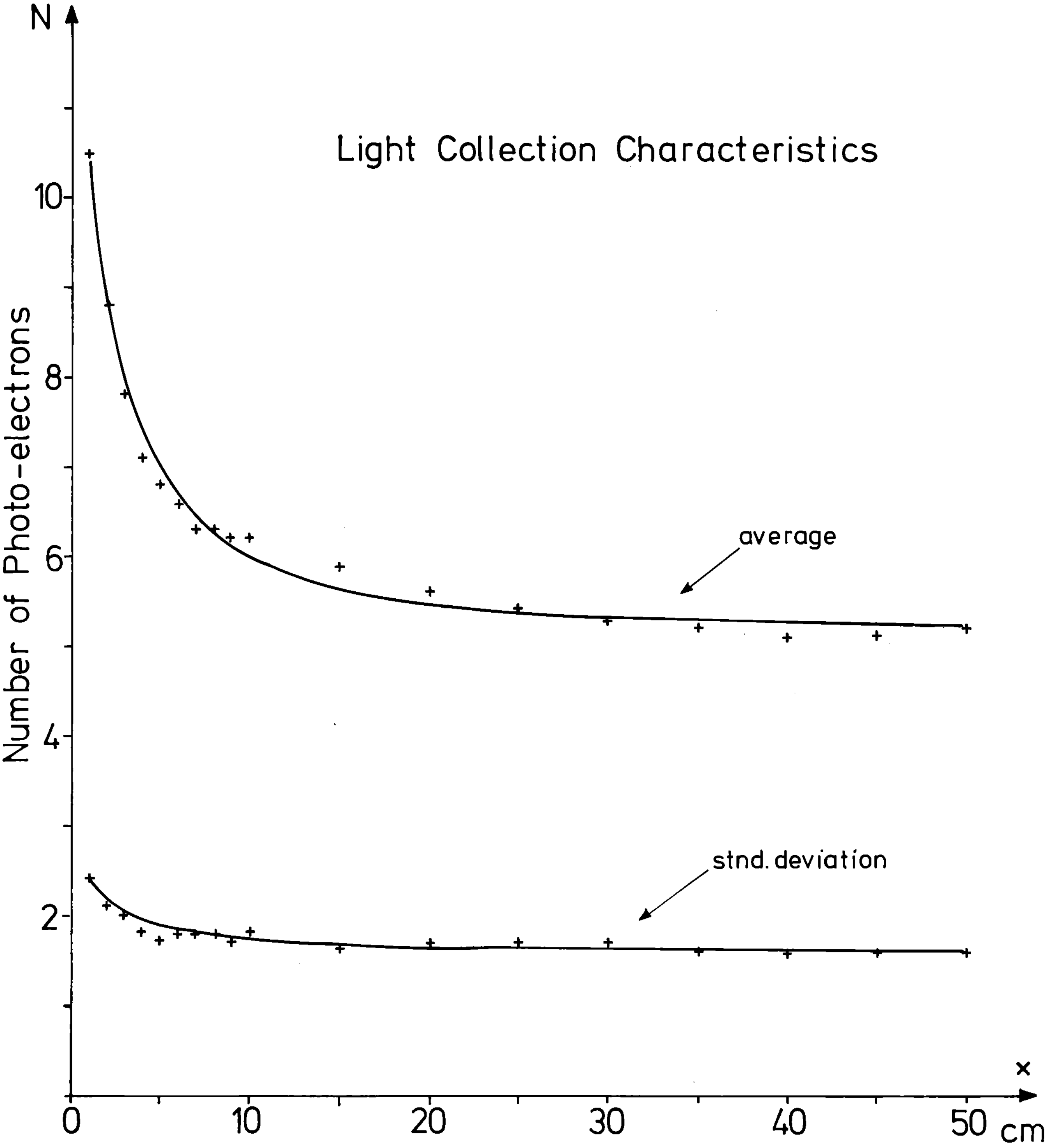

Fig.30: Spatial variation in the number of photo-electrons and standard deviation versus the distance from the closest photomultiplier tube for a source of 500 scintillation photons. The number of electrons represents the square root of the product of the number of photo-electrons produced in each tube (10x10x100 cm^3 module). A fit to the data yields for the average number of photo-electrons $y = 12.41 \exp(-0.88\sqrt{x})+5.21$ and for the stnd. deviation $\sigma = 1.86 \exp(-0.84\sqrt{x})+1.60$.

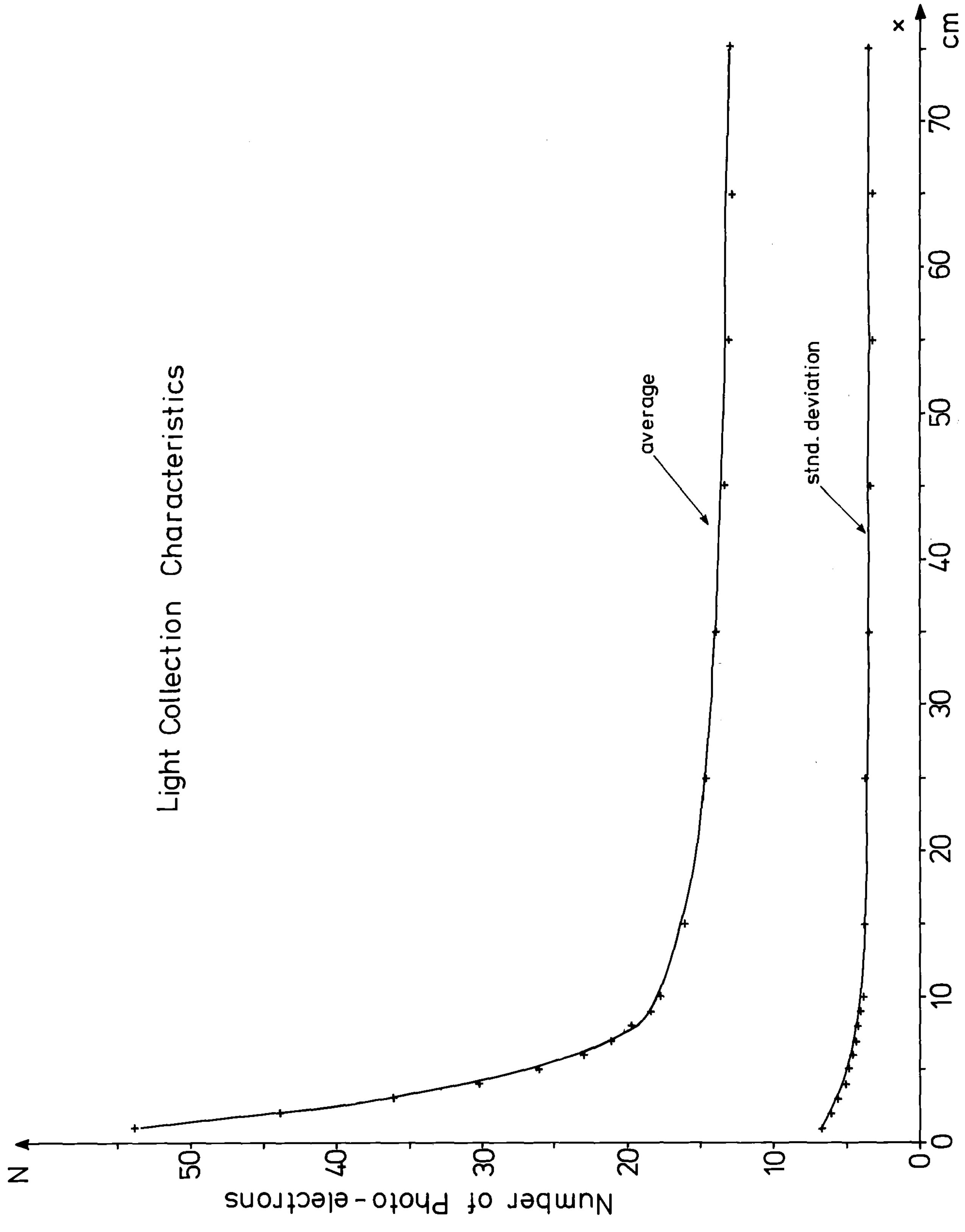

Fig.31: Spatial variation in the number of photo-electrons and standard deviation versus the distance from the closest photomultiplier tube for a source of 500 scintillation photons. The number of electrons represents the sum of the number of photo-electrons produced in each tube (20x20x150 cm^3 module). A fit to the data yields for the average number of photo-electrons

$$y=\begin{cases}53.00\exp(-0.27x)+13.00, & x\leq 8\\ 29.62\exp(-0.55x)+12.8\ , & x>8\end{cases}$$

and for the stnd. deviation $\sigma=3.94\exp(-0.21x)+3.5$.

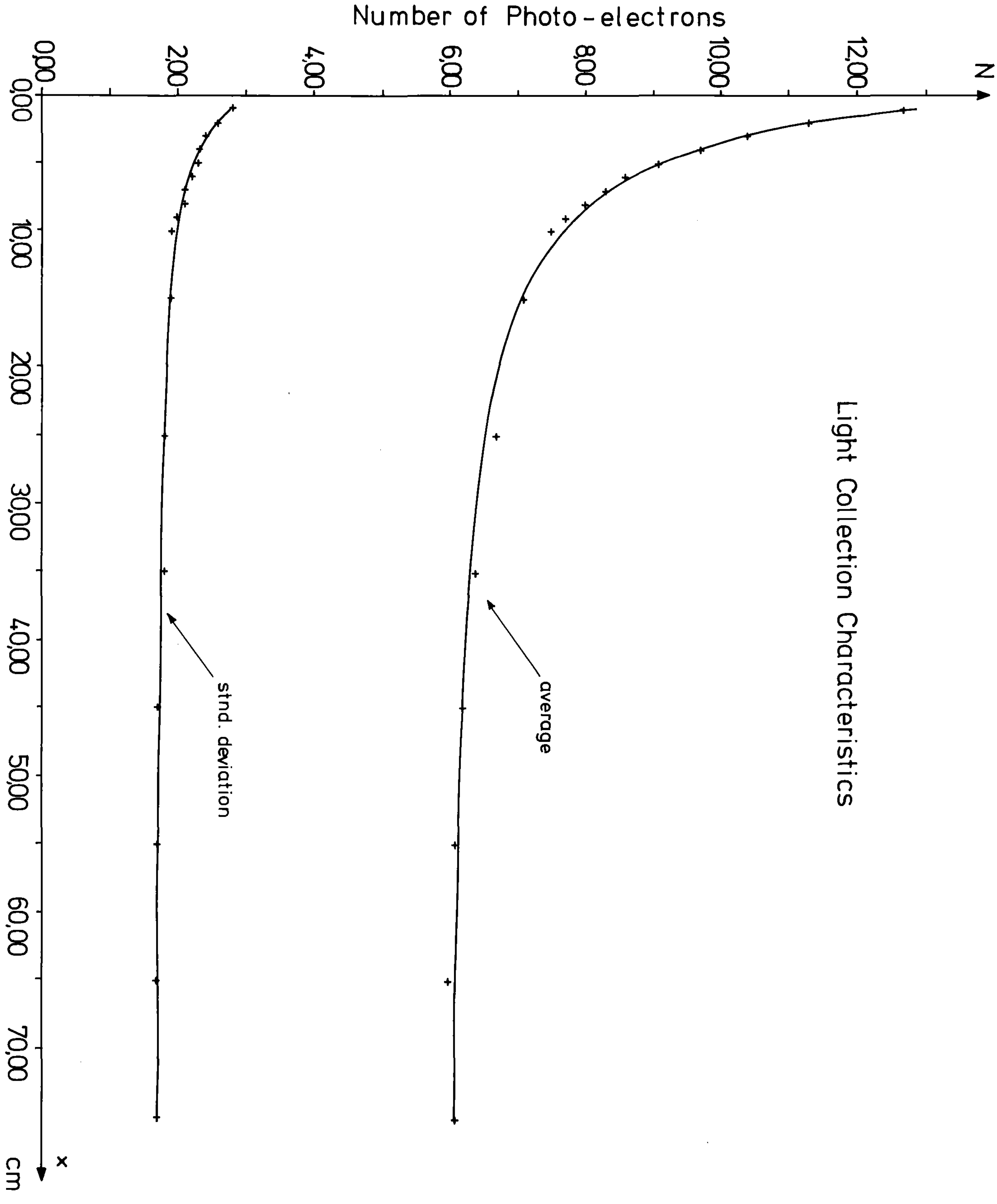

Fig.32: Spatial variation in the number of photo-electrons and standard deviation versus the distance from the closest photomultiplier tube for a source of 500 scintillation photons. The number of electrons represents the square root of the product of the number of photo-electrons produced in each tube (20x20x150 cm^3). A fit to the data yields for the average number of photo-electrons $y=13.21\exp(-0.66\sqrt{x})+6.04$ and for the stnd. deviation $\sigma=2.00\exp(-0.60\sqrt{x})+1.70$.

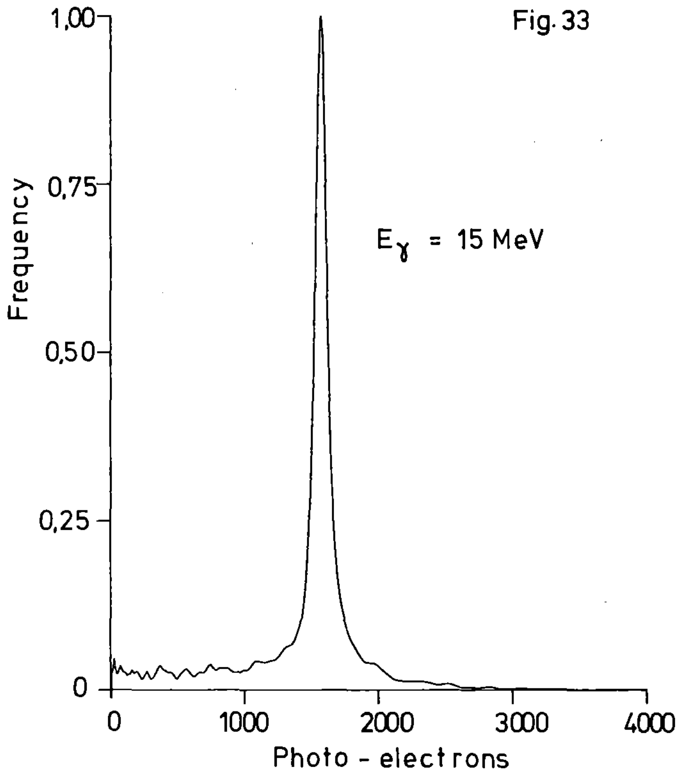

Fig.33: Pulse height distribution for 15 MeV gamma rays in the 10x10x100 cm^3 modular detector system using the photo-electron production data given in fig.30.

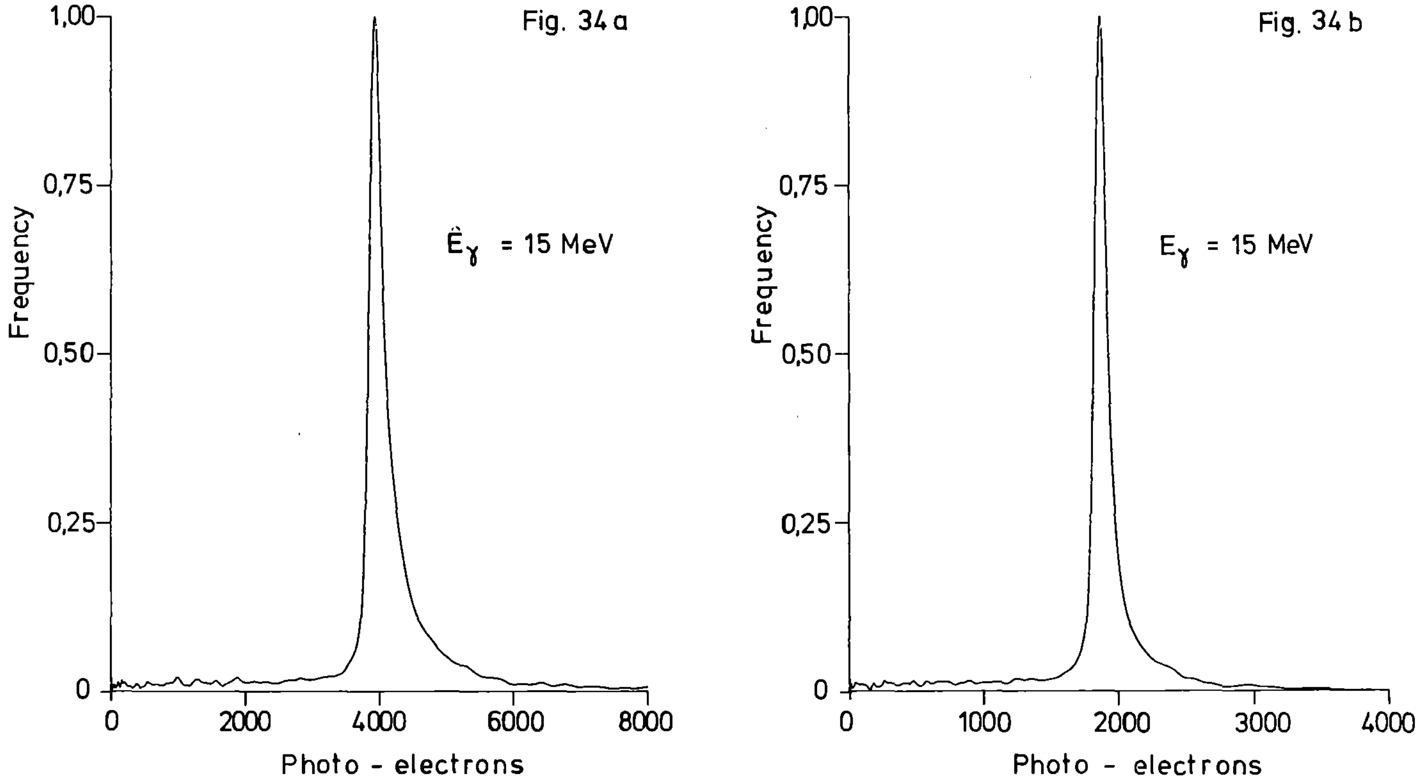

Fig.34: Pulse height distribution for 15 MeV photons in the 20x20x150 cm^3 modular detector system
a) sum dependence for photo-electron statistics,
b) product-square dependence on photo-statistics.

The remaining pulse height distributions for the energies and particles considered previously are given in figs. 35-37 (sum dependence on photo-statistics) and 38-40 (product square root dependence on photo-statistics).

The efficiency and resolution of both detector systems are summarized in Table 9. Even though these detector systems are quite large a substantial number of gamma rays are produced near the edge and can escape before producing a signal. All electron energies will have 100% efficiency. Using the square root of the product of the number of electrons each phototube sees can reduce the resolution of the smaller detector by ~2, but does not improve the resolution of the bigger detector drastically.

Liquid-Argon-Detector System

The liquid argon detector system will have fixed dimensions in x and y, namely 2m x 2m, but will have a variable depth as the thickness of the graphite plates or the argon gaps are varied. In all cases, the amount of graphite is fixed at 2.7 tons. It was not discovered until these calculations were finished that the default density of graphite in PEGS is that for diamond, namely 2.26 g/cm^3. The more common density of graphite is 1.7 - 1.8 g/cm^3. Therefore, the effective thickness of the graphite is ~2.26/1.75 times larger than given above. Two thickness of graphite plates have been considered, 0.3 cm and 0.6 cm. For the 0.3 cm case, there are 100 argon gaps and 100 graphite plates; in the 0.6 cm case, 50 argon gaps and 50 graphite plates. The thin plates of conducting material which would have to be plated on the graphite has not been included. As mentioned before, the sampling fluctuations and energy leakage should dominate the resolution of this detector system and therefore, fluctuations in charge collection have not been included.

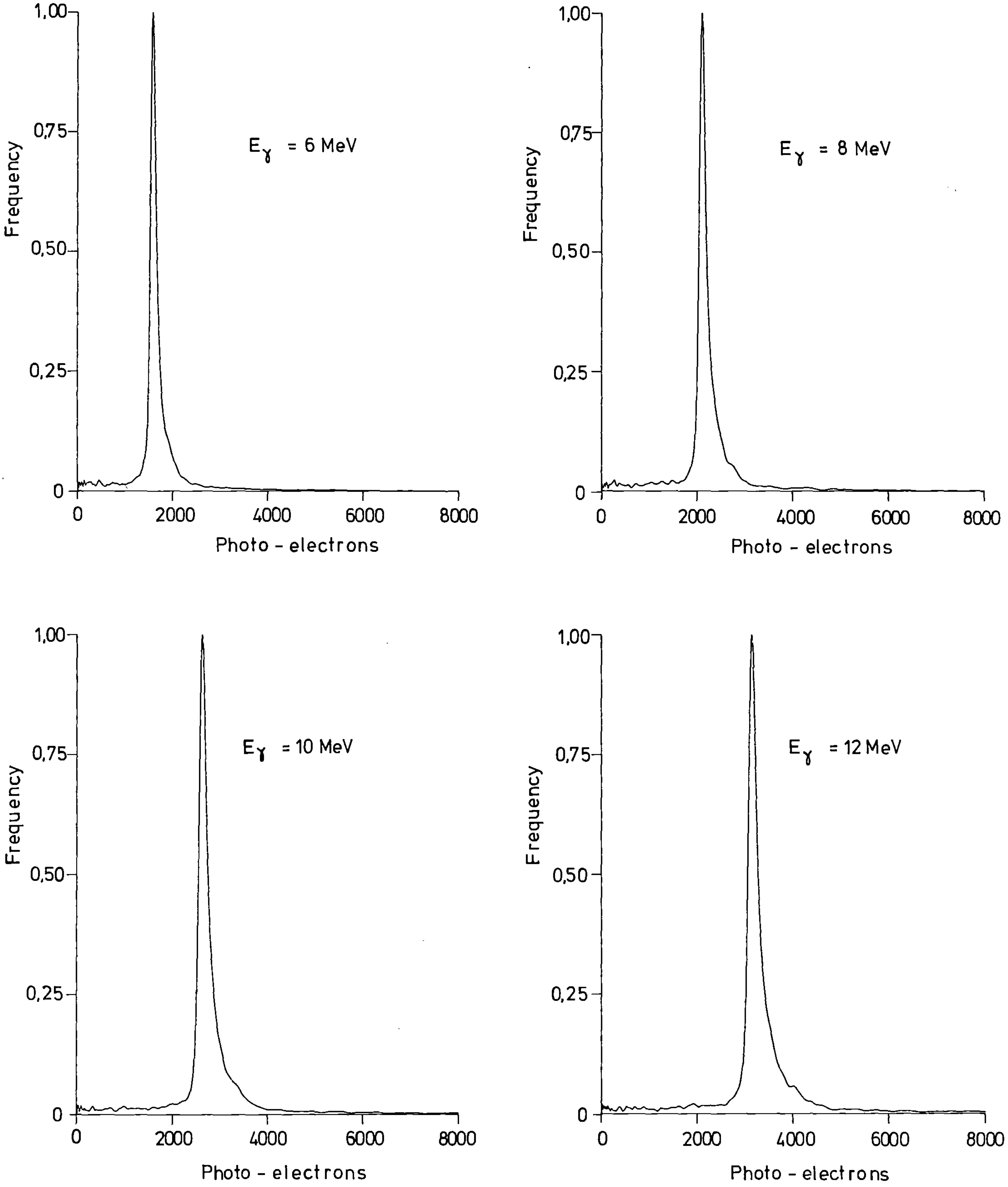

Fig.35: Pulse height distributions for various gamma ray energies (6, 8, 10 and 12 MeV) for the 20x20x150 cm^3 modular detector system. (Sum method for photo-electron statistics.)

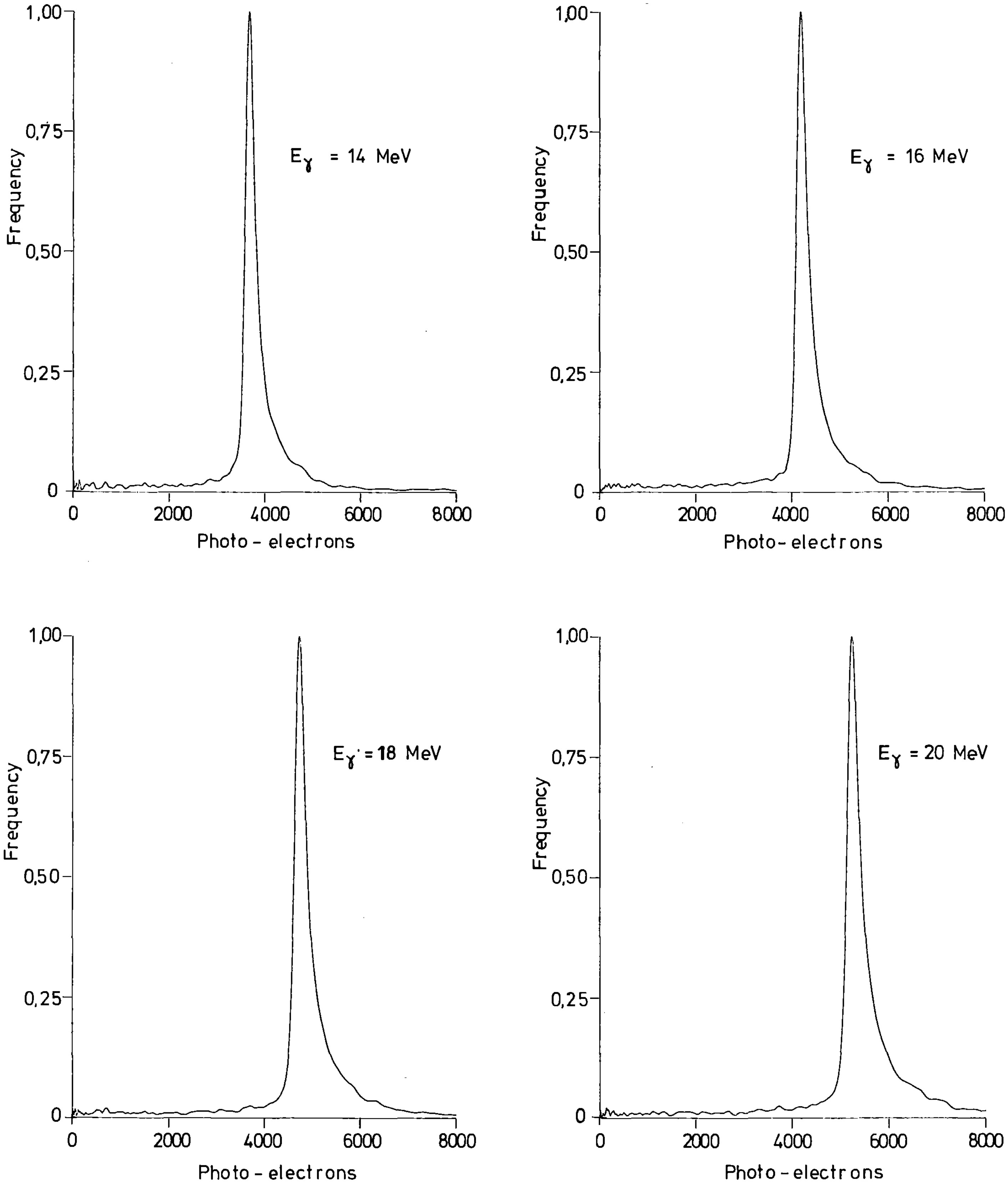

Fig.36: Pulse height distributions for various gamma ray energies (14, 16, 18 and 20 MeV) for the 20x20x150 cm^3 modular detector system. (Sum method for photo-electron statistics.)

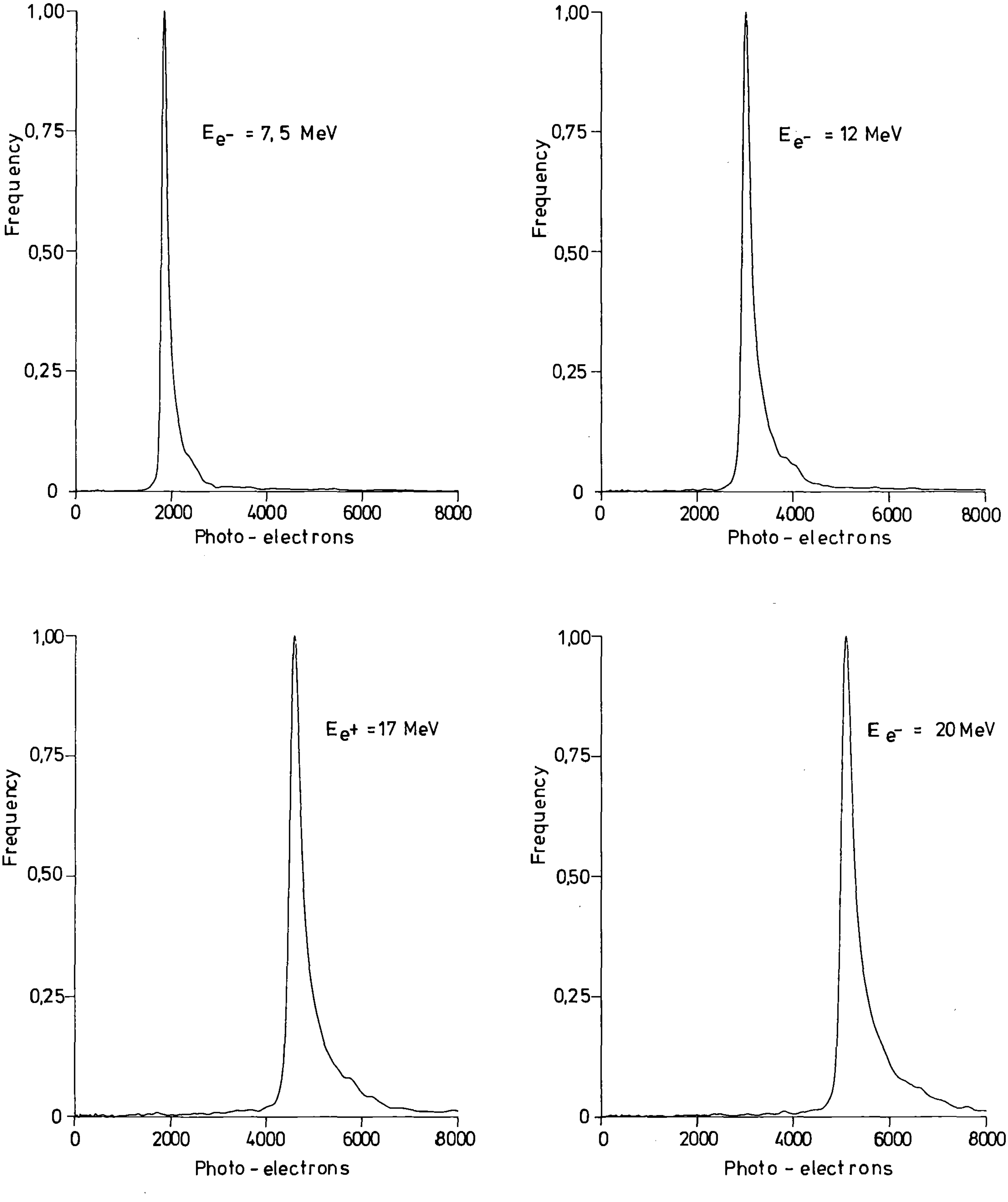

Fig.37: Pulse height distributions for various electron and positron energies for the 20x20x150 cm^3 modular detector system. (Sum method for photo-electron statistics.)

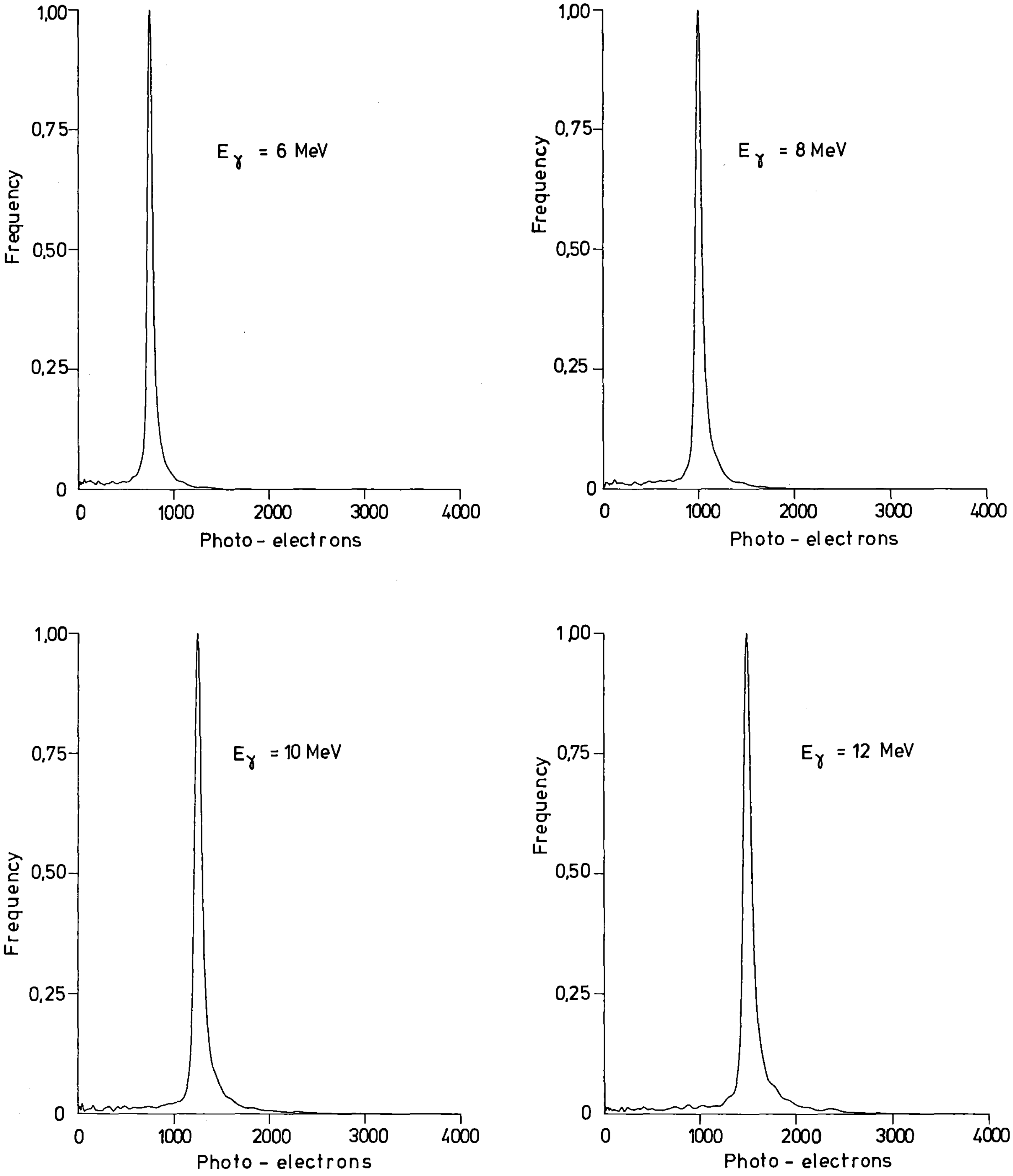

Fig.38: Same as fig.35 except product square root method for photoelectron statistics.

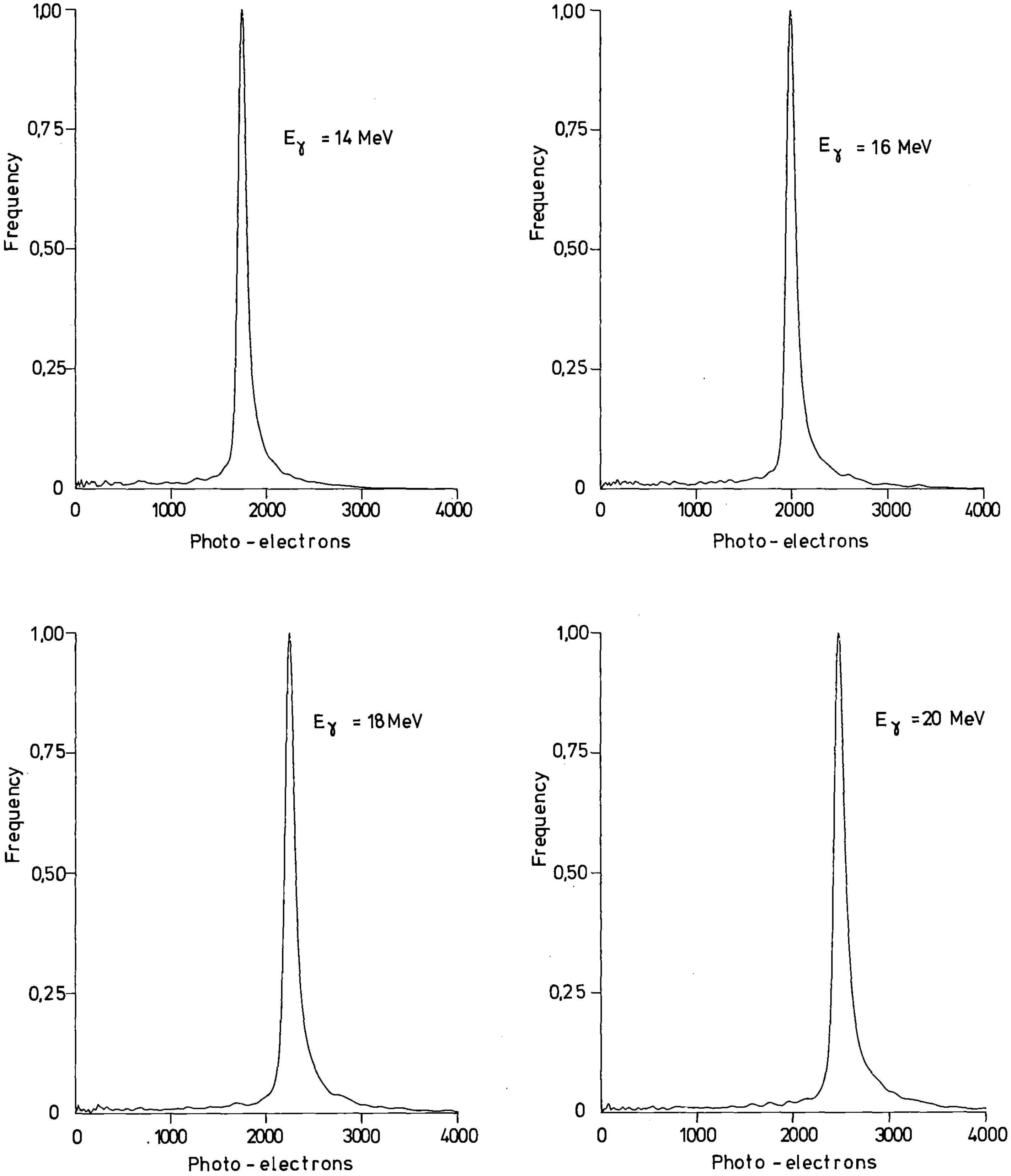

Fig.39: Same as fig.36 except product square root method for photoelectron statistics.

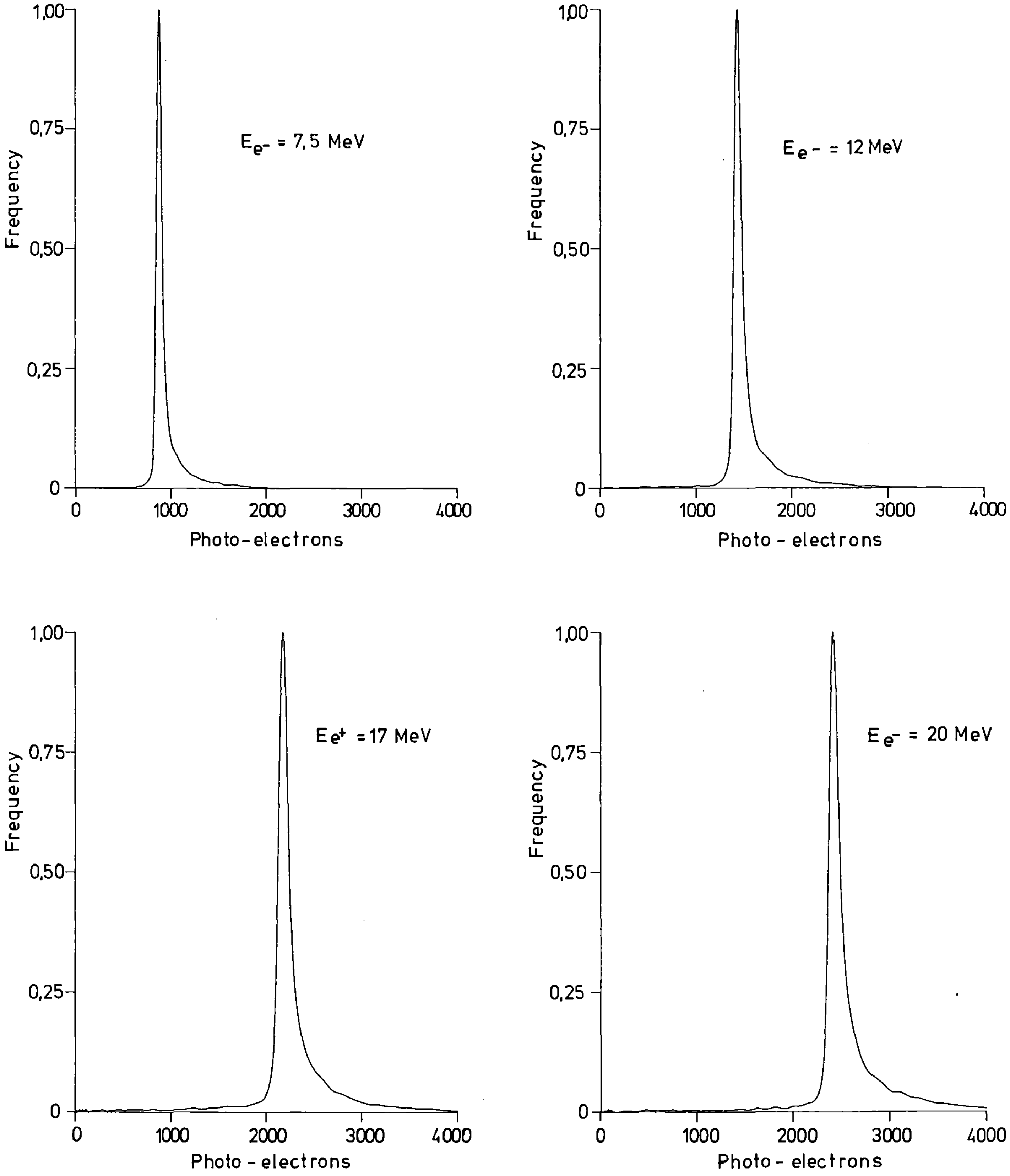

Fig.40: Same as fig.37 except product square root method for photo-electron statistics.

Table 9: Efficiency and Resolution of Both Scintillation Detector Systems

Efficiency (%)

Gamma Ray Energy (MeV)	Detector I[a]	Detector II[b]
6	71.8	83.5
8	68.1	81.1
10	64.4	79.2
12	63.1	77.8
14	61.2	76.8
15	61.5	76.1
16	60.7	75.8
18	59.2	75.2
20	59.6	74.7

a) 10x10x100 cm^3
b) 20x20x150 cm^3

Resolution ($\frac{\Delta E}{E}$ x 100%)

Gamma Ray Energy (MeV)	Detector I[a]		Detector II[b]	
	Method I[c]	Method II[d]	Method I	Method II
6	16.6	9.4	9.3	8.2
8	15.4	7.9	8.1	7.7
10	16.0	7.5	7.7	7.0
12	15.5(16.7,e^-)	7.7(6.8,e^-)	7.2(7.3,e^-)	6.6(6.9,e^-)
14	15.0	7.0	7.2	6.4
15	15.4	7.2	6.3	6.1
15x[e]	6.1	6.2	5.0	4.9
16	15.7	7.1	6.5	5.9
18	14.6	6.8	6.1	5.4
20	16.4(16.3,e^-)	6.5(5.9,e^-)	6.1(6.3,e^-)	5.4(5.6,e^-)

c) Sum dependence on photostatistics; d) product square dependence on photostatistics; e) no photostatistics.

The expected pulse height distributions for 15 MeV gamma rays distributed isotropically and uniformally within the graphite is given in figs.41 and 42 for 0.3 and 0.6 cm graphite plates and for various argon gaps. The resolution is unacceptably large for the 0.6 cm case and is largely unacceptable for the 0.3 cm (1.2 cm argon gap) case. The effect on the resolution and detection efficiency of restricting the interactions to within 35 cm of an edge of the detector is shown in fig.41c. The efficiency is drastically increased with a minimal decrease in the resolution.

The probability that the 15 MeV gammas will escape the system without producing a signal is given in Table 10. Note how drastically this percentage is reduced if the source of the gammas is restricted. The detection efficiency is 100% minus the number presented in this table.

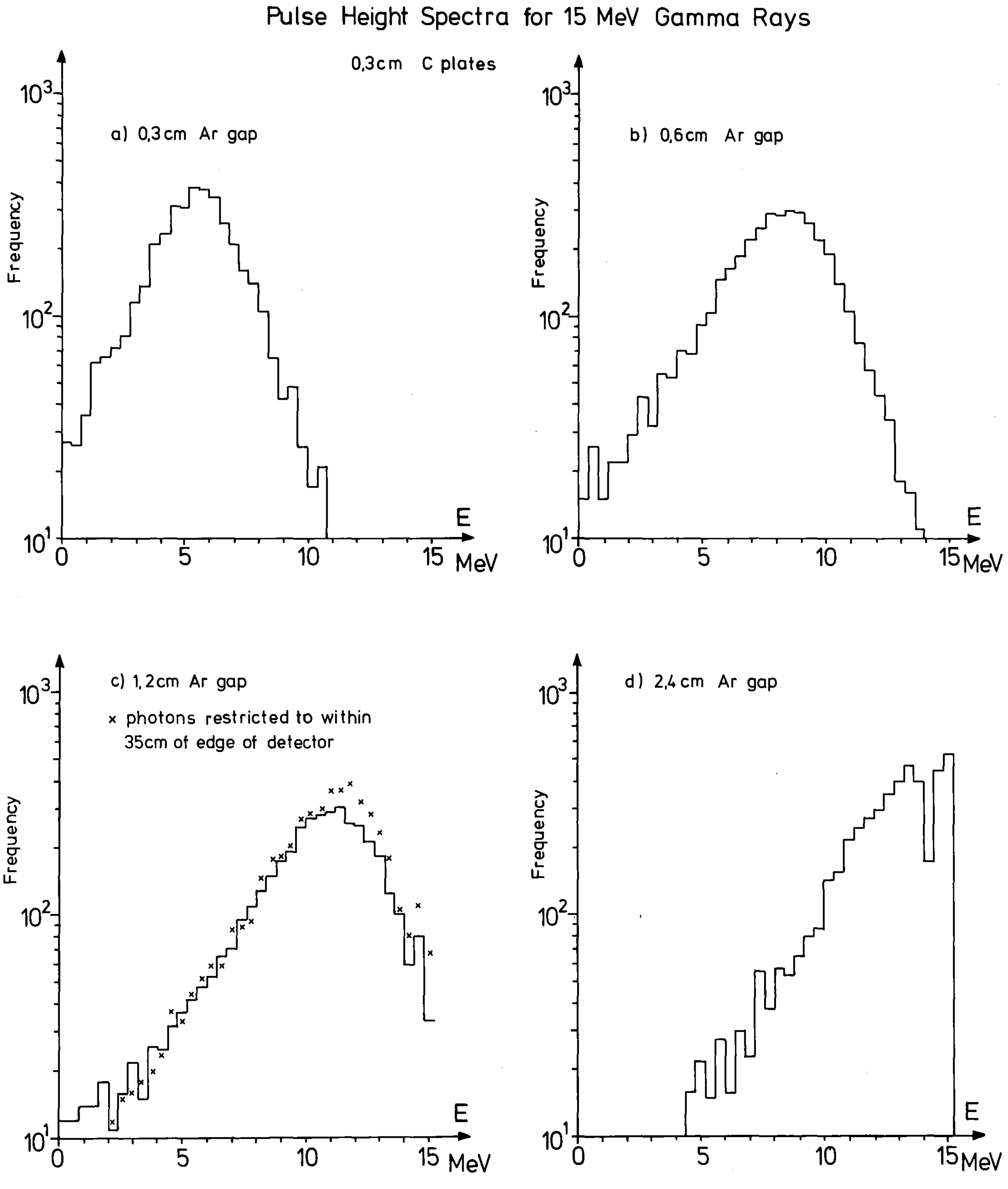

Fig. 41: Pulse height distributions for 15 MeV gamma rays in the liquid argon ionization chamber for 0.3 cm thick graphite plates and for various thickness of the argon gaps.

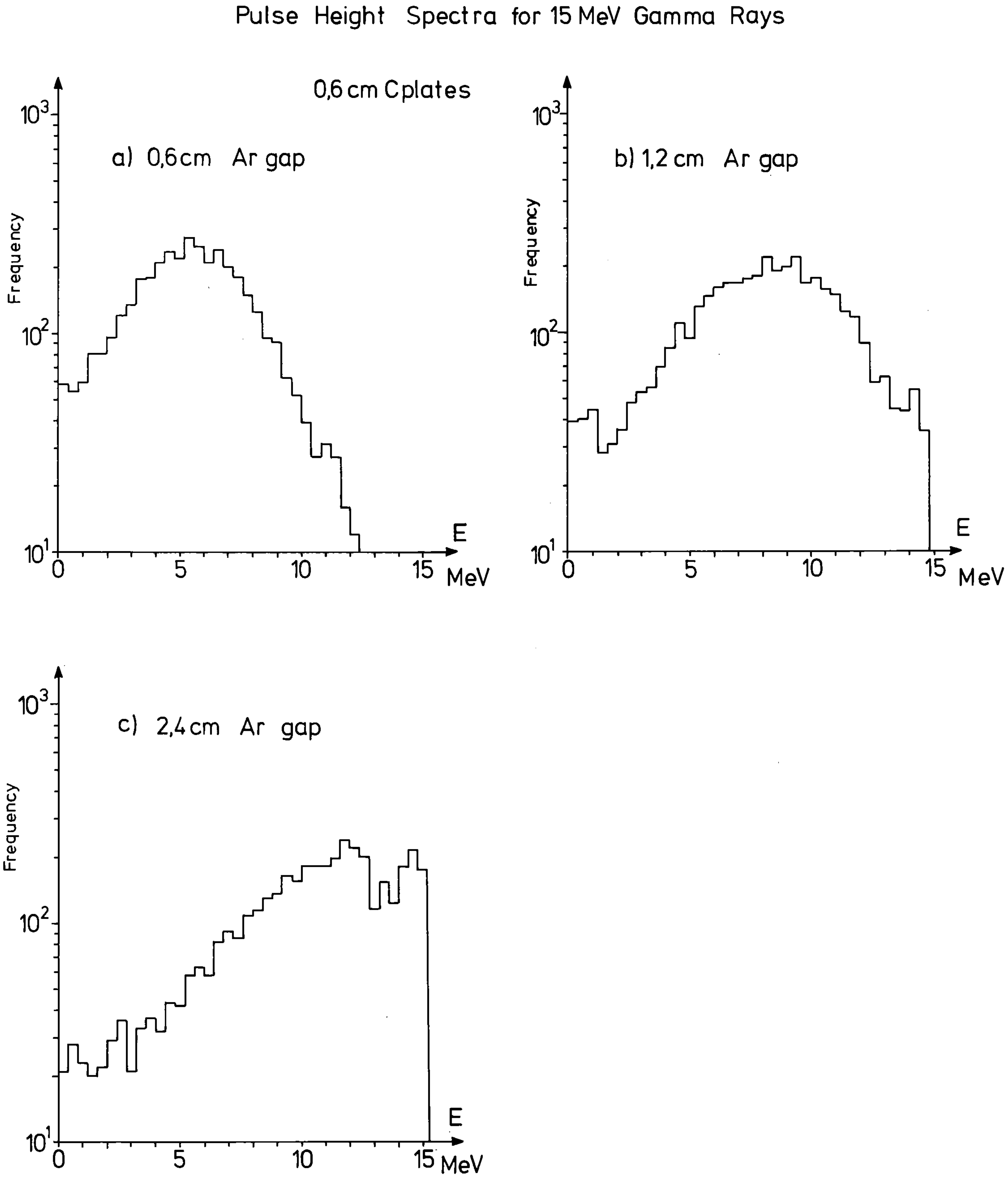

Fig.42: Pulse height distributions for 15 MeV gamma rays in the liquid argon ionization chamber for 0.6 cm thick graphite plates and for various thickness of the argon gaps.

Table 10: Percentage of 15 MeV Gamma Rays Escaping from Detector

0.3 cm graphite[++] plates (200 plates)

Ar gap (cm)	Escapes	Volume of Det (m^3)
0.3	22.6%	2x2x1.2
0.6	20.5%	2x2x1.8
1.2	17.9% (4.7%)[+]	2x2x3.0
2.4	3.8%	2x2x5.4

0.6 cm graphite plates (100 plates)

Ar gap (cm)	Escapes	Volume of Det (m^3)
0.6	24.2%	2x2x1.2
1.2	21.3%	2x2x1.8
2.4	17.9%	2x2x3.0

[+] interaction not within 35 cm of an edge

[++] $\rho = 2.26$ g /cm^3

Presented in figs.43 and 44 are the expected pulse height distributions for 5 and 10 MeV gamma rays, and 17 MeV e^+ and 20 MeV e^- for the 0.3 cm (1.2 cm argon gap) graphite case. Table 11 presents similar data to that given in Table 10 for the additional particles and energies considered. In addition, the self-vetoing probability is given which represents the probability that part of the energy from the source particle will escape from the system and fire the veto counter. This data assumes that the anti counters are located close to the detector and that the escaping particles do not have to penetrate any of the cryogenic container.

Due to the reasonably poor resolutions obtained with this detector and to the problems associated in general with cryogenic systems liquid argon ionization chambers with thin graphite plates would be a poorer choice for a low energy neutrino detector than a segmented mineral oil detector.

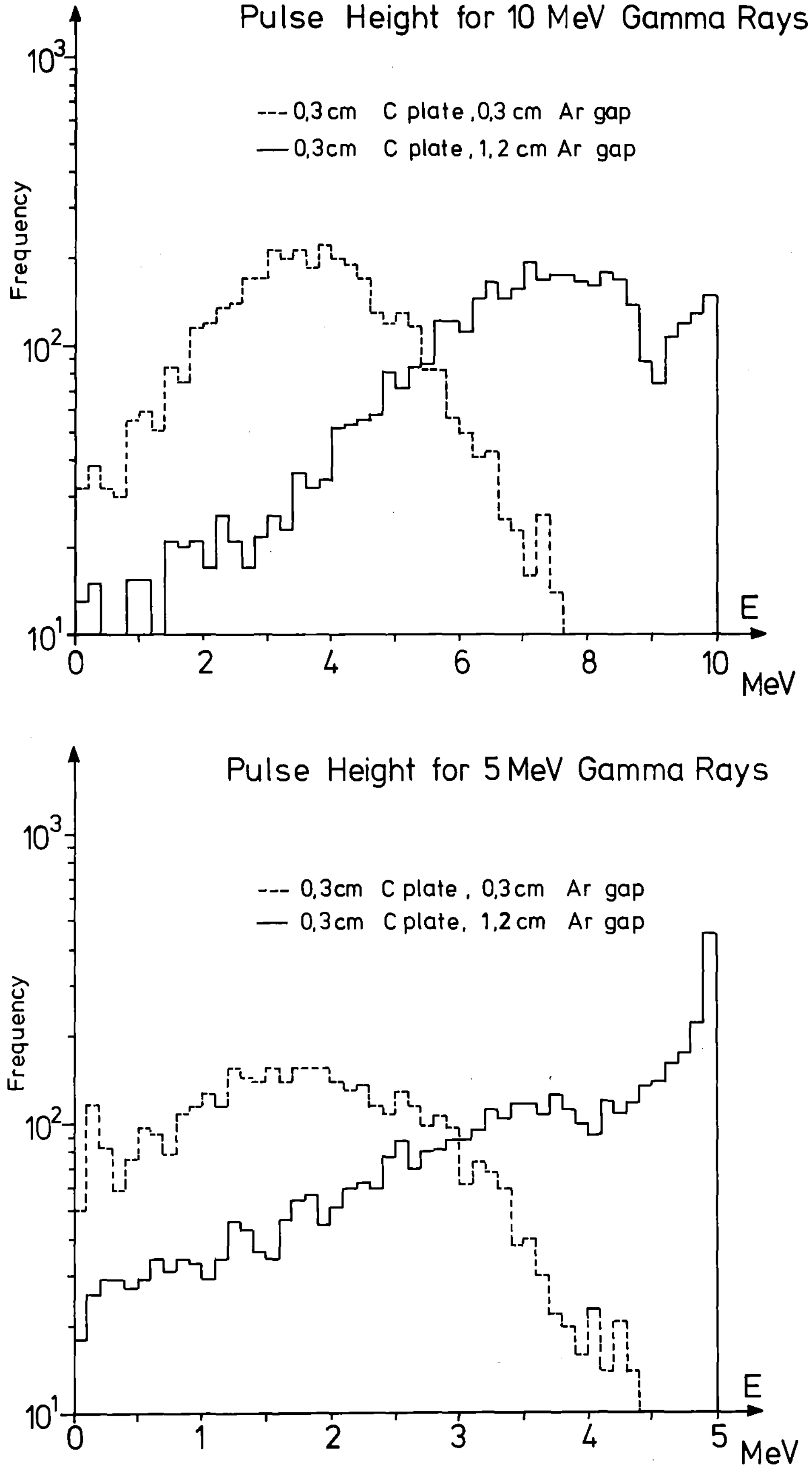

Fig.43: Pulse height distributions for 5 and 10 MeV photons in the liquid argon ionization chamber for 0.3 cm graphite plates and 0.3 and 1.2 cm argon gaps.

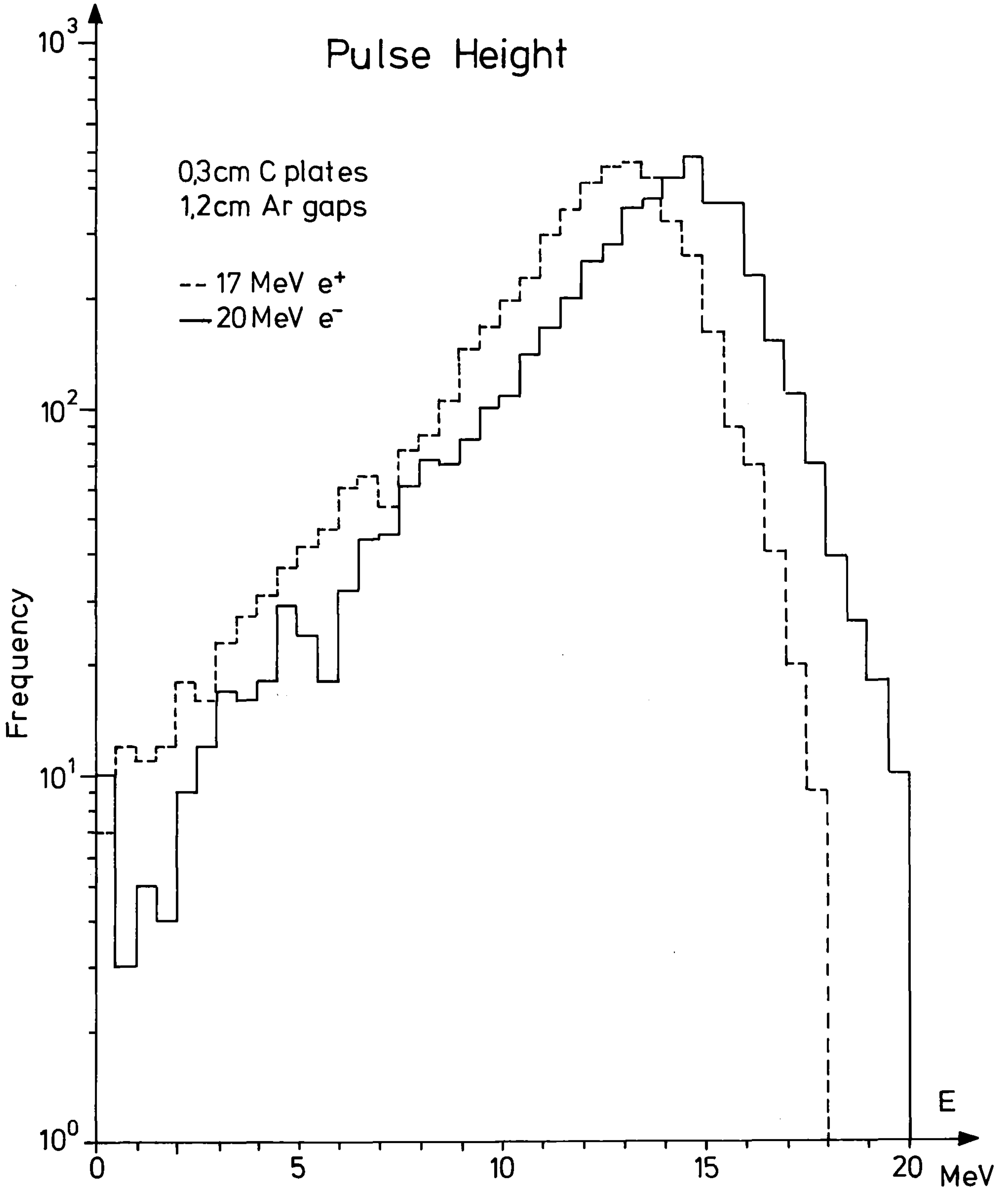

Fig.44: Pulse height distributions for 17.0 MeV e^+ and 20.0 MeV e^- in the liquid argon ionization chamber for 0.3 cm graphite plates and 1.2 cm argon gaps.

Table 11: Percentage of Particles Escaping from the liquid argon detector system and the self vetoing probability of this system

		Percentage of Particles Escaping and Producing no Pulse		Self Vetoing Percentage	
		Ar gap (cm)		Ar gap (cm)	
		0.3	1.2	0.3	1.2
E_γ (MeV)	5	19.6	14.9	0.64	0.40
	10	21.1	17.7	1.4	1.2
	15	22.6	17.9	2.0	1.8
E_{e^-} (MeV)	20	----	0.52	---	3.5
E_{e^+} (MeV)	17	----	0.56	---	3.1

References

1) S.Bilenky and B.Pontecorvo,Phys.Reports 41 225 (1978)

2) S.Weinberg, Phys.Rev.Lett. 19 1264 (1967)

3) H.Faissner et al., Phys.Rev.Lett. 41, 213 (1978)

4) H.Chen and F.Reines, "A Study of Neutrino Electron Elastic Scattering at LAMPF", Status Report UCI-Neutrino No.39, UCLA, Irvine (April, 1980)

5) T.W.Donnelly et al., Phys.Rev. D18, 1607 (1979)

6) S.Weinberg, Phys.Rev.Lett 40, 223 (1978)

7) H.H.Chen "Use of the UCI/LASL Detector to Search for Neutrino Oscillations", Report UCLA Irvine, UCI-Neutrino No.44 (1980)

8) S.E.Willis et al., Phys.Rev.Lett. 44, 522 (1980), see also errata: Phys.Rev.Lett.45, 1370 (1980)

9) T.A.Gabriel et al., "CALOR: A Monte Carlo Program Package for the Design and Analysis of Calorimeter Systems", ORNL-TM-5619 (April, 1977)

10) H.W.Bertini, Phys.Rev. C6, 631 (1972)

11) M.P.Guthrie "EVAP-4: Another Modification of a Code to Calculate Particle Evaporation from Excited Compound Nuclei" ORNL-TM-3119 (1970)

12) R.L.Ford and W.R.Nelson "The EGS Code System: Computer Programs for the Monte Carlo Simulation of Electromagnetic Cascade Showers",SLAC-210 (June, 1978)

13) M.B.Emmett "The MORSE Monte Carlo Radiation Transport
Code System"
ORNL-4972 (February, 1975)

14) W.W.Engle, Jr. "A Users Manual for ANISN, A One Dimensional
Discrete Ordinates Transport Code with Anisotropic Scattering,
K-1693

15) S.A.Dupree et al. "Time Dependent Neutron and Photon Transport
Calculations Using the Method of Discrete Ordinates"
ORNL-4662

16) W.A.Rhoades and F.R.Mynatt "The DOT III Two-Dimensional
Discrete Ordinates Transport-Codes", ORNL-TM-4280 (Sept.1973)

17) R.G.Alsmiller, Jr., J.Barish "Neutron-Photon Multigroup
Cross Section for Neutron Energies $\leq$ 400 MeV"
ORNL-TM-7818

18) H.H.Chen et al., "A Measurement of Stopped π^+ Decays in a
Copper Beam Dump with Incident Protons of 720 MeV (A Calibration of the LAMPF Neutrino Source Intensity)"
UCI-Neutrino No.17, Internal Report, Feb.1976

19) B.Zeitnitz "Neutrino Physics at the Spallation Neutron Source"
KfK 3155, March 1981

20) T.W.Armstrong, K.C.Chandler, J.Barish "Journal Geophys.Res.,
Vol.78, 2715 (1973)"

21) A.W.Wolfendale "Cosmic Rays at Ground Level",Inst.of Physics
(1973)

22) "Electromagnetic Interactions of Hadrons", Vol.II
edited by A.Donnachie, G.Shaw, Plenum Press, NY, pages 299-305